The Pennsylvania State University

The Graduate School

College of Earth and Mineral Sciences

TIME-LAPSE SEISMIC ANALYSIS OF THE TAHOE FIELD, VIOSCA KNOLL BLOCK 783, OFFSHORE GULF OF MEXICO

A Thesis in

Geosciences

by

Joseph L. Razzano III

Submitted in Partial Fulfillment
of the Requirements
for the Degree of

Master of Science

May 2006

I grant The Pennsylvania State University the nonexclusive right to use this work for the University's own purposes and to make single copies of the work available to the public on a not-for-profit basis if copies are not otherwise available.

Joseph L. Razzano III

The thesis of Joseph L. Razzano III was reviewed and approved* by the following:

Peter B. Flemings
Professor of Geosciences
Thesis Advisor

Charles J. Ammon
Associate Professor of Geosciences

Sridhar Anandakrishnan
Associate Professor of Geosciences

Turgay Ertekin
Professor and George E. Timble Chair in Earth and Mineral Sciences
Chair of Petroleum and Natural Gas Engineering

Katherine H. Freeman
Professor of Geosciences
Associate Head for Graduate Programs and Research

*Signatures are on file in the Graduate School

ABSTRACT

We add to current knowledge about the M4.1 channel-levee through acoustic modeling of the pre-production M4.1 reservoir using seismic, well log, core, and pressure data. We use our acoustic characterization to initialize fluid substitution models that predict changes in acoustic rock and fluid properties for several production-related scenarios. We then predict the acoustic response of each scenario using synthetic seismic modeling and compare results with pre-production synthetic data. We attribute observed seismic differences, following seven years of production, to changes in the acoustic properties of the M4.1 reservoir. We observe both seismic strengthening and weakening throughout the M4.1. Seismic strengthening in the reservoir is attributed to gas exsolution in the oil phase, while seismic weakening is attributed to an increase in oil saturation in a gas-oil system.

We interpret the observed increase in seismic amplitude, down-dip of well 783-5BP, to suggest the presence of an oil rim in a region that was initially characterized as containing only gas. Based on seismic brightening observed to the south in the East Levee, we interpret the presence of oil down to a depth of 10,500ft and place the pre-production oil-water contact (OWC) at this depth. This contact is located 90ft further down structure than the originally interpreted OWC.

Time-lapse analysis reveals an increase in seismic amplitude in the West Levee, above the gas-oil contact (GOC), which we attribute to gas exsolution in the oil phase. Within this region, the M4.1 sand contains both gas and oil in an area we term the "fringe" zone. We show, through Gassmann fluid substitution and synthetic seismogram

modeling, that gas exsolution in the oil phase of this fringe zone is consistent with the observed seismic strengthening.

While seismic differences are observable throughout the M4.1 reservoir, seismic differences are significantly stronger in two regions: R1 and R4. The M4.1 sand in region R1 is very clean and has a large impedance contrast with respect to the overlying shale. These two factors cause drainage in the region to significantly alter the acoustic properties of the reservoir, which results in the strong seismic differences observed in the time-lapse analysis. Region R4, located in the West Levee, also exhibits a strong difference in seismic response after seven years of production. The M4.1 sand is thickest this region. The increased thickness causes greater constructive interference between the wavelets recording the top and bottom of the sand. An increase in constructive interference results in better imaging of the sand and captures the changes in acoustic properties resulting from production.

The observed changes in fluid behavior seen in the post-production M4.1 have helped to better explain the initial fluid conditions in the reservoir. Through our analysis, we have identified oil reserves in a region that was initially believed to contain only gas. Also, based on the time-lapse analysis, we relocated a pre-production oil-water contact, which results in identification of additional hydrocarbon reserves in the region.

This methodology employed by this study can be applied to any field that has been imaged by two or more seismic datasets separated by calendar time. Time-lapse analysis can increase the economic life of hydrocarbon reservoirs, as well as increase our understanding of dynamic changes in rock and fluid properties that occur during production.

TABLE OF CONTENTS

List of Figures

LIST OF TABLES

ACKNOWLEDGEMENTS

It is my sincere belief that my work, as well as the work of the entire Petroleum Geosystems Initiative, would not be possible without the data/technical support provided by Heather Nelson and Tom Canich. On numerous occasions they dropped what they were doing in order to help with our work and for that I am truly grateful.

To my friends in state college, all I can say is…"Simply Stunning". To Rocco, Unkel Ted, CJ, and M-Dawg, I leave you with this…there will be more Stage 5 Alerts in your lives and I ask you to remember and respect Rule #76…"No Excuses, Play Like A Champion!" I will never forget the El-Four-O-Deuce, the sunsets, the celebrations, and most of all…each of you. "He said it's the life for all his life, but then one day he said… "No, I Gotta' Go"

Finally, I have to say thank you to my best friend in the whole world. Going through this experience with you by my side has been one of the greatest experiences in my life and I cannot imagine having done this without you. You are one of the most genuine and caring people I have ever met and I have learned more from you than you will ever know. I'll love you always, and no mater what changes time may bring, you can always count on me to be there for you...even for a little cuddle.

This thesis is dedicated to both of my grandmothers who were not able to see me achieve this degree. While not here in body, their spirit and influence has certainly been a factor in helping me achieve this degree. Thank You.

Chapter 1

M4.1 Acoustic Characterization

Abstract

Observed amplitude response of the M4.1 reservoir is driven by three main factors: fluid type, impedance contrast at the sand-shale interface, and sand thickness. The M4.1 reservoir of the Tahoe field is a laminated channel-levee system that formed from turbidite flows into an unconfined slope setting (Kendrick, 2000). Two distinct lithofacies are observed within the M4.1 reservoir: the Channel Facies and the Levee Facies. The channel, in conjunction with two large normal faults, compartmentalizes the reservoir. We use amplitude and well-log data to describe the acoustic properties of the reservoir. Analysis of the amplitude response of the M4.1 sand provides a static pre-production characterization that will serve as the basis for modeling post-production changes in amplitude response seen in additional seismic datasets.

1.1 Introduction

The Tahoe field was one of the first channel-levee systems to be produced in the deep-water Gulf of Mexico (GOM) (Kendrick, 2000). Tahoe is located in the GOM 140 miles southeast of New Orleans and was discovered in 1984 (Fig. 1). The main reservoir in the field is termed the M4.1. Development began in January 1994 and as of March 2004; the M4.1 had produced 7.2 million stock tank barrels of oil (MMSTB) and 165 billion cubic feet of gas (BCF).

The M4.1 is the main reservoir and it has been interpreted as a channel-levee system formed from turbidite flows into an unconfined slope setting (Kendrick, 2000). Rapid pulses of sediment originated from the northwest and flowed for many miles along ribbon-like channels to the southeast during the Late Miocene (White et al., 1992). The sediments have been interpreted as levee and interchannel deposits composed of slightly consolidated, very fine grained, and clay rich sandstones (Rollins et al., 1993). Levee deposits within this depositional environment can have laminated sands with high to moderate continuity, which are very productive reservoirs (Shew et al., 1995). At Tahoe, sand laminations range from less than a millimeter to several centimeters. (Akkurt et al., 1997). Faults, the anticlinal dome structure, and poor connectivity across the channel, has led to the compartmentalization of the reservoir (Enunwa et al, 2005; Kendrick, 2000).

We present a detailed petrophysical analysis of the M4.1 sand in order to build an acoustic model of the sand. Analysis of the amplitude response of the M4.1 sand, using seismic and well log data, will provide a static pre-production characterization to allow
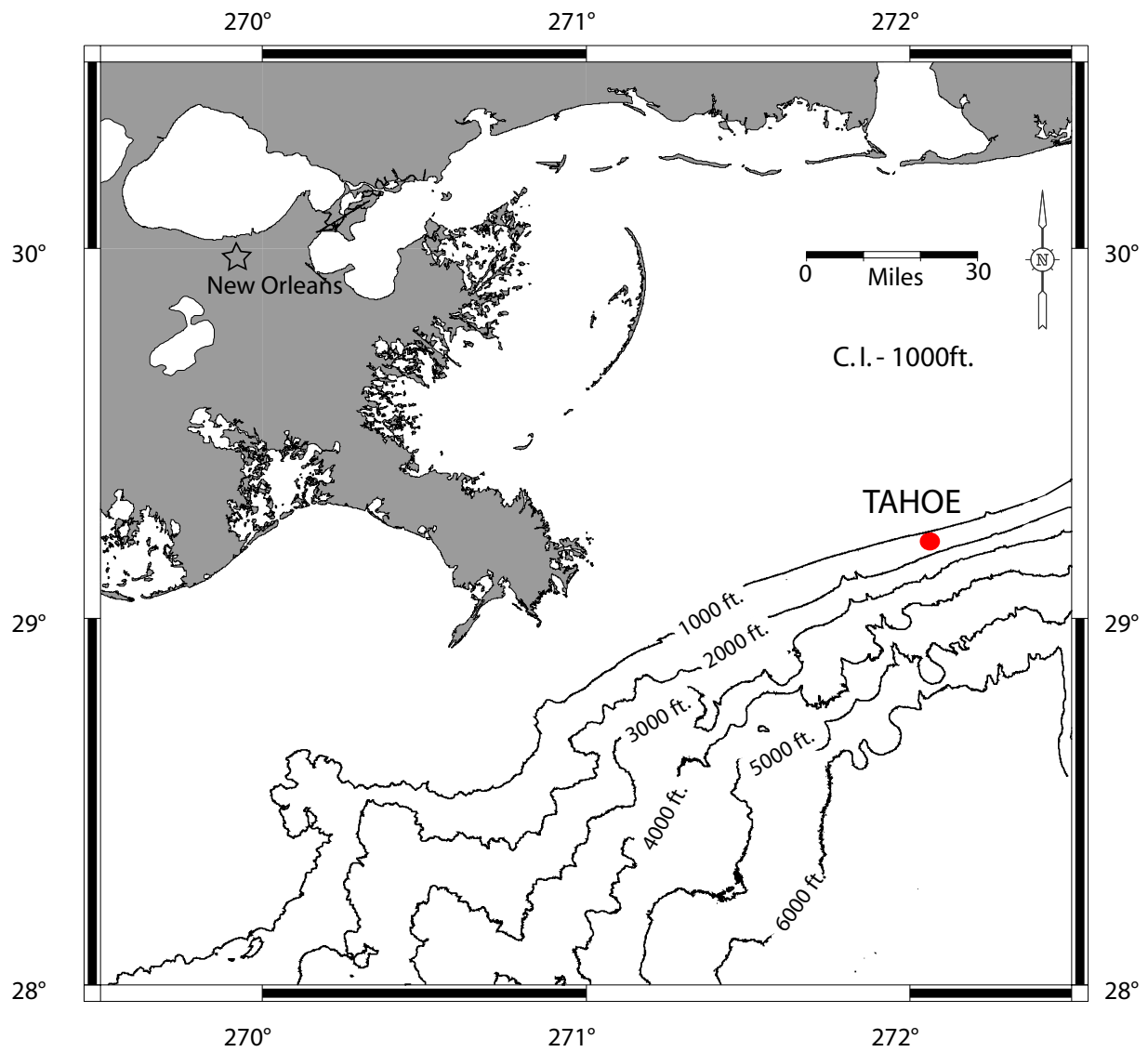
Figure 1: Location map of Tahoe Field. Tahoe (red dot) is located 140 miles south-east of New Orleans and lies in water depths ranging from 350 to 500 meters.

interpretation of seismic data and to serve as the basis for modeling post-production changes in amplitude response seen in additional seismic datasets.

1.2 Geologic Overview

The M4.1 reservoir is located mainly in Block VK 783 at approximately 10,000 ft below sea-level (Fig. 1). The M4.1 sand is bounded by Fault A to the north and Fault B to the southwest (Fig. 2). Two distinct lithofacies are observed within the M4.1 reservoir: the Channel Facies and the Levee Facies. The Channel Facies is sand-rich, has a blocky gamma ray log signature (Fig. 3A), and was penetrated by the 783-2 and 783-1 wells (Fig. 2). The Levee Facies has a sandy base that shales upwards (Figs. 3B & 3C). The gamma ray log is serrated, which suggests that this facies is composed of interbedded sandstone and shale layers. The Levee Facies is present at all locations in the field outside of the channel and generally thins away from the channel. Average net to gross within the Levee Facies ranges from 45% to 59% with bed thicknesses ranging from 0.2 – 3 inches (Enunwa et al., 2005). In seismic cross-section, the levees are thicker than the channel that separates them (Enunwa et al., 2005).

1.3 Seismic Response of the M4.1

We obtained a 3D seismic survey over the Tahoe field acquired in 1993, one year before production began. Shot orientation is northeast-southwest and the data are 60 fold with a bin size of 82x82ft. The survey was conducted with a streamer length of 6,000 m, a CDP line spacing of 50 m, and a shotpoint interval of 50 m. The data were processed using running summation (runsum) techniques.
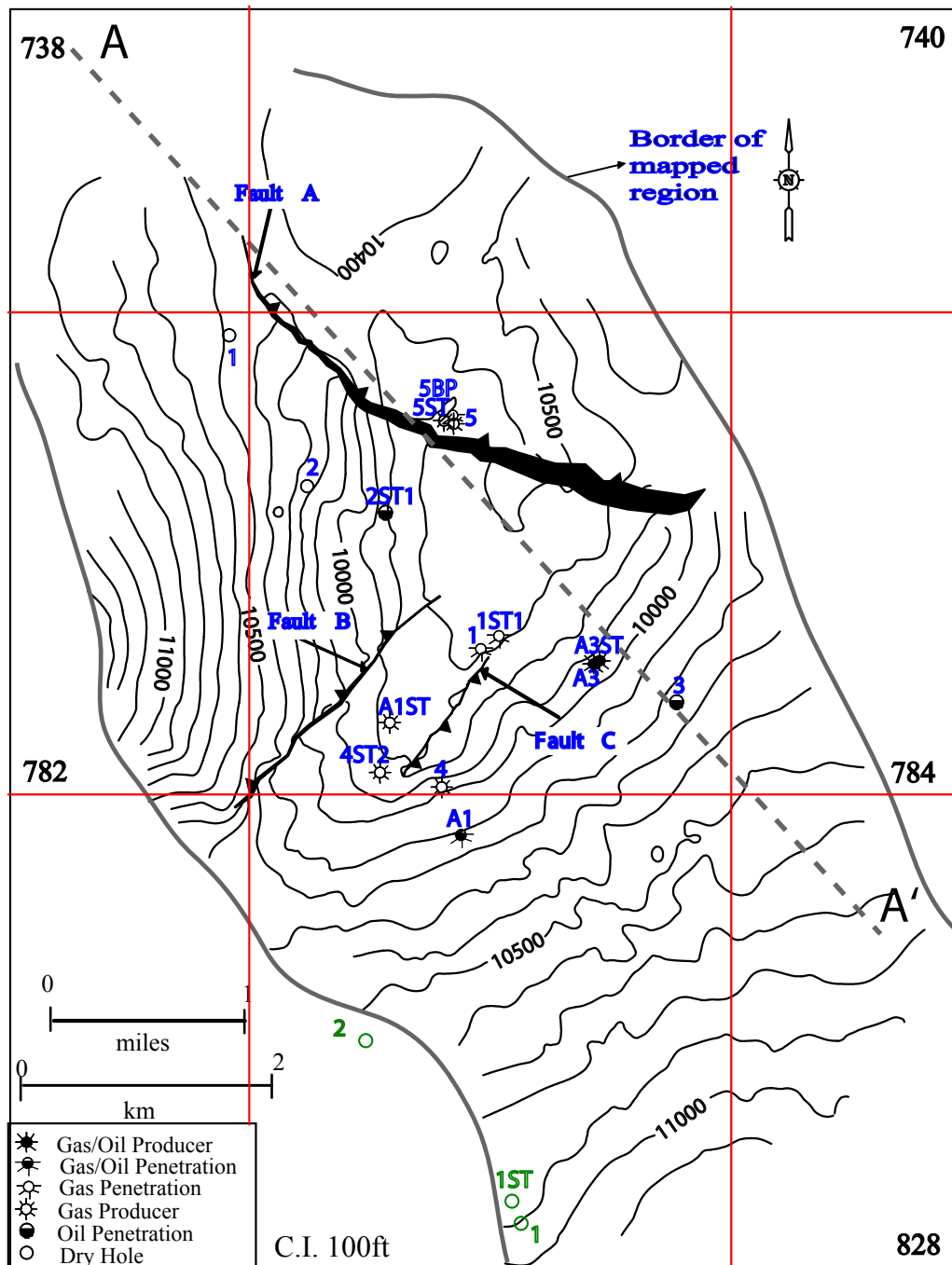
Figure 2: Structure map to the top of the M4.1 sand. The contours are in true vertical sub-sea depth (TVDSS) ft. The M4.1 is an anticlinal dome. It is intersected at the crest of the structure by a regional fault, Fault A, and to the south-southwest by two smaller faults, B and C. This map was made by mapping the M4.1 in time and converting the time map to depth using the depths to the top of the M4.1 at well penetrations. Data from the wells outlined in green were not used to construct this map. The location of seismic cross-section AA' shown in Figure 4 is indicated.
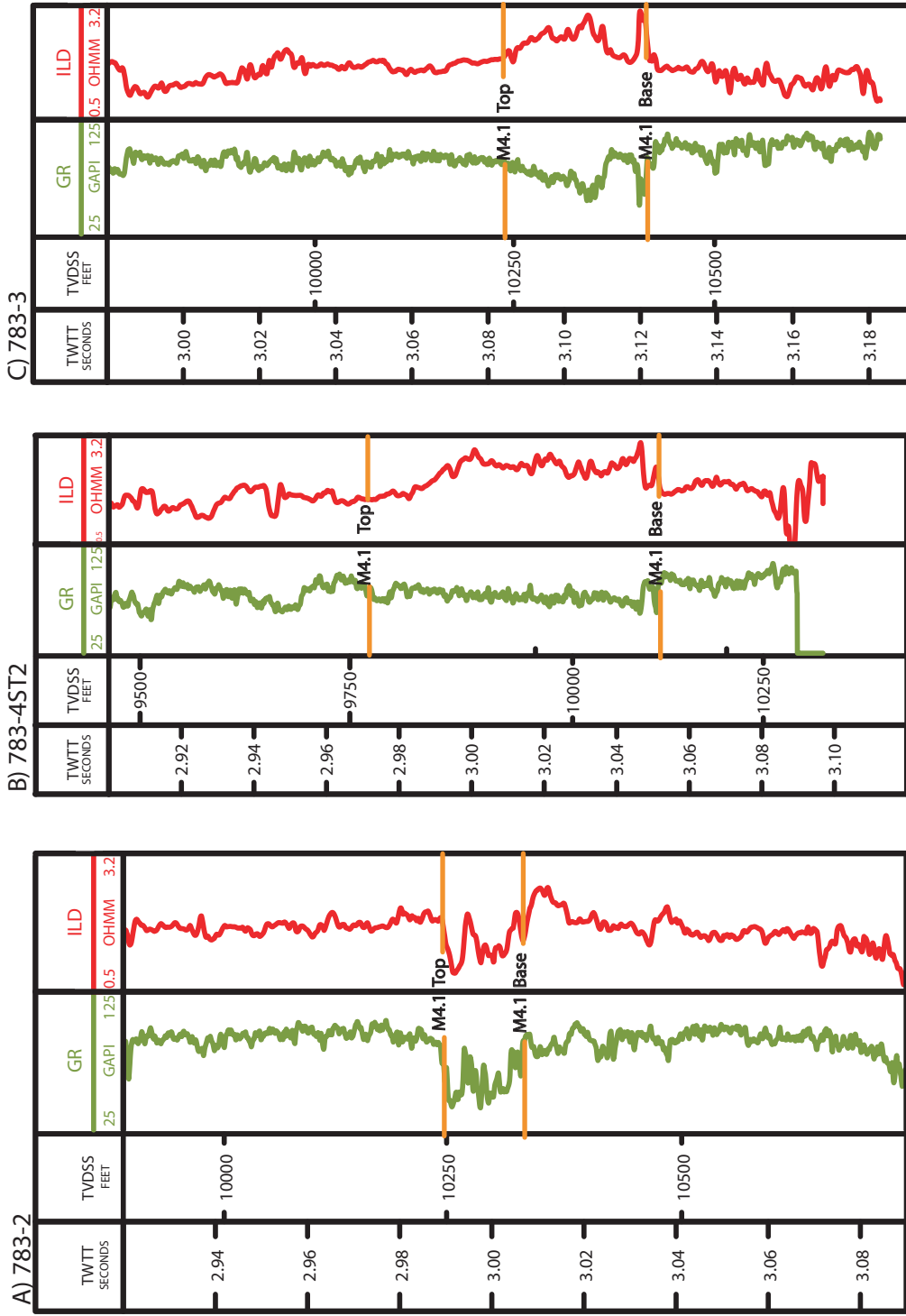
Figure 3: Gamma-ray (GR) and resistivity (ILD) logs for the A) Channel Facies at well 783-2, B) Levee Facies at well 783-4ST2, and C) Levee Facies at well 783-3. Wells are located in Figure 2.

The M4.1 sand is seismically imaged as a trough with the upper and lower zero-crossings marking sand boundaries (Fig. 4). The M4.1 was mapped throughout the seismic dataset to produce an amplitude map (Fig. 5). A region of weak amplitudes trends NW-SE through the center of the reservoir (Fig. 5). Faults A & B, in conjunction with this region of low amplitude, bound amplitudes and compartmentalize the reservoir. Based on the relationship between amplitude and log data, we interpret large negative amplitudes (warm colors) to represent where hydrocarbons are present while small negative amplitudes (cool colors) represent regions of stratigraphic thinning or areas saturated only with water (Fig. 5).

We present a fluid distribution map which divides the M4.1 into three hydrocarbon bearing compartments (Fig. 6). Compartment J, which lies north of Fault A, is interpreted to contain gas based on seismic amplitude response and fluid samples from well penetrations (Fig. 6). Compartment C is located in the western region of block 783 and is interpreted to contain gas based on seismic amplitude response and well penetrations showing gas samples (Fig. 6). We also interpret the presence of an oil rim in Compartment C based on well-log information from well 827-A1, which penetrated the oil-water contact (OWC) (Fig. 6). Compartment A is located in the eastern region of block 783, to the south of Fault A, and is interpreted to contain gas based on amplitude and fluid samples from the 783-1ST1 well (Fig. 6). We also interpret the presence of an oil rim in Compartment A based on amplitude and oil samples from well 783-3 (Fig. 6).

There is a good correlation between seismic two-way travel time (TWTT) thickness and recorded log thickness (Enunwa, 2005). Based on this correlation, a seismic TWTT thickness map was made to better estimate sand thicknesses away from
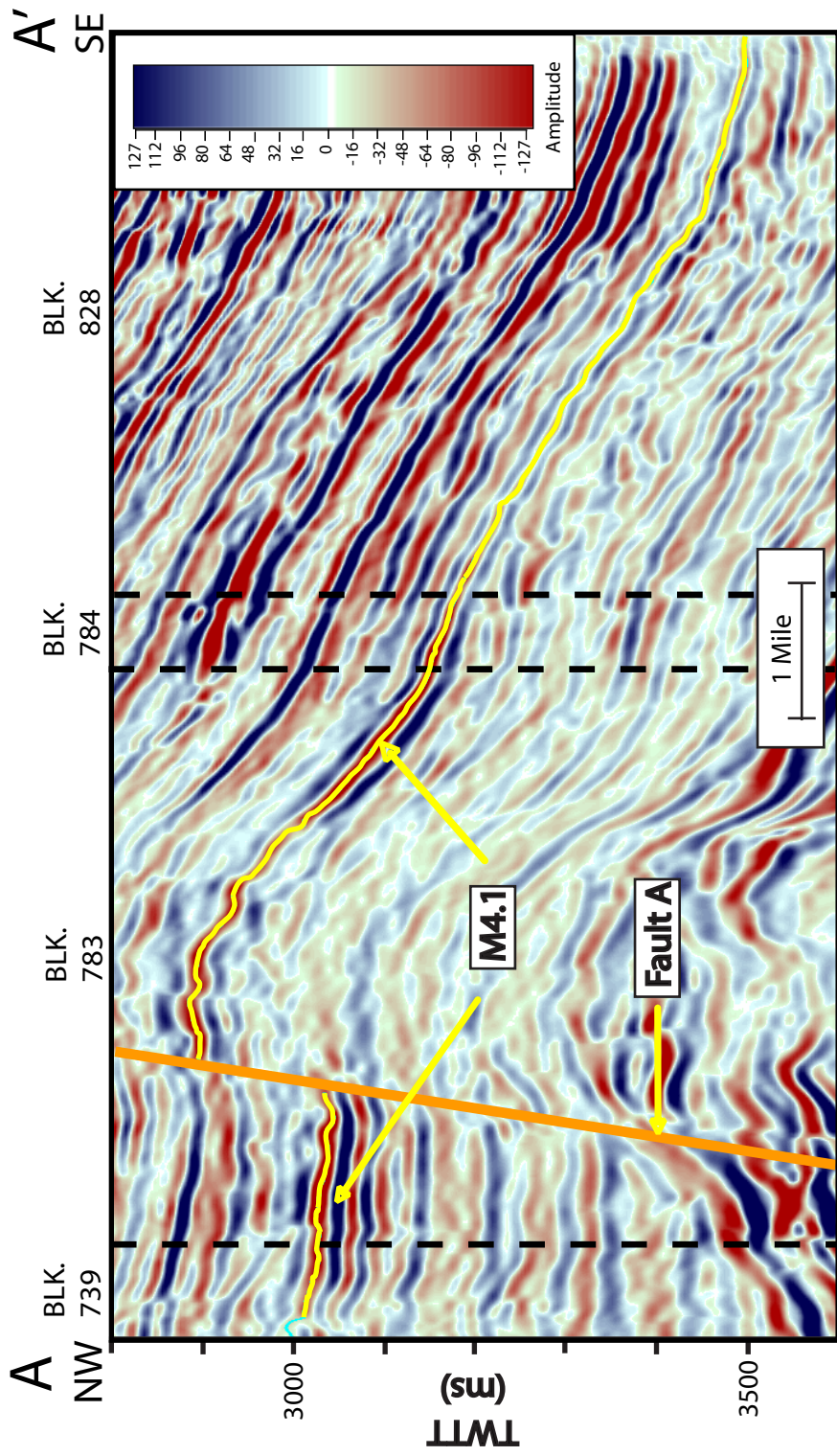
Figure 4: Seismic cross-section AA' (Located in Figure 2). The M4.1 is the bright red event delineated with the yellow line. Fault A compartmentalizes the M4.1. Red colors record negative amplitudes while blue records positive amplitudes.
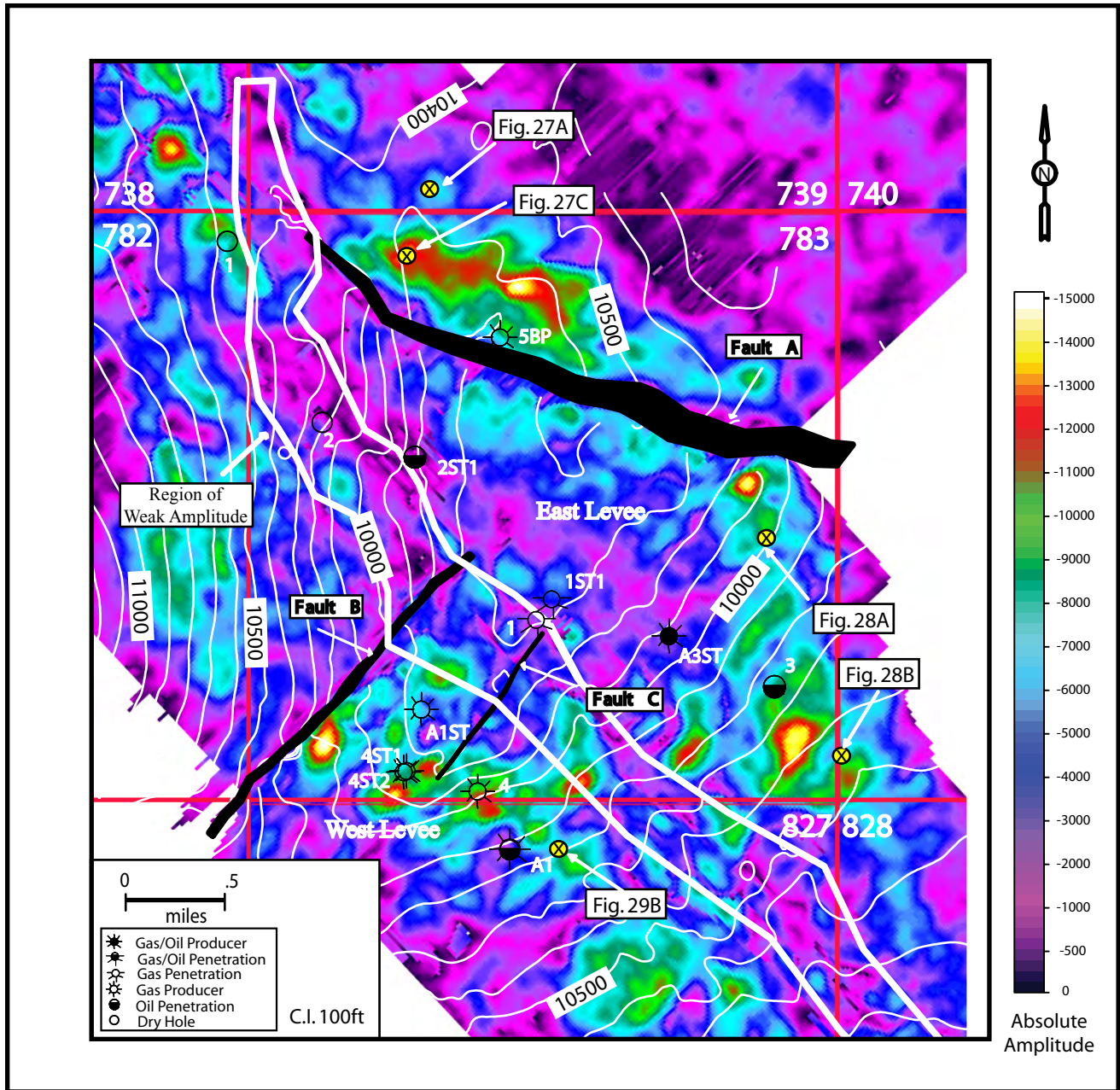
Figure 5: Amplitude extraction of the M4.1, overlain on a structure map of the top of the M4.1. Large negative amplitudes generally indicate hydrocarbon bearing regions. Smaller negative amplitudes represent either zones where water fills the pores or where the reservoir sand has thinned. A trend of low amplitudes is outlined in white and is interpreted to indicate the Channel location. Locations of seismic trace extractions in Figures 27-29 are also labeled.
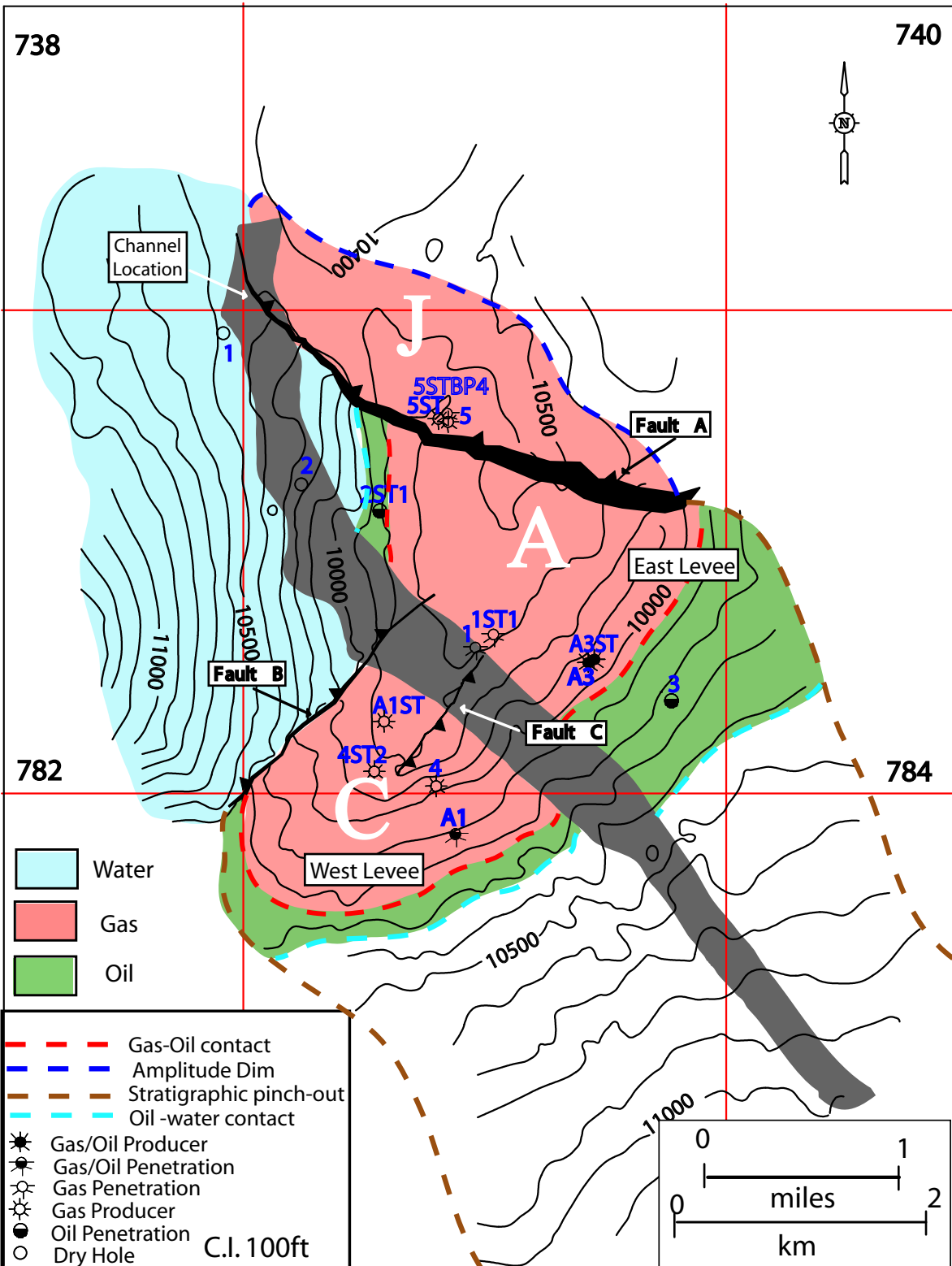
Figure 6: Structure map to the top of the M4.1, overlain by fluid distribution map (modified from Enunwa et. al., in press). This map shows the varying fluid contacts in the M4.1 reservoir. The three compartments of the M4.1 are denoted.

10

well control (Fig. 7). A region of M4.1 thinning trends NW-SE and is thinner than its flanking regions (Fig. 7). This thinning coincides with the region of weak amplitudes (Fig. 5), and we interpret the linear feature seen in both maps to record the location of the Channel in this channel-levee system. The thicker flanks seen to the east and west of the Channel represent the East and West Levees respectively.

1.4 M4.1 Acoustic Response

1.4.1 Introduction

Seismic data were analyzed at several well locations in order to characterize the amplitude behavior of the M4.1 sand (Table 1). At each well, velocity and density logs, and checkshot data, are used to correlate the sand to the seismic response. Synthetic seismograms were generated to compare the observed seismic and predicted seismic responses. The synthetics were generated by convolving a zero phase, 25Hz Ricker wavelet with an integrated reflection coefficient series based on impedance data from each well. A peak frequency of 25Hz was chosen based on frequency domain analysis of the seismic data. See Appendix A for a detailed discussion and example of the synthetic techniques used.

1.4.2 Acoustic Response of Type Wells

A well was chosen for study from each of the three geographical settings present in the M4.1: Channel (783-2), East Levee (783-3), and West Levee (783-4ST2). Well 783-2 is located in the Channel and contains a water-saturated M4.1 (Fig. 6). At this location, the M4.1 is imaged as a single seismic trough (Fig. 8). There is a sharp
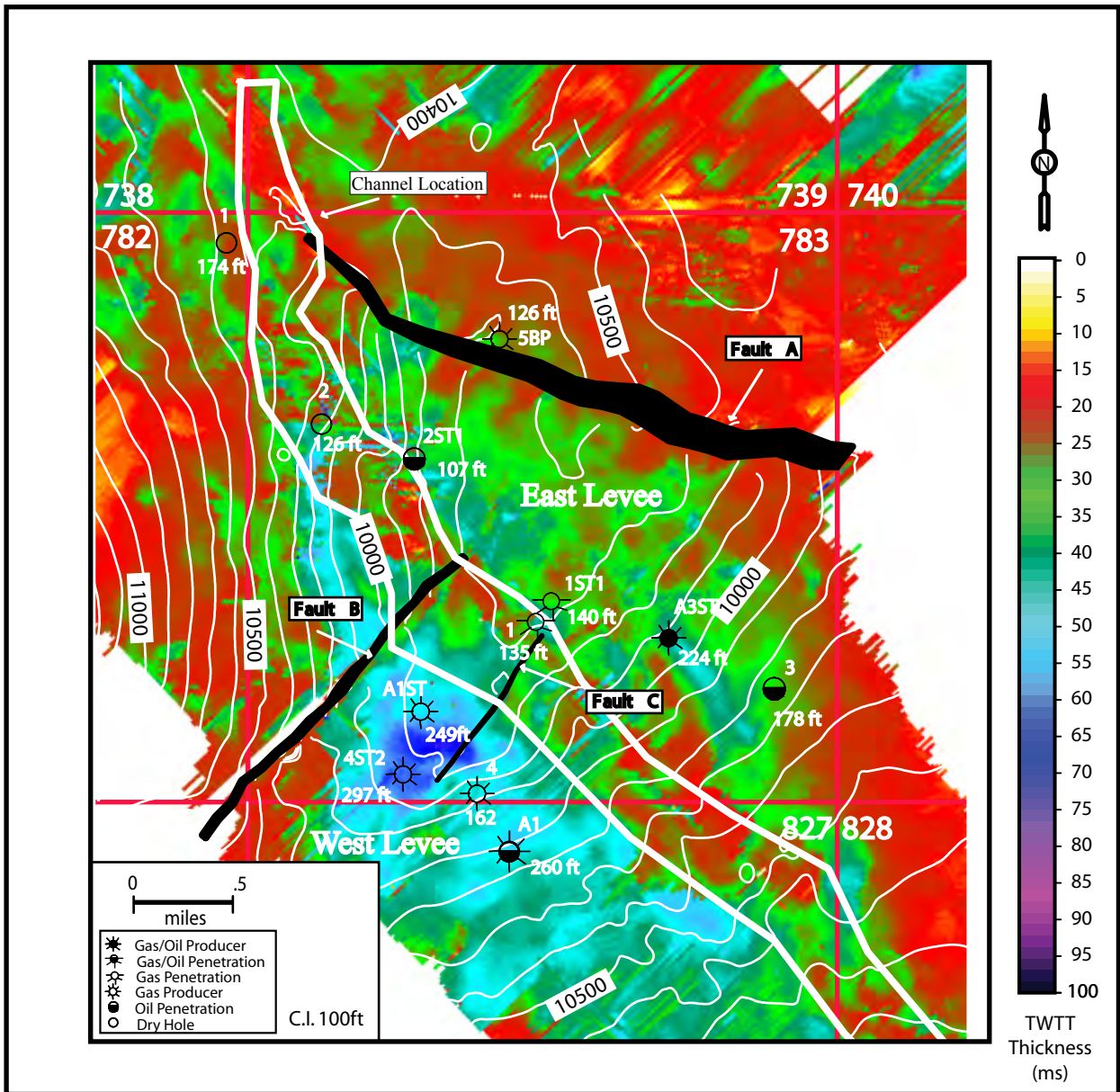
Figure 7: Two-way travel time (TWTT) thickness map of the M4.1 created by calculating the distance between upper and lower zero-crossings in time. Gross sand thickness is posted at each well penetration.

Well	Seismic Amplitude	Location	Fluid Type	Sand Thickness (ft.)
783-4	-12583	W. Levee	Gas	162
783-3	-9141	E. Levee	Oil	178
783-5BP	-8506	E. Levee	Gas	126
783-4ST1	-8492	W. Levee	Gas	290
783-4ST2	-8492	W. Levee	Gas	297
783-1ST1	-3954	E. Levee	Gas	140
783-1	-3712	Channel	Gas	135
783-2ST1	-3613	E. Levee	Oil	107
783-2	-1770	Channel	Water	126

Table 1: List of wells selected for amplitude analysis. The location, fluid type, sand thickness and peak negative amplitude (observed in seismic) is shown for each well location. The wells have been displayed in order of decreasing absolute amplitude.
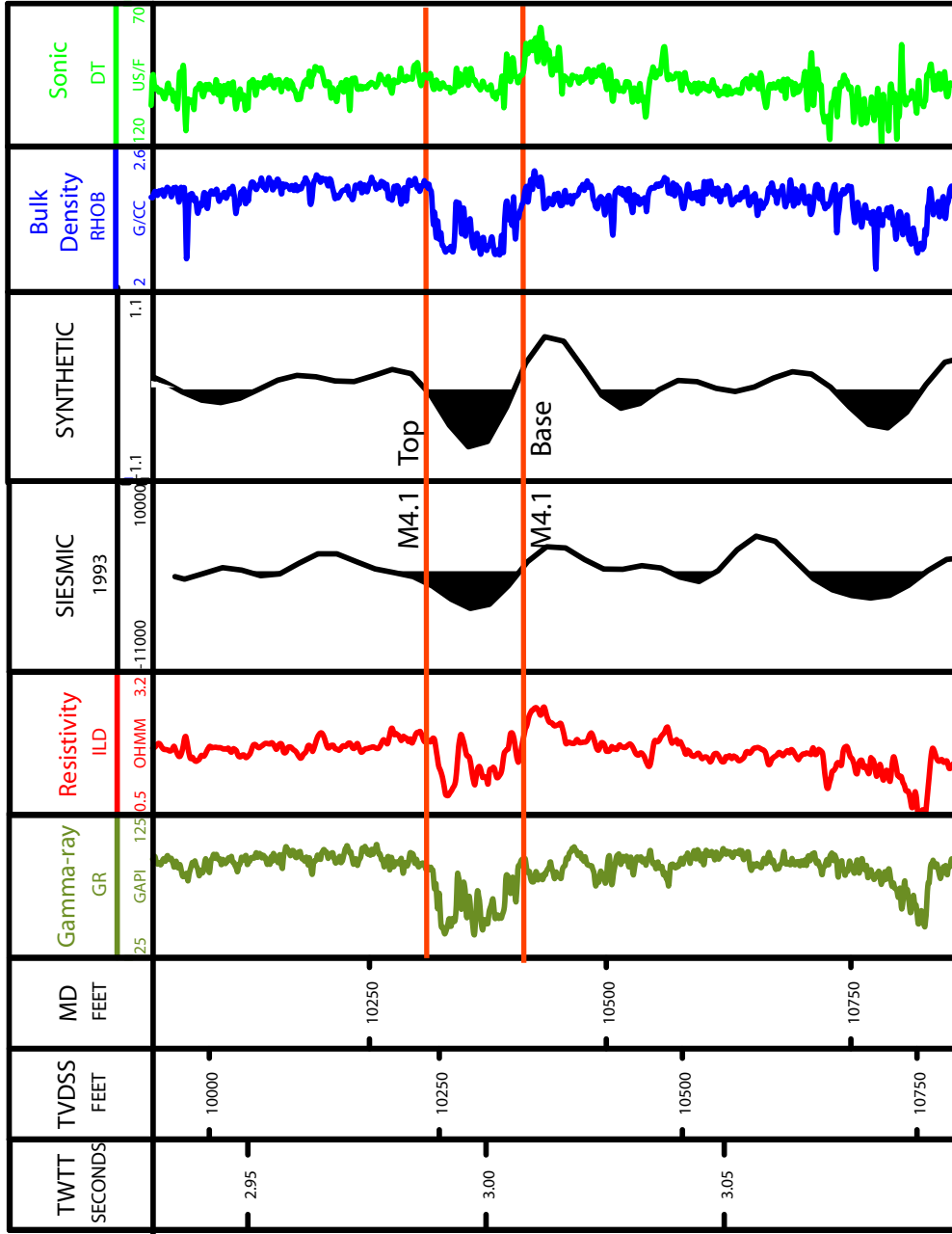
Figure 8: Welltie for the 783-2 showing the following well logs: gamma-ray (GR), resistivity (ILD), bulk density (RHOB), and sonic (DT). An extracted seismic trace and synthetic trace at the well location is also shown. The extracted seismic was shifted down 6 ms. Well 783-2 is located in Figure 2.

14

decrease in gamma-ray, resistivity, and density at the top of the M4.1 in this well. Acoustic impedance decreases with depth as you enter the M4.1 and results in a reflection coefficient (RFC) of ~ -0.063 (Table 2). The amplitude expression at well 783-2 is the weakest observed at studied well locations. Synthetic modeling of the M4.1 at well 783-2 images the sand as a single trough (Fig. 8).

The M4.1 at well 783-3 contains oil and is located in the East Levee, (Fig. 6). There are two distinct sand layers within the M4.1 at this well location (Fig. 9). The upper layer shows a gradual decrease in gamma-ray and a gradual increase in resistivity as you move down through the M4.1. At approximately 10,360ft (TVDSS), there is a sharp increase in gamma-ray and decrease in resistivity. This is followed by another drop in gamma-ray and increase in resistivity which represents the lower layer. The M4.1 is imaged seismically as one trough, because the individual sands are too thin to be imaged separately. Upon entering the M4.1, acoustic impedance decreases and results in an RFC of ~ -0.083 (Table 2). The amplitude expression of the M4.1 at this location is very strong and represents one of the brightest amplitudes recorded. Synthetic modeling of well 783-3 images the sand as a single trough (Fig. 9).

The 783-4ST2 well penetrates a gas-saturated M4.1 and is located in the West Levee (Fig. 6). At this location, the M4.1 is imaged as two troughs (Fig. 10). The sand at this location is thick enough for the seismic to image the acoustic impedance contrast at both the upper and lower sand-shale interfaces separately (Fig. 10). Gamma-ray logs shows a steady reading while the resistivity exhibits a gradual increase as you move down through the sand. As you enter the M4.1 at this location there is a decrease in

Well	Fluid	M4.1 Top Δ Impedance (kg/m^{2}s)	RFC
783-5BP	Gas	2.22E+06	-0.131
783-1	Gas	1.60E+06	-0.113
783-3	Oil	1.22E+06	-0.083
783-1ST	Gas	1.13E+06	-0.075
783-2ST	Oil	9.86E+05	-0.064
783-2	Water	9.34E+05	-0.063
783-4	Gas	8.59E+05	-0.059
783-4ST1	Gas	8.20E+05	-0.060
782-1	Water	5.83E+05	-0.037
783-4ST2	Gas	4.07E+05	-0.029

Table 2: List of impedance contrasts as you enter the top of the M4.1 at each well location. The reflection coefficient produced when entering the M4.1 sand is also shown. Wells are listed in order of decreasing impedance change. In-situ fluid type is also listed.
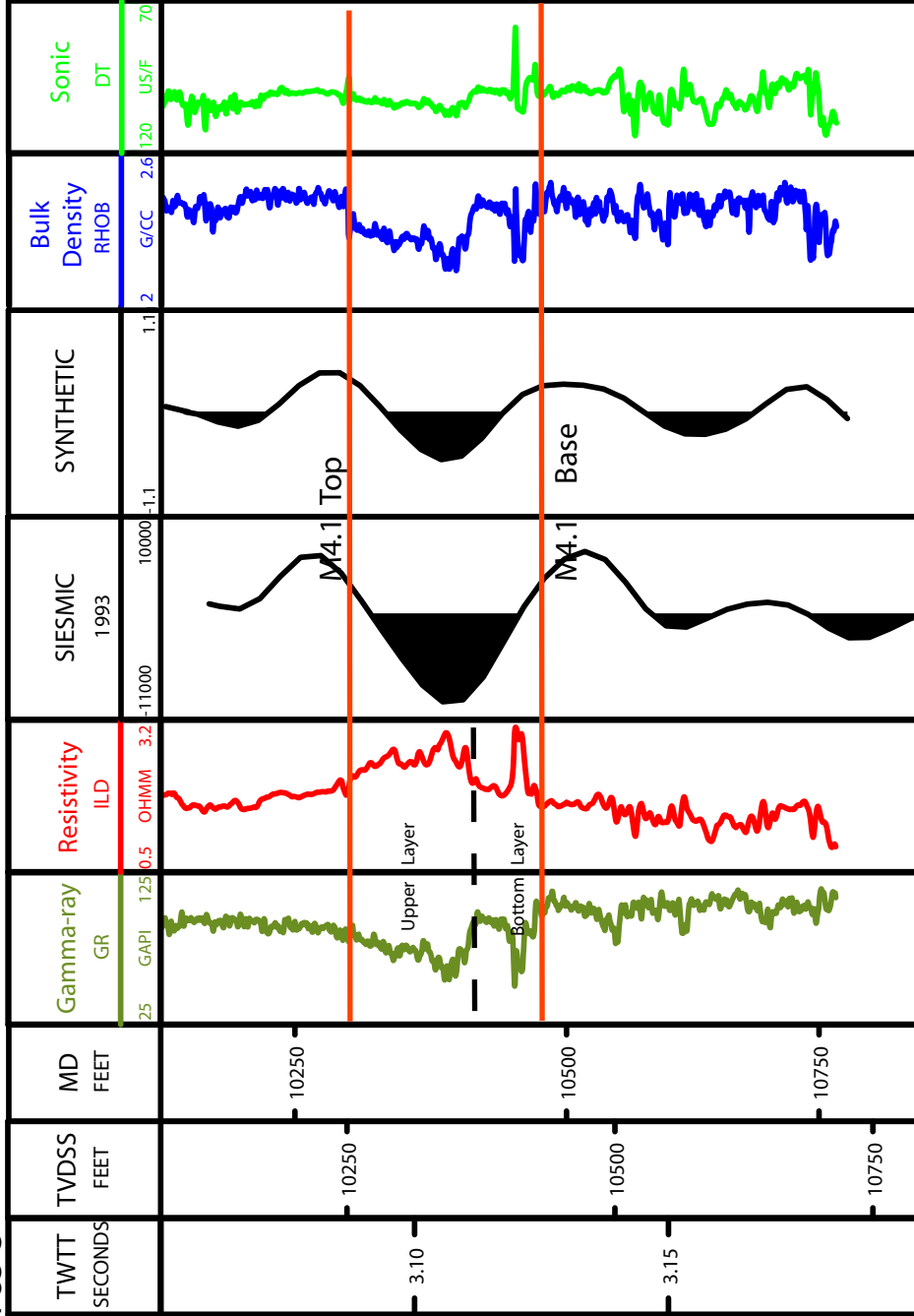
Figure 9: Welltie for the 783-3 showing the following well logs: gamma-ray (GR), resistivity (ILD), bulk density (RHOB), and sonic (DT). An extracted seismic trace and synthetic trace at the well location is also shown. The extracted seismic was shifted down 10 ms. Well 783-3 is located in Figure 2.

17
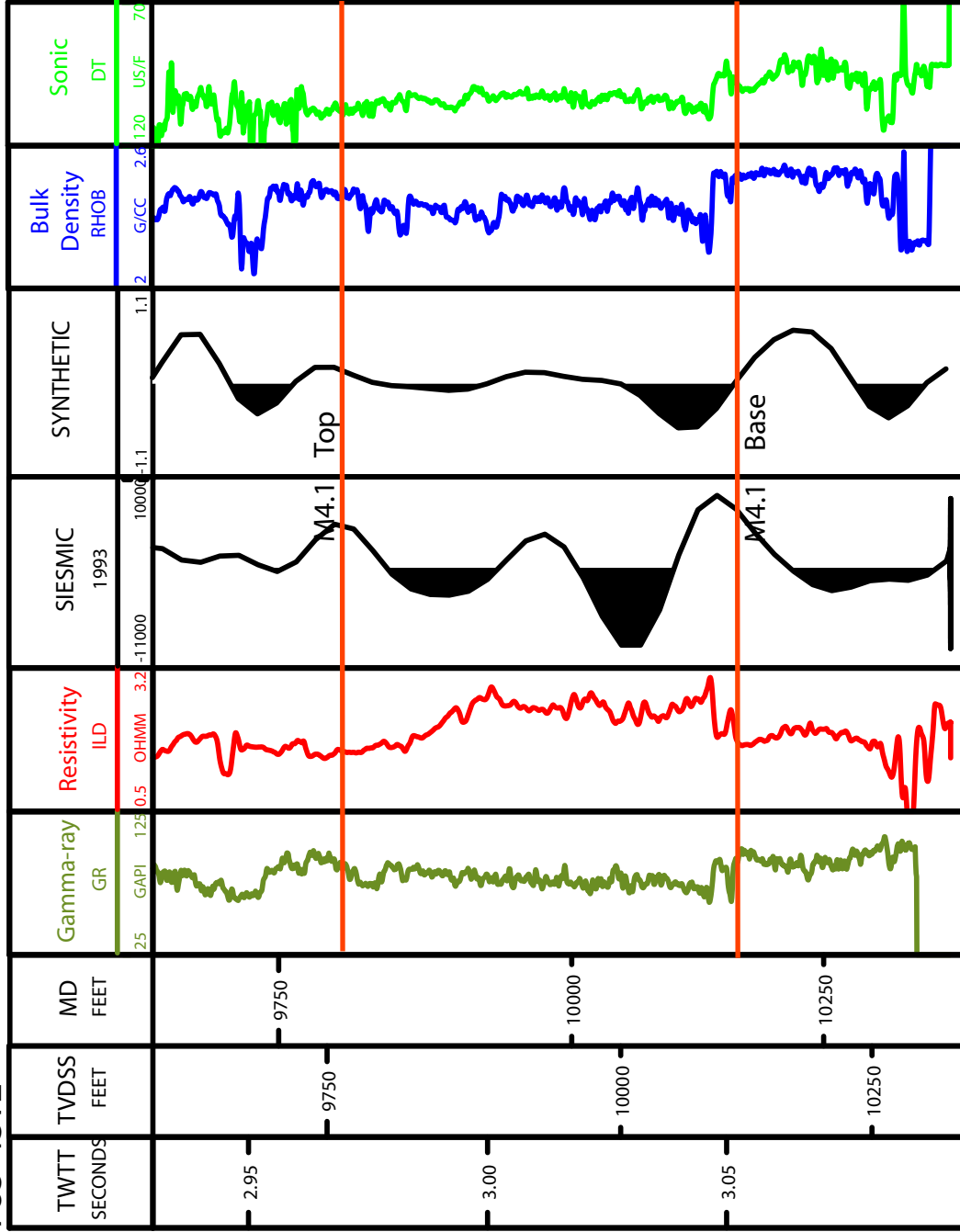
Figure 10: Welltie for the 783-4ST2 showing the following well logs: gamma-ray (GR), resistivity (ILD), bulk density (RHOB), and sonic (DT). An extracted seismic trace and synthetic trace at the well location is also shown. Well 783-4ST2 is located in Figure 2.

acoustic impedance which results in a RFC of -0.029 (Table 2). Synthetic modeling of the M4.1 at well 783-4ST2 images the sand as two separate troughs (Fig. 10).

1.4.3 Acoustic Discussion

The acoustic response of the M4.1 is controlled by three factors: fluid type, impedance contrast at the sand-shale interface, and sand thickness. The type of fluid present affects the impedance properties of the sand which determine acoustic behavior. The impedance contrast between the M4.1 and bounding shales also determines what type of acoustic signature will be expressed. Acoustic response is also a function of sand thickness and tuning effects. Tuning, as described by Widess (1973), is the termed used to describe the effects of bed thickness on seismic signature. For bed thicknesses on the order of a seismic wavelength or larger, there is little interference between the wavelets that record the top and bottom of the bed (Brown, 2004). As bed thickness becomes smaller than the seismic wavelength, the wavelet will experience various combinations of constructive and destructive interference. Widess (1973) showed that the amplitude of the composite wavelet reaches a maximum when bed thickness is approximately one quarter the seismic wavelength, this is known as the tuning thickness. The tuning phenomenon is usually described by graphs such as the one found in Figure 11A. This is a plot of maximum amplitude versus increasing bed thickness, with maximum amplitude occurring at approximately 175ft (Fig. 11A).

We discuss the observed amplitude behavior of the M4.1 in four locations: Channel, East Levee north of Fault A, East Levee south of Fault A, and West Levee south of Fault B (Fig. 5). The Channel has two well penetrations: 783-1 and 783-2 (Fig.
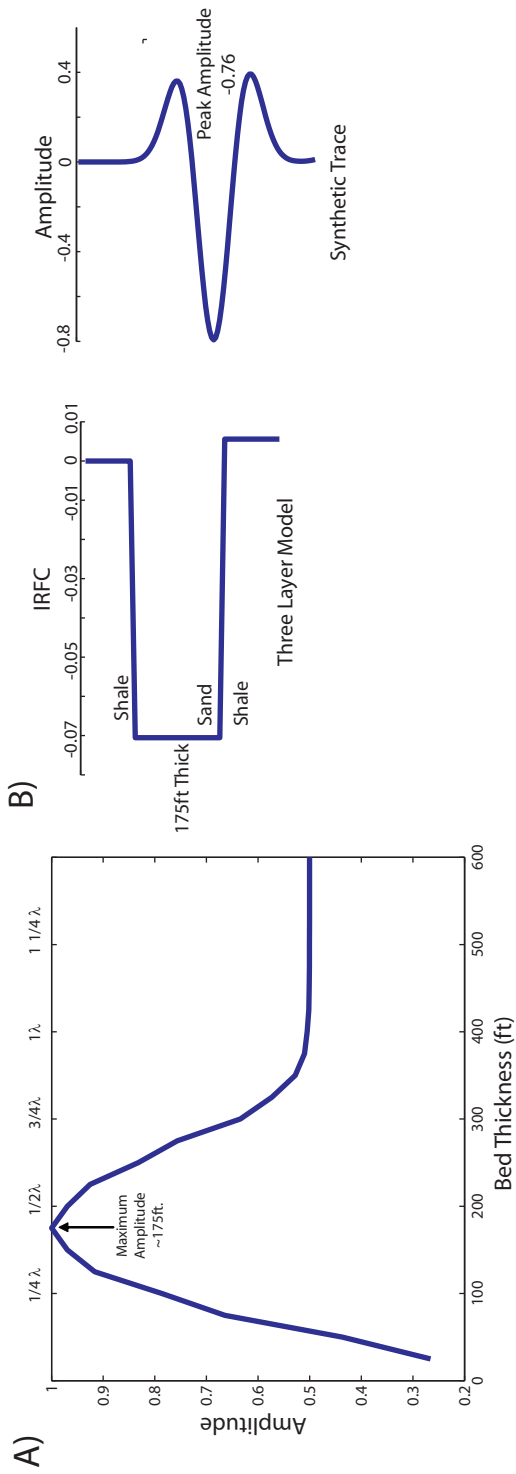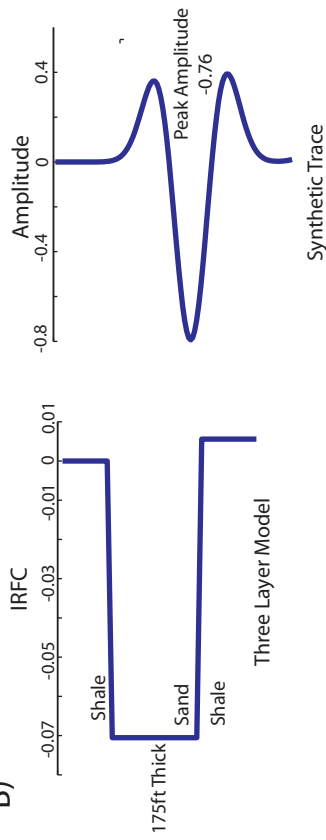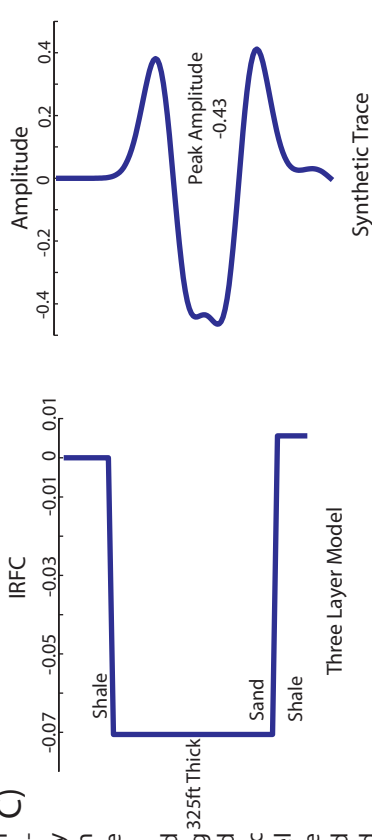
Figure 11: A) Peak amplitude versus bed thickness. Maximum amplitude occurs at approximately 175ft. The amplitude values plotted represent the peak negative amplitude of each synthetic seismic trace divided by the largest negative amplitude (-0.76). Synthetic seismic traces were generated by convolving a zero phase, 25Hz Ricker wavelet with an integrated reflection coefficient (IRFC) series based on a three layer model (Fig. 11B). Modeled bed thickness ranges from 25-600ft. B) Three-layer model consisting of a sand bed situated between two shale beds. The IRFC series was generated using average values of velocity and bulk density for the M4.1 sand and bounding shales. Sand thickness is 175 feet. C) Three-layer model consists of a sand bed situated between two shale beds. The IRFC series was generated using average values of velocity and bulk density for the M4.1 sand (9700 ft/s & 2.28 g/cc) and bounding shales (10,400 ft/s & 2.46 g/cc). Sand thickness was is 325 feet. The synthetic seismic trace is shown to the right.

5). Fluid type controls the observed amplitude behavior in the Channel. Well 783-2 contains water and there is a sand thickness of 126ft, whereas 783-1 is gas-saturated and is 135 ft thick. There is a larger impedance drop as you enter the sand in the location of the gas well (783-1) and this results in a larger RFC than at 783-2 (Table 2). The larger RFC caused by the presence of gas is responsible for the stronger amplitude expression that is observed as you move southeast through the Channel (Fig. 5).

The second location we discuss amplitude behavior is around the #5 wells which are located in the East Levee to the north of Fault A and penetrate a gas-saturated M4.1 (Fig. 5). The amplitudes at the #5 wells are controlled by the impedance contrast between the M4.1 and bounding shales. These amplitudes are large relative to all other areas in the East Levee containing gas (Fig. 5). This difference in amplitude expression results from the fact that the sand is cleaner (lower GR) in this region and hence the velocity and density contrast between the sand and bounding shales is much greater. This strong impedance contrast is demonstrated in well 783-5BP (Fig. 12A). Well 783-1ST1 is also gas charged and located in the East Levee, however, the M4.1 in this location is not as clean and therefore there is not as much of a velocity and density contrast (Fig. 12B). This difference in impedance contrast between these two wells corresponds to a difference in RFC of 43% (Table 2). The larger RFC at well 783-5BP results in a stronger amplitude response (Fig. 5). The M4.1 sand at well 783-1ST1 is thicker than at well 783-5BP, however, tuning effects do not play a role in the strong amplitudes present at 783-5BP. The large impedance contrast overcomes tuning effects resulting from the small difference in sand thickness between the two wells.
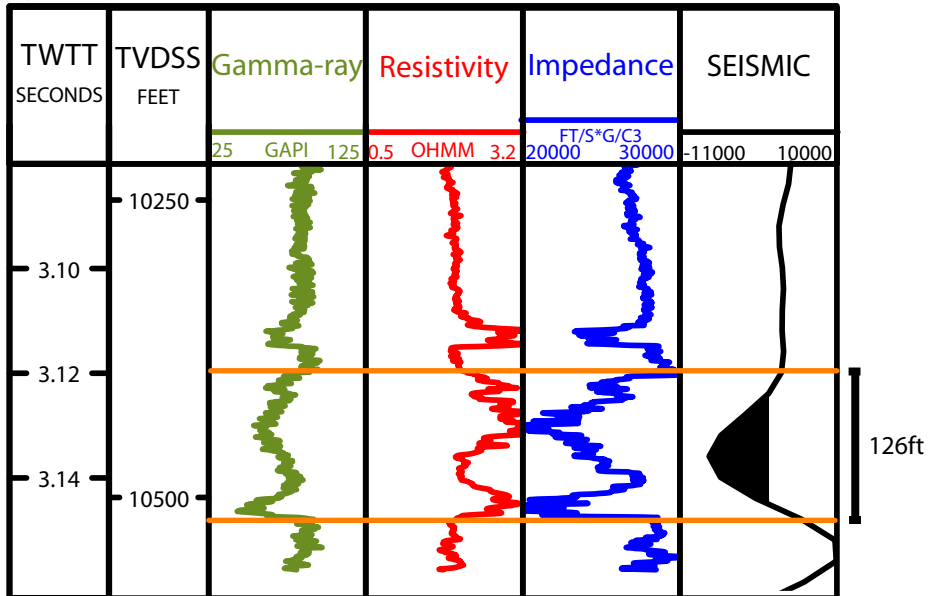
21
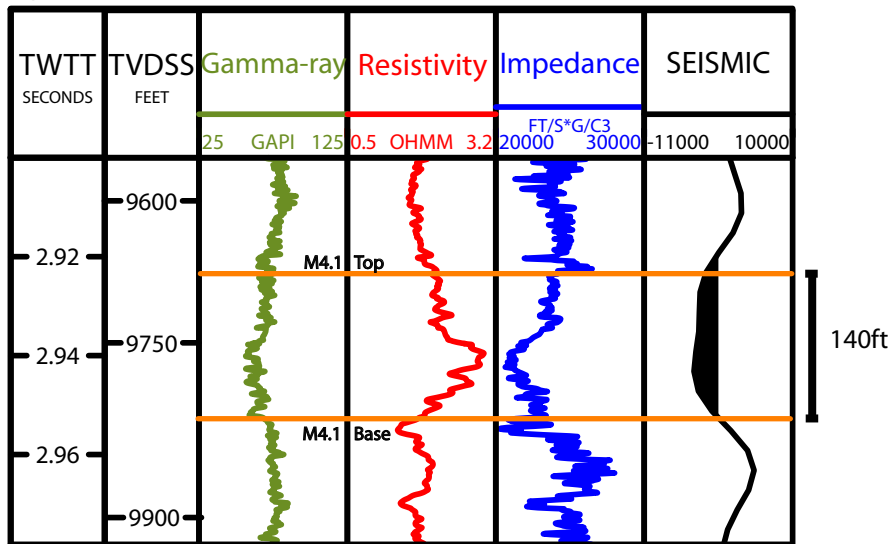
Figure 12: Gamma-ray (GR) log, resistivity (ILD) log, impedance log, and seismic traces for wells: A) 783-5BP and B) 783-1ST1. Well 783-1ST1 is located in the East Levee south of Fault A and well 783-5BP is located in the East Levee north of Fault A. There is a greater impedance contrast when entering and exiting the M4.1 at well 783-5BP relative to 783-1ST1. This difference in impedance contrast between the wells corresponds to a difference in RFC of 43% and results in the stronger amplitude response observed at well 783-5BP. The extracted seismic traces for wells 783-1ST1 and 783-5BP have been shifted up 8ms and down 100ms respectively. Wells are located in Figure 2.

The third location we discuss amplitude behavior is in the southeast region of the East Levee at well 783-3 (Fig. 5). Oil is present at 783-3 in the M4.1 and the amplitude expression here is larger than all amplitudes produced by gas bearing regions of the M4.1, with the exception of well 783-4 (Table 1). The M4.1 in this location is cleaner than the gas charged locations to the north which results in a greater impedance contrast when entering the M4.1. Analysis of impedance data shows that on average, there is a 35% greater impedance contrast when entering the M4.1 in the location of well 783-3 when compared to gas-saturated wells (Table 2). The presence of a larger impedance contrast at well 783-3 results in a greater RFC, which causes the strong seismic amplitudes observed (Fig. 5). The large amplitudes can also be attributed to the sand thickness being close to the tuning thickness. The sand is 178ft thick at 783-3 which is close to the tuning thickness of 175ft, where the amplitude response is greatest (Fig. 11A).

The final location we discuss amplitude behavior is at the #4 wells in the West Levee (Fig.5). There are three gas bearing wells in this group: 783-4, 783-4ST1, and 783-4ST2. Their observed seismic amplitudes are large when compared to the gas bearing region of the East Levee to the south of Fault A (Table 1). These large amplitudes are the result of increased bed thickness in this portion of the West Levee. Gas bearing wells in the East Levee have similar RFC's when entering the M4.1 (Table 2), however, the increased sand thickness at the #4 wells allows for greater constructive interference between the wavelets that are recording the top and bottom of the sand. This increase in the amount of constructive interference results in a stronger amplitude response.

Tuning effects also impact the amplitude response of the #4 wells relative to each other. The observed amplitude response of the M4.1 in the location of well 783-4 is significantly larger than the amplitudes observed at wells 783-4ST1 and 783-4ST2 (Table 1). The difference in amplitudes results from the fact that the sand is thin at 783-4 relative to the other two wells. Constructive interference generates greater amplitudes as bed thickness approaches 1/4 λ (Widess, 1973). For bed thicknesses greater than 1/4 λ, the maximum possible amplitude falls of due to a decrease in constructive interference. The M4.1 at well 783-4 is approximately 162ft thick, which falls close to the region of maximum amplitude (Fig. 11A). The thicker sands at wells 783-4ST1 and 783-4ST2 cause a decrease in the amount of constructive interference experienced and results in smaller amplitude expressions (Fig. 11A).

1.5 Conclusions

The M4.1 reservoir is a channel-levee system with two distinct lithofacies: the Channel facies and the Levee facies. A region of amplitude dimming that coincides with a region of thinning is interpreted to record the location of the channel. The channel, in conjunction with two large normal faults, compartmentalizes the M4.1. We characterize the acoustic response of the M4.1 reservoir based on amplitude and well-log data analyses. Amplitude response is driven by three main factors: fluid type, impedance contrast at the sand-shale interface, and sand thickness.

Chapter 2

GASSMANN MODEL

Abstract

Gassmann fluid substitution predicts changes in seismic properties of the M4.1 reservoir resulting from production-related effects. Modeling of gas exsolution due to a pressure decline below bubble point predicts a 25% increase in RFC for an increase in gas saturation to 10%. Synthetic modeling of this increase in RFC predicts a 40-72% increase in seismic amplitude. Modeling predicts that oil-swept areas will exhibit a 25% decrease in reflection coefficient (RFC). Synthetic seismic modeling of this decrease in RFC results in a 30% decrease in seismic amplitude. Compaction due to a pressure decline causes a 3% increase in dry frame modulus which causes a 4% decrease in seismic amplitude. Compaction also results in a 0.5% decrease in porosity which causes a 3% decrease in amplitude. We initialize the Gassmann fluid substitution model by defining average rock and fluid properties for an oil- and gas-saturated M4.1.

2.1 Introduction

Gassmann fluid substitution can be used to predict production-related changes in acoustic velocity of the M4.1 reservoir. These changes are modeled using the relationship between a rock's bulk P-wave modulus (M) and its corresponding dry frame (K_{dry}), grain (K_s), and pore fluid moduli (K_w, K_o, K_g) (Gassmann, 1951). The methodology employed is similar to that performed in studies of the Bullwinkle and South Timbalier fields, Gulf of Mexico (Comisky, 2002; Burkhart, 1997). The parameters necessary to implement Gassmann's equations are the moduli of the dry rock (K_{dry}), reservoir fluids (K_w, K_o, K_g), and solid grains (K_s). If these are properties known, the bulk P-wave modulus (M) for the saturated rock under any pressure and saturation conditions can be predicted.

Changes in fluid saturation during production, such as an increase in water saturation (S_w) resulting from water sweep, can cause a significant increase in acoustic velocity (Gregory, 1976). As production occurs, the reservoir can experience a drop in pressure which causes the formation to compact and alter rock properties. When compaction occurs the rock will stiffen, resulting in an increase in the dry frame modulus (K_{dry}) (Landro, 2001). In addition, the increase in vertical effective stress will cause a decrease in porosity (Landro, 2001). This decrease in porosity and increase in dry frame modulus cause an increase in acoustic velocity (Wyllie et al., 1956; Zhang et al., 2000). A decline in reservoir pressure below the bubble point can result in gas exsolution in the oil phase of the reservoir. Introduction of gas into the system causes a significant drop in acoustic velocity and bulk density (Domenico, 1977).

2.2 Overview of the Gassmann Model

Gassmann theory (Gassmann, 1951) relates the saturated rock's bulk p-wave modulus (M) to dry frame (K_{dry}), solid grain (K_s), and pore fluid (K_{fl}) moduli and porosity (ϕ) in the following manner:

$$M = SK_{dry} + \frac{\left(1 - \frac{K_{dry}}{K_s}\right)^2}{\frac{\phi}{K_{fl}} + \frac{(1-\phi)}{K_s} + \frac{K_{dry}}{K_s^2}} . \qquad \text{Equation 1}$$

S depends on the dry rock Poisson's Ratio (v);

$$S = \frac{3(1-\upsilon)}{1+\upsilon} . \qquad \text{Equation 2}$$

K_{fl} is the modulus of the composite reservoir fluid and can be obtained using Wood's equation (Wood, 1941):

$$\frac{1}{K_{fl}} = \frac{S_w}{K_w} + \frac{S_o}{K_o} + \frac{S_g}{K_g} . \qquad \text{Equation 3}$$

K_{dry} is initially unknown and is determined using a method developed by Benson (1999). When saturated bulk modulus (M) and bulk density are known, we can use Equation 4 to solve for the saturated rock's acoustic velocity.

$$V_p = \sqrt{\frac{M}{\rho_b}} . \qquad \text{Equation 4}$$

There are several assumptions which are made when applying the Gassmann equations to the study of porous rocks. First, the rock, both its matrix and frame, are

macroscopically homogenous. Second, all the pores are interconnected and in communication. Third, the pores are filled with a frictionless fluid. Fourth, the rock-fluid system is closed, meaning drainage does not occur. Finally, the pore fluid does not interact with the solid in a manner that causes either softening or hardening of the frame (Gassmann, 1951).

2.3 M4.1 Elastic Parameters

It is first necessary to provide a static characterization of the elastic rock and fluid properties under in-situ conditions. The necessary inputs for this characterization are the dry rock (K_{dry}), solid grain (K_s), fluid moduli (K_w, K_o, K_g), fluid density (ρ_f), and Poisson's ratio (ν). Poisson's ratio (ν) is unknown and assumed to be 0.18 based on previous studies (Table 3) (Spencer et al., 1994). Fluid densities for water (1.057 g/cc), oil (0.7628 g/cc), and gas (0.21 g/cc) were calculated based on PVT and fluid sample analyses from the M4.1 reservoir (Table 3). The bulk modulus for a solid quartz grain (K_s) is 38GPa (Table 3). The fluid moduli for water (K_w) and gas (K_g), 2.8GPa and 55MPa respectively, were based on compressibility data available (Table 3). The fluid modulus for oil (K_{oil}), 947MPa (Table 3), was determined using correlations between in-situ pressure and temperature conditions, API number, and p-wave velocity (Appendix B). These parameters are assumed constant and independent of well location (Table 3). K_{dry}, the dry rock modulus, is determined at each well location using a method developed by Benson (1999) (Appendix B). The calculated K_{dry} values at each well location are found in Appendix B (Table B2) and range between 8.3-9.8GPa for an oil-saturated M4.1 and 8.5-11.2 for a gas-saturated M4.1. We define an average K_{dry} for an oil-saturated

Parameter	Description	Value
v	poissson's ratio	0.18
ρ_w	water density	1.057 g/cc
ρ_o	oil density	0.7628 g/cc
ρ_g	gas density	0.21 g/cc
K_s	qtz. grain modulus	38 MPa
K_w	water modulus	2.837 GPa
K_o	oil modulus	947 MPa
K_g	gas modulus	55 MPa

Table 3: List of elastic rock and fluid constants used in Gassmann modeling.

sand (9GPa) and a gas-saturated sand (10GPa) based on these values (Table 4). We use the average rock and fluid properties found in Table 4 to initialize the Gassmann fluid substitution model.

2.4 Gassmann Model

2.4.1 Introduction

We use Gassmann modeling to show the affects of production on the acoustic properties of the M4.1 sand. We model changes in velocity, bulk density, impedance and RFC based on five scenarios. First, we model increasing water saturation in an oil-water system. Second, we model increasing oil saturation in a gas-oil system. Third, we simulate gas exsolution out of the oil phase in an original oil-water system resulting from a decline in reservoir pressure below bubble point. Finally, we model increasing dry frame modulus (K_{dry}) and decreasing porosity, both caused by an increase in effective stress. The modeled impedances are then used to predict the amplitude response of the modeled scenarios.

2.4.2 Gassmann Modeling

1) Increasing water saturation

We show the effect of increasing water saturation (S_w) on velocity, bulk density, impedance, and RFC in an oil- and gas-saturated region. Water saturation is increased from initial saturation of 25% to S_w=80%. Dry frame modulus (K_{dry}) and porosity (Φ) are held constant. First, we model increasing water saturation (S_w) in an oil-water system. As S_w increases, velocity, bulk density, and impedance increase (Fig. 13A & 13C). We

Parameter	Oil Saturated M4.1	Gas Saturated M4.1
Φ	29%	27%
S_w	26%	27%
S_{hyd}	74%	73%
ρ_w	1.057 g/cc	1.057 g/cc
ρ_o	0.7628 g/cc	0.7628 g/cc
ρ_g	0.21 g/cc	0.21 g/cc
K_w	2.837 GPa	2.837 GPa
K_o	947 MPa	947 MPa
K_g	55 MPa	55 MPa
K_s	38 GPa	38 GPa
K_{dry}	9 GPa	10 GPa
ν	0.18	0.18

Table 4: Average rock and fluid properties for both an oil-saturated and gas-saturated M4.1. These properties serve as the initial parameters to calibrate the Gassmann fluid substitution model.

calculate the reflection coefficient (RFC) at the top of the M4.1 as a function of water saturation and the average impedance of the overlying shale (8.04×10^6 kg/m^{2}s) (Fig. 13D). As water saturation increases from a residual saturation of 25% to 80%, the magnitude of the RFC decreases 31% from -0.074 to -0.051 (Fig. 13D).

When water replaces gas and no oil is present, velocity first decreases and then increases (Fig. 14A). This happens because as S_w increases, bulk density increases more rapidly than the bulk modulus (M) does (Fig. 14B). As S_w increases, despite the decrease in velocity, impedance still increases (Fig. 14C). We estimate RFC at the top of the M4.1 as a function of water saturation and the average impedance of the overlying shales in the gas bearing regions (7.96×10^6 kg/m^{2}s) (Fig. 14D). As water saturation increases from initial saturation to 80%, the magnitude of RFC decreases 25% from -0.075 to -0.055 (Fig. 14D)

2) Increasing oil saturation in a gas-oil system

We model changes in the acoustic properties of a M4.1 reservoir that experiences an increase in oil saturation. This model could simulate the up-dip movement of an oil rim into a gas zone. We increase oil saturation (S_o) from zero to 65%, while gas saturation (S_g) is decreased from 75% to 10%. Water saturation (S_w) is held constant at 25%. We use the average rock and fluid properties for a gas-saturated M4.1 reservoir (Table 4) to initialize the fluid substitution model. Dry frame modulus (K_{dry}) and porosity (Φ) are held constant. There is a decrease in velocity as oil saturation increases to approximately 55% (Fig. 15A). As in the previous example, the decrease in velocity results because the bulk density is increasing faster than the bulk modulus (M) (Fig.

Figure 13: Modeled effects of increasing water saturation on the following acoustic properties for an oil-saturated M4.1: A) velocity & bulk density, B) bulk density & bulk modulus, C) impedance, and D) reflection coefficient (RFC). Velocity, bulk density, bulk modulus, and impedance all increase as water saturation increases. D) Predicted RFC at the top of the M4.1 based on a shale impedance of 8.04×10^6 kg/m2s. The RFC decreases 31% as water saturation increases from 26-80%.

Figure 14: Modeled effects of increasing water saturation on the following acoustic properties for a gas-saturated M4.1:A) velocity & bulk density, B) bulk density & bulk modulus, C) impedance, and D) reflection coefficient (RFC). A) Velocity decreases as water saturation increases. This happens because as Sw increases, the rock's bulk density is increasing faster than the bulk modulus (Fig. 14B). Impedance increases as water saturation increases. D) Predicted RFC at the top of the M4.1 based on a shale impedance of 7.9x106 kg/m2s. The RFC decreases 25% as water saturation increases from 27-80%.
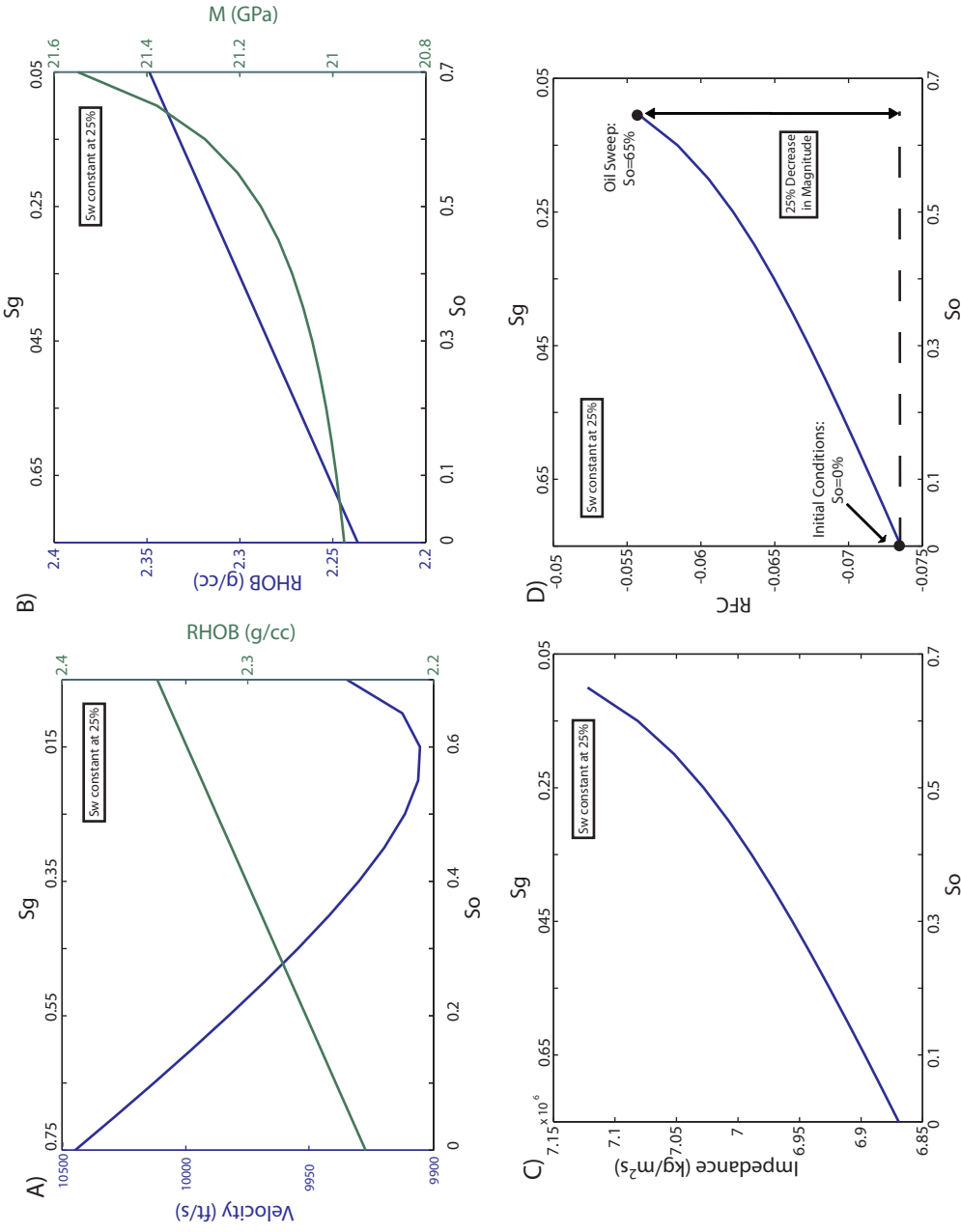
Figure 15: Modeled effects of increasing oil saturation on the following acoustic properties for a gas-saturated M4.1:A) velocity & bulk density, B) bulk density & bulk modulus, C) impedance, and D) reflection coefficient (RFC). A) Velocity decreases as oil saturation increases. This happens because as So increases, the rock's bulk density is increasing faster than the bulk modulus (Fig. 15B). Impedance increases as oil saturation increases. D) Predicted RFC at the top of the M4.1 based on a shale impedance of 7.9x106 kg/m2s. The RFC decreases 25% as oil saturation increases from an initial saturation of zero to So=65%.

15B). As oil saturation increases above 55%, this affect is no longer observed and velocity increases (Fig. 15A). Impedance increases as oil saturation increases (gas saturation decreases) (Fig. 15C). We estimate RFC at the top of the M4.1 as a function of oil saturation and the average impedance of the overlying shales in gas bearing regions $(7.96 \times 10^6 \text{ kg/m}^2\text{s})$ (Fig. 15D). Increasing oil saturation from zero to 65%, results in a 25% decrease in the magnitude of RFC (Fig. 15D).

3) Gas Exsolution

As reservoir pressure decreases below the bubble point, free gas will be released from solution. We simulate the effect of gas exsolution by increasing gas saturation (S_g) from 0% to 75%, while holding water saturation (S_w) constant at 25%. We calculate velocity, bulk density, impedance, and RFC as S_g increases from zero to 75% (Fig. 16). Initially, we see a large drop in acoustic velocity with the introduction of small amounts of gas, S_g=5%-10%, followed by a gradual increase in velocity (Fig. 16A). The increase in velocity at higher gas saturations is due to the bulk density decreasing faster than the bulk modulus (Fig. 16B). Impedance decreases as gas saturation increases (oil saturation decreases) (Fig. 16C). Increasing gas saturation from zero to S_g=10% causes a 25% increase in the magnitude of RFC (Fig. 16D). A small introduction of gas, approximately 10%, has a significant effect on acoustic properties. As S_g increases beyond 10%, the affect on RFC becomes less significant. For instance, as S_g is increased from 10-50%, RFC only increases by 15% (Fig. 16D).
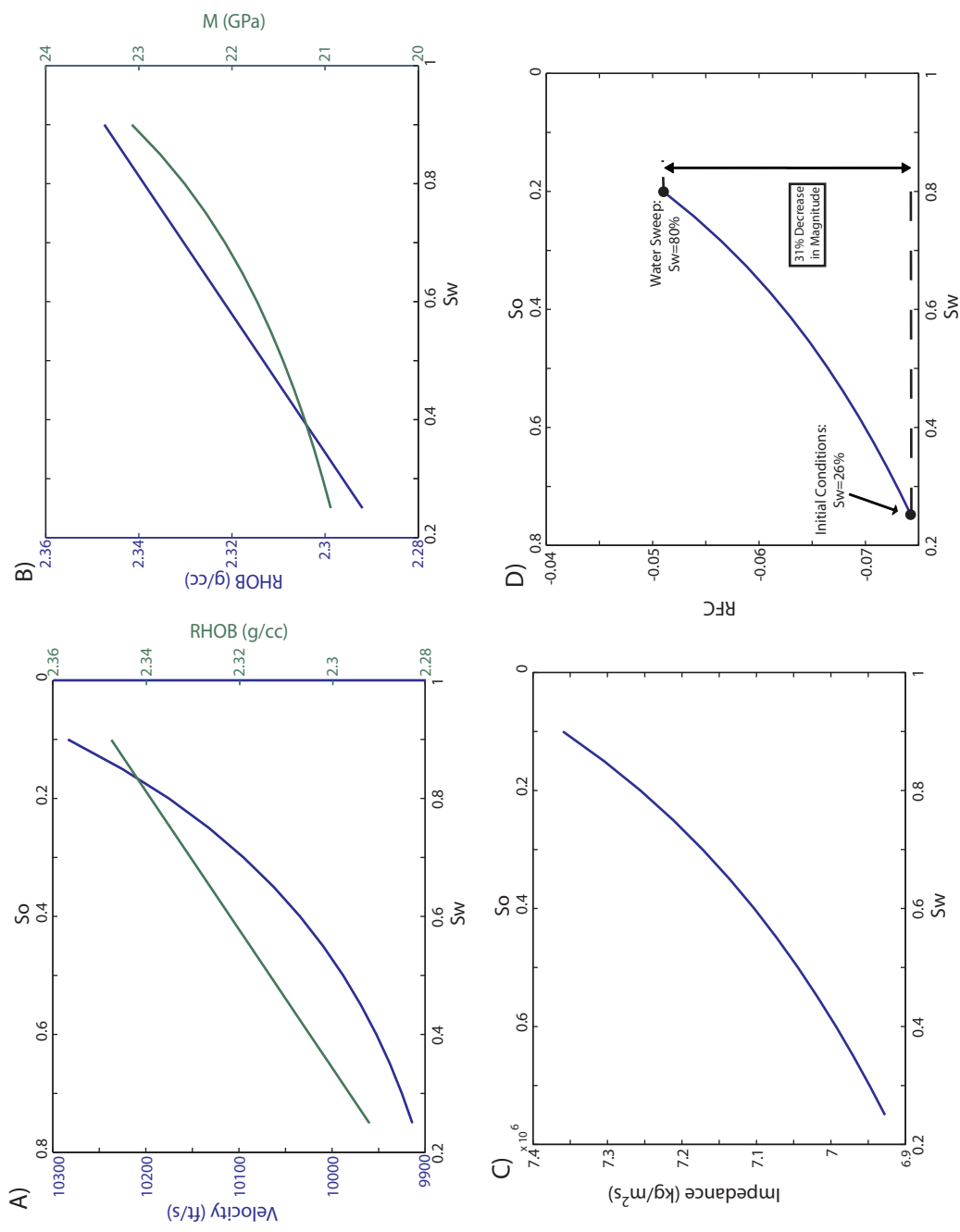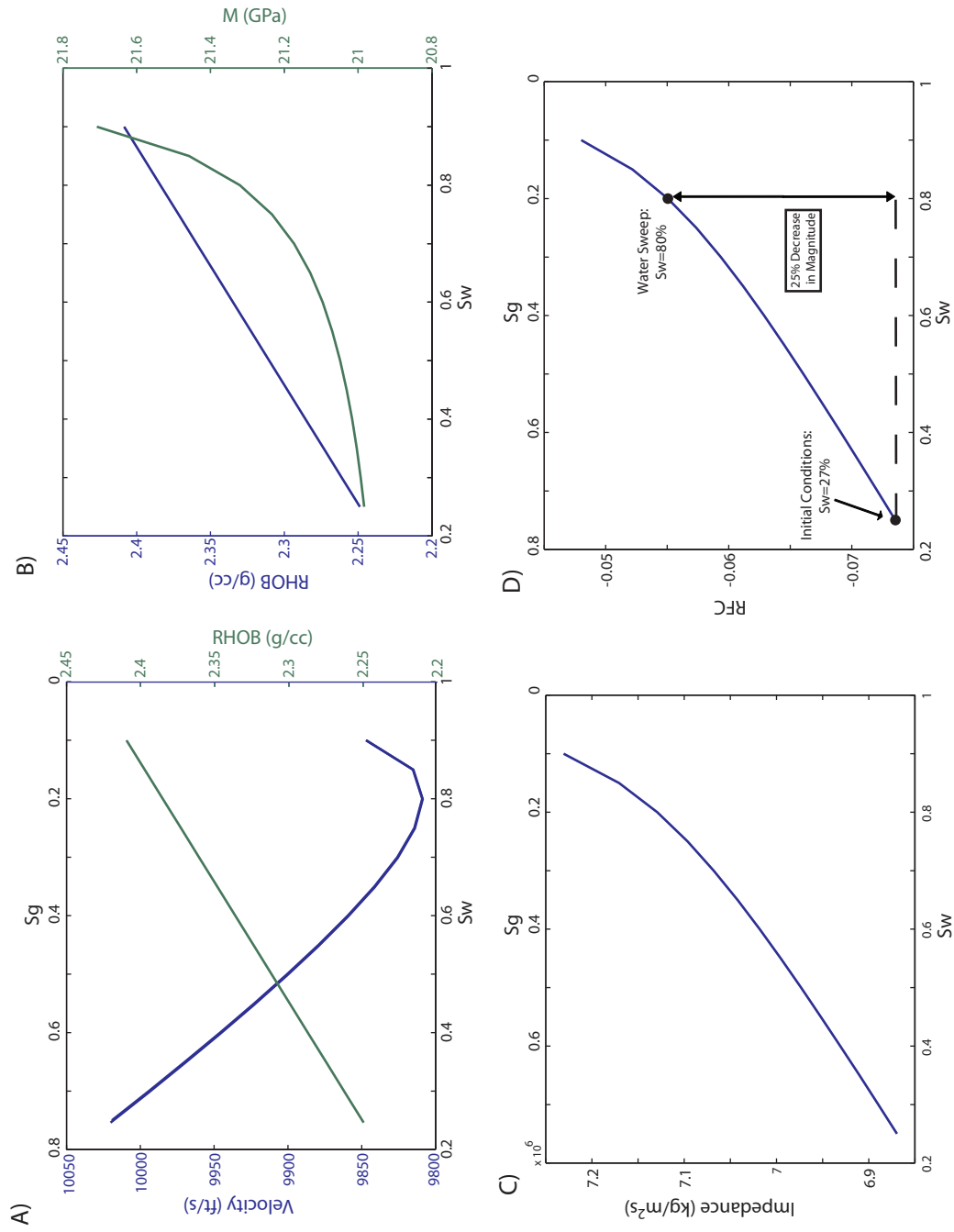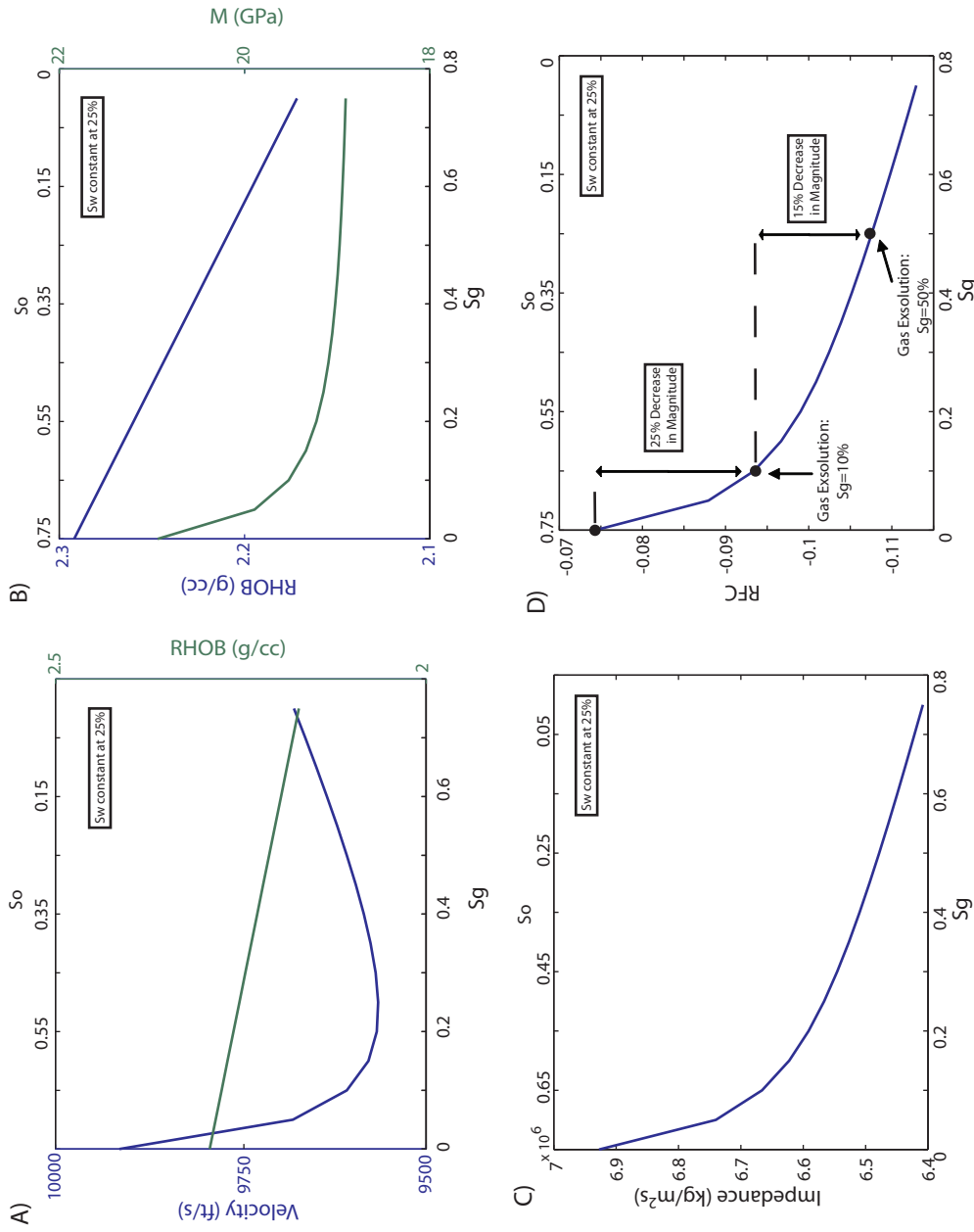
Figure 16: Modeled effects of increasing gas saturation on the following acoustic properties for an oil-saturated M4.1: A) velocity & bulk density, B) bulk density & bulk modulus, C) impedance, and D) reflection coefficient (RFC). A) Velocity decreases sharply at low gas saturations and reaches a minimum at approximately Sg=25%. Beyond Sg=25%, velocity begins to increase. The increase in velocity at higher gas saturations is attributed to the fact that at these saturations, the rock's bulk density is decreasing faster than the bulk modulus (Fig. 15B). C) Impedance shows a large decline at low gas saturations followed by a steady decline at higher saturations. D) Predicted RFC at the top of the M4.1 based on a shale impedance of 8.04x106 kg/m2s. The magnitude of RFC decreases There is a sharp decrease in the magnitude of the RFC at low gas saturations, Sg=5-10%, followed by a more gradual decline at higher saturations. As Sg increases from zero to 10%, we observe a 25% decrease in the magnitude of the RFC. Increasing gas saturation from 10-50% results in 15% decrease in the magnitude of the RFC.

37

4) Increase in K_{dry}

We model the effect of increasing effective stress (σ) on dry bulk modulus (K_{dry}). As production occurs, reservoir pressure decreases, which results in an increase in effective stress experienced by the sand. Zhang and Bentley (2000) used the data of Han et al. (1986) to derive an empirical relationship between K_{dry} and σ, showing that K_{dry} changes as a function of σ based on the following approximation:

$$\frac{dK_{dry}}{d\sigma} = Ae^{B\sigma} .$$

Equation 5

A and B are empirically derived constants, K_{dry} is in GPa and σ is in MPa. Integration of Equation 5 allows for the solution of K_{dry} for any effective stress:

$$K_{dry} = \frac{A}{B}e^{B\sigma} + C ,$$

Equation 6

where C is the constant resulting from integration. The constants A and B are 0.362 and -0.0797, respectively, and were derived based on data used by Blangy (1992). We calculate C based on the initial values of K_{dry} for an oil- and gas-saturated region (Table 4).

The largest decrease in reservoir pressure we observe is 450 psi, based on post-production repeat formation test (RFT) data (Enunwa, 2005). This decrease in pressure results in an increase in effective stress of 3MPa. We use Equation 6 to calculate a new K_{dry} based on this increase in effective pressure (Table 5A). We calculate a new K_{dry} for both an oil- and gas-saturated M4.1 (Table 5A). An increase in effective pressure of 3MPa results in an increase in K_{dry} of 1% for an oil-saturated M4.1 and 2% for a gas-saturated M4.1 (Table 5A). Next, we calculate impedance and RFC based on the new

Fluid	K_{dry} (GPa)	Impedance (kg/m²s)	RFC	Modeled K_{dry} (GPa)	Modeled Imp. (kg/m²s)	Modeled RFC	% Increase In K_{dry}	% Increase in Imp.	% Drop in RFC
Oil	9	6.94E+06	-0.073	9.1	6.95E+06	-0.072	1	0.21	1
Gas	10	6.79E+06	-0.079	10.2	6.85E+06	-0.075	2	0.84	5
						Average=	2	1	3

Table 5A: Modeled changes in dry bulk modulus (Kdry), impedance, and RFC, as a function of increasing effective stress. The constants A and B in Equation 6 are 0.362 and -.0797, respectively, and were derived by Blangy (1992). Four well locations were used in the modeling: 783-1, 783-3, 783-4ST1, and 783-5BP. Each well was modeled with a maximum increase in effective stress of 3MPa.

Fluid	K_{dry} (GPa)	Impedance (kg/m²s)	RFC	Modeled K_{dry} (GPa)	Modeled Imp. (kg/m²s)	Modeled RFC	% Increase In K_{dry}	% Increase in Imp.	% Drop in RFC
Oil	9	6.94E+06	-0.073	9.3	7.02E+06	-0.068	3	1.10	7
Gas	10	6.79E+06	-0.079	10.4	6.92E+06	-0.070	4	1.86	12
						Average=	3	1	10

Table 5B: Modeled changes in dry bulk modulus (Kdry), impedance, and RFC, as a function of increasing effective stress. The constants A and B in Equation 6 are 0.746 and -.0773, respectively, and were derived by Han et al. (1986). Four well locations were used in the modeling: 783-1, 783-3, 783-4ST1, and 783-5BP. Each well was modeled with a maximum increase in effective stress of 3MPa.

value of K_{dry} (Table 5A). Porosity and fluid saturations are held constant (Table 4). Modeling predicts that changes in dry bulk modulus (K_{dry}) resulting from compaction cause a 1% increase in RFC for an oil-saturated M4.1 and a 5% increase for a gas-saturated M4.1 (Table 5A)

This model was also conducted using an alternate set of values for the coefficients A and B (Equation 6), based on data from Han et al. (1986). From these data we obtain values of 0.746 and -0.0773 for A and B, respectively. Using the coefficients derived by Han et al. (1986), an increase in effective pressure of 3MPa results in an average increase in K_{dry} of 3% and 4% for an oil- and gas-saturated sand respectively (Table 5B). Gassmann modeling of these increases in K_{dry} predict a 7% and 12% decrease in RFC magnitude for sand saturated with oil and gas, respectively (Table 5B)

5) Decrease in Porosity

Core samples were taken at several depths throughout the M4.1 at well location 783-4ST2. The porosity of each sample was measured as a function of increasing stress. Data from this petrophysical analysis show that an increase in effective stress of 3MPa causes a decrease in porosity of approximately 0.5%. We model the impact of a 0.5% decrease in porosity on dry frame modulus (K_{dry}) in both an oil- and gas-saturated sand using the following relationship set forth by Mavko et al. (1995),

$$\frac{\phi_0}{K_p} = \frac{1}{K_{dry}} - \frac{1}{K_s} . \qquad \text{Equation 7}$$

Equation 7 relates the initial pore space modulus (K_p) to initial dry frame modulus (K_{dry}), solid grain modulus (K_s) and initial porosity (ϕ_0). Once K_p is calculated using initial conditions, Equation 7 can be re-written to solve for K_{dry} for any change in ϕ:

$$K_{dry_{new}} = \frac{1}{\left[\dfrac{\phi_{new}}{K_p} + \dfrac{1}{K_s} \right]} .$$ Equation 8

Table 6 lists the predicted K_{dry} resulting from a 0.5% decrease in porosity. The new values of K_{dry} and ϕ were then used to calculate impedance and RFC (Table 6). Saturation levels were held constant at initial values (Table 4). Gassmann modeling of a 0.5% decrease in porosity shows an average decrease in RFC magnitude of 1% for both oil- and gas-saturated regions (Table 6).

2.4.3 Modeling Acoustic Response

We now consider the effect of impedance changes on seismic response at several well locations. We model increasing water saturation in both an oil- and gas-saturated M4.1. We model increasing oil saturation in a gas-oil system at well 783-4ST2. Increasing gas saturation resulting from gas exsolution in the oil phase of an oil-water system is modeled at well locations 783-2ST1 and 783-3. We predict changes in rock properties associated with compaction effects and model the impact of increasing dry frame modulus (K_{dry}) and decreasing porosity on seismic response at several well locations.

At each studied well location, within the M4.1 interval, we substitute the original velocity and density logs with the predicted velocities and densities from the

Fluid	Kdry (GPa)	Modeled Kdry (GPa)	Impedance (kg/m²s)	Modeled Impedance (kg/m²s)	% Increase in Impedance	Initital RFC	Modeled RFC	% Decrease in RFC
Oil	9	9.04	6.94E+06	6.95E+06	0.18	-0.073	-0.072	1
Gas	10	10.04	6.79E+06	6.81E+06	0.25	-0.079	-0.078	1
							Average=	1

Table 6: Modeled effects of a 0.5% decrease in porosity on dry frame modulus (Kdry), impedance, and RFC. Decreasing porosity by 0.5% causes an average decrease in RFC magnitude of 1%.

previous section. Changing the velocity and density at each modeled well location causes a change in the reflection coefficient (RFC) at the top of the sand, which affects the amplitude response at that location. This change in amplitude response is modeled by creating synthetic seismic traces at each well location based on the modified velocity and density logs (See Appendix B).

1) Increasing water saturation

Gassmann fluid substitution modeling was used to modify the impedance logs at four well locations to reflect increasing water saturation due to water sweep. The four wells used are: 783-2ST1, 783-3, 783-4ST2, and 783-5BP (Fig. 2). Wells 783-2ST1 and 783-3 are initially oil-saturated and wells 783-4ST2 and 783-5BP are initially gas-saturated (Fig. 6). Modified impedance logs predict the impedance at each well location for a water saturation of 80% and an in-situ fluid saturation of 20%. Then, synthetic seismic traces are generated from each of the modified impedance logs.

Synthetic modeling of water sweep predicts a decrease in synthetic amplitude at all locations studied with the exception of well 783-2ST1. Modeling predicts a decrease in amplitude of 58% in wells that are oil-saturated (Fig. 17) and 23% in wells that are initially gas-saturated (Fig. 18). The decrease in synthetic amplitude observed in the gas wells is lower because the presence of gas significantly lowers acoustic impedance and results in a strong acoustic signature. The predicted drop in amplitudes would result in a seismic dimming seen in post-production seismic data.
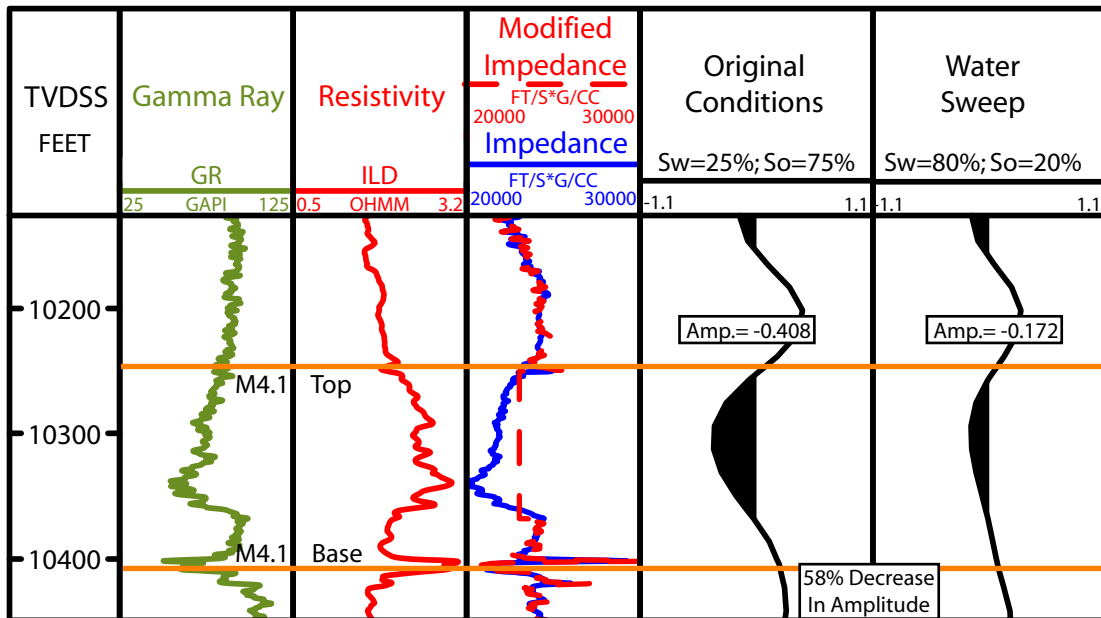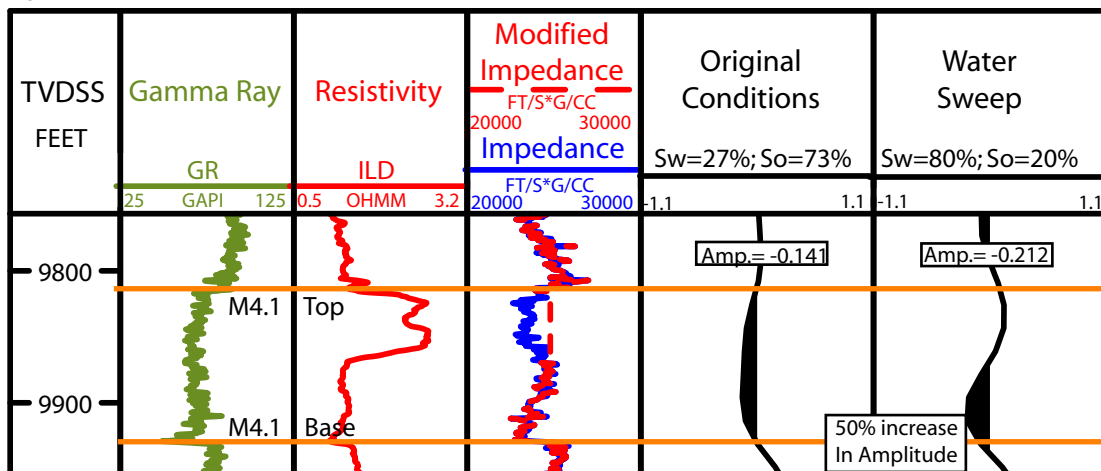
Figure 17: Comparison of synthetic seismograms before and after water sweep modeling for wells: A) 783-3 and B) 783-2ST1. Gamma-ray (GR), resistivity (ILD) and impedance logs are also shown. The blue impedance log represents original impedance while the red log represents the modeled impedance from fluid substitution. Modeling increasing water saturation in the two oil wells shows a 58% decrease in synthetic amplitude at 783-3 and a 50% increase at 783-2ST1. Wells are located in Figure 2.
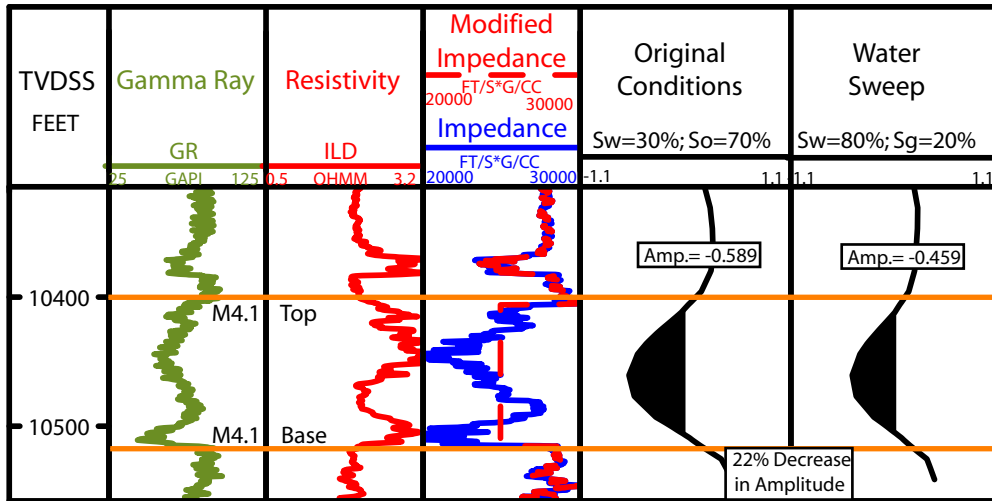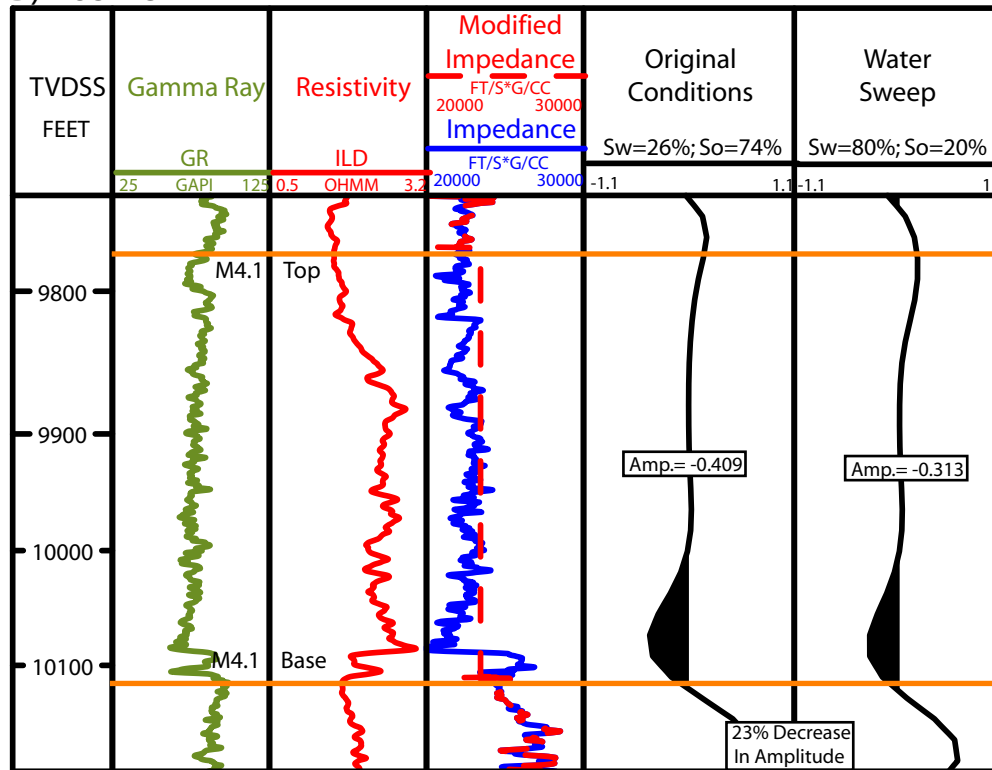
Figure 18: Comparison of synthetic seismograms before and after water sweep modeling for wells: A) 783-5BP and B) 783-4ST2. Gamma-ray (GR), resistivity (ILD) and impedance logs are also shown. The blue impedance log represents original impedance while the red log represents the modeled impedance from fluid substitution. Modeling increasing water saturation in the two gas wells shows a 22% decrease in synthetic amplitude at 783-5BP and a 23% decrease at 783-4ST2. Wells are located in Figure 2.

Gassmann modeling predicts a 31% decrease in RFC at well 783-2ST1, however, synthetic modeling of this decrease results in an increase in amplitude of 52% (Fig. 17B). At this location, the M4.1 shows the oil-water contact (OWC) at approximately 9,869 ft (TVDSS). The impedance log at this location was only modified in the oil-saturated region. The predicted velocity and density from Gassmann modeling were higher than the velocity and density of the water-saturated region of the sand. Therefore, there is an acoustic impedance contrast between the oil- and water-legs at this location and this contrast produces a stronger amplitude response than the original synthetic (Fig. 17B). This affect would be imaged as a brightening of amplitude in post-production seismic data.

2) Increasing oil saturation in a gas-oil system

The Gassmann fluid substitution model was used to modify the impedance logs at well 783-4ST2 to reflect increasing oil saturation due to oil sweep. Well 783-4ST2 in initially gas-saturated with S_g=74% (Fig. 6). We modified the 783-4ST2 logs to predict the impedance based on an oil saturation of 70%, with water and gas saturations of 20% and 10% respectively. Synthetic modeling predicts a 30% decrease in synthetic amplitude (Fig. 19). A decrease in amplitude resulting from oil sweep would be imaged as a dimming of amplitude in post-production seismic data.
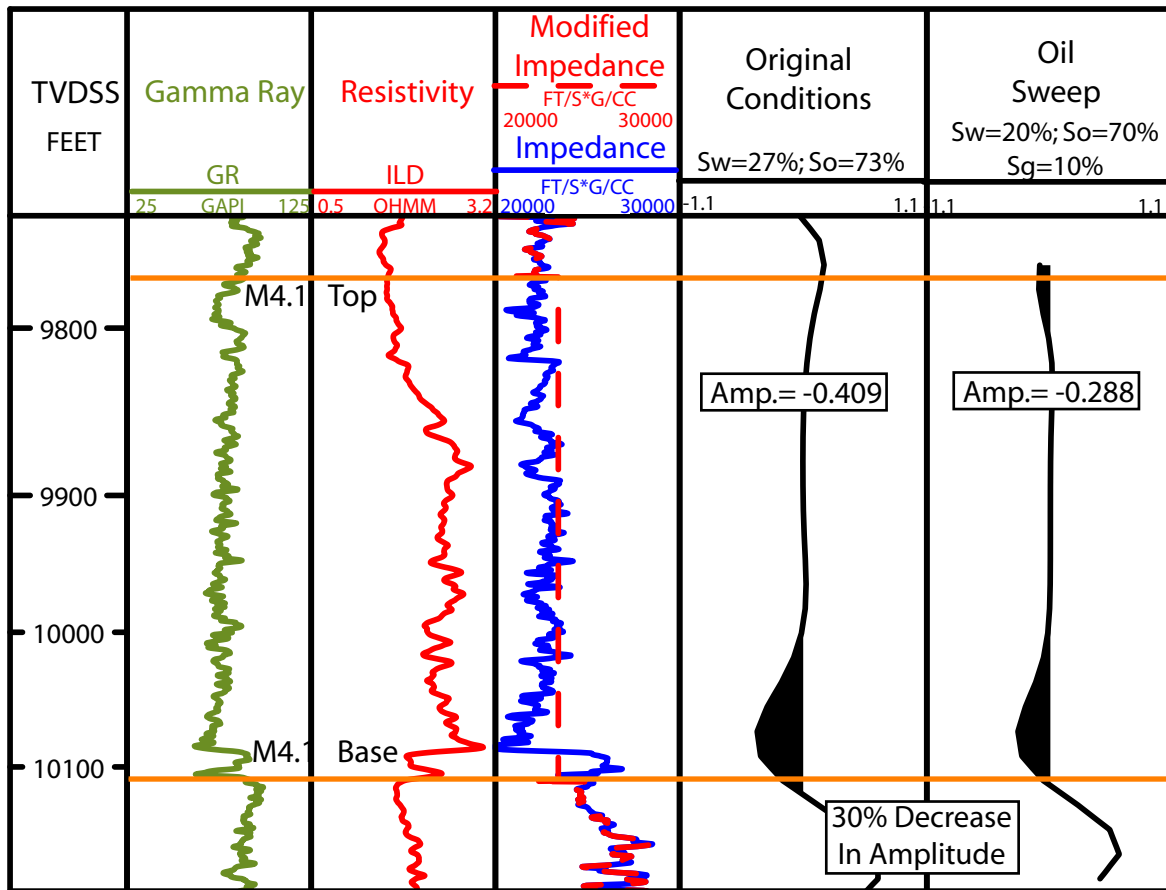
Figure 19: Comparison of synthetic seismograms before and after oil sweep modeling at the 783-4ST2 well. Gamma-ray (GR), resistivity (ILD) and impedance logs are also shown. The blue impedance log represents original impedance while the red log represents the modeled impedance from fluid substitution. Synthetic modeling shows that an increase in oil saturation to 70% will result in a 30% decrease in amplitude. Well is located in Figure 2.

3) Gas Exsolution

The Gassmann fluid substitution model was used to modify the impedance logs at two well locations to reflect increasing gas saturation (S_g) in the oil phase due to gas exsolution. The two wells used for gas exsolution modeling are: 783-2ST1 and 783-3. Wells 783-2ST1 and 783-3 are initially oil-saturated and located in the East Levee (Fig. 6). Modified impedance logs predict the impedance at each well location for gas saturations equal to 10%, 25%, and 50%. In each case water saturation was held constant at the initial value. Synthetic modeling of an increase in S_g from zero to 10% results in an average increase in synthetic amplitude of 56% (Fig. 20). Synthetic modeling predicts an average increase in synthetic amplitude of 37% for an increase in S_g from 10% to 50%, (Fig. 20). The predicted increase in amplitude would be imaged as a brightening in post-production seismic data. There is no oil penetration in the West Levee and therefore gas exsolution in this region was not modeled. However, it is assumed that increased gas saturation in this region will have a similar impact on amplitudes as predicted for the East Levee.

4) Increase in K_{dry}

The Gassmann fluid substitution model was used to modify the impedance logs at four well locations to reflect a 3% increase in dry bulk modulus (K_{dry}) due to an increase in effective pressure of 3MPa. The four wells used for modeling are: 783-1, 783-3, 783-4ST1 and 783-5BP. Wells 783-1, 783-4ST1, and 783-5BP are initially gas-saturated and well 783-3 is oil-saturated (Fig. 6). Synthetic modeling of this impedance change predicts an average decrease in synthetic amplitude of 4% for both an oil- and gas-
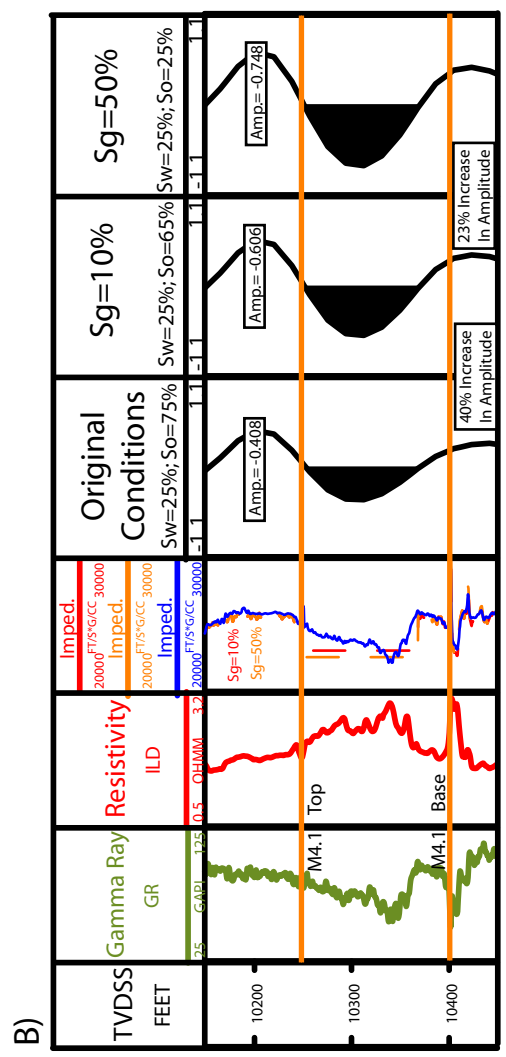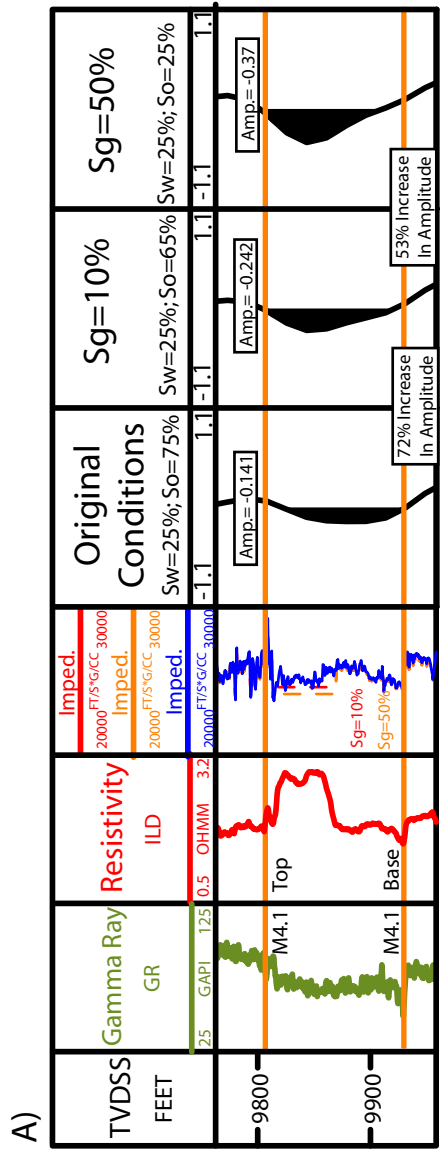
Figure 20: Comparison of synthetic seismograms before and after modeling free gas exsolution into the oil legs at well locations A) 783-2ST1 and B) 783-3. Gamma-ray (GR), resistivity (ILD) and impedance logs are also shown. The blue impedance log represents original impedance, the red log represents the modeled impedance for Sg=10%, and orange log represents the modeled impedance for Sg=50%. A) An initial increase in gas saturation of 10% results in a 72% increase in amplitude. As gas saturation increases beyond 10%, amplitude continues to increase at a lower rate. B) An initial increase in gas saturation of 10% results in a 40% increase in amplitude. As gas saturation increases beyond 10%, amplitude continues to increase at a lower rate. Wells are located in Figure 2.

saturated M4.1 (Table 7A). This effect would be imaged as amplitude dimming in post-production seismic data.

5) Decrease in Porosity

The Gassmann fluid substitution model was used to modify the impedance logs at five well locations to reflect a 0.5% decrease in porosity. The five wells used for modeling are: 783-1, 783-2, 783-3, 783-4ST2 and 783-5BP. Wells 783-1, 783-4ST2, and 783-5BP are initially saturated with gas (Fig. 6). Wells 783-2 and 783-3 are water- and oil-saturated, respectively (Fig. 6). Synthetic modeling of the impedance changes associated with a 0.5% decrease in porosity predicts an average decrease in synthetic amplitude of 3% (Table 7B). This decrease in synthetic amplitude would be imaged as amplitude dimming in post-production seismic data.

2.5 Conclusions

We use Gassmann fluid substitution to model the effects of changing fluid saturation, effective stress, and porosity on acoustic impedance. Synthetic seismograms were then generated to model the affect of these changes on synthetic amplitude. We show that increasing water saturation in both gas- and oil-water systems causes a significant decrease in amplitude. A decrease in amplitude would be images as a dimming in post-production seismic data. Modeling of increasing oil saturation in a gas-oil system also predicts a decrease in seismic amplitude. We model increasing gas saturation in an oil-water system due to gas exsolution. We show that a small increase in gas saturation, S_g=10%, has a significant impact on acoustic

A)

Well	Fluid	Initial Amplitude	Modeled Amplitude	% Drop In Amplitude
783-1	Gas	-0.789	-0.756	4
783-3	Oil	-0.408	-0.392	4
783-4ST1	Gas	-0.522	-0.496	5
783-5BP	Gas	-0.589	-0.566	4
			Average=	4

B)

Well	Fluid	Initial Amplitude	Modeled Amplitude	% Drop In Amplitude
783-1	Gas	-0.789	-0.774	2
783-2	Water	-0.629	-0.617	2
783-3	Oil	-0.408	-0.391	4
783-4ST2	Gas	-0.409	-0.399	2
783-5BP	Gas	-0.589	-0.573	3
			Average=	3

Table 7: Synthetic modeling results for A) Increase in Kdry of 3% and B) Decrease in 0.5% in porosity, both resulting from an increase in effective stress of 3MPa.

properties resulting in an average increase in amplitude of 56%. Increases in seismic

amplitude resulting from gas exsolution would be imaged as a seismic brightening in

post-production data. Changes in acoustic response due to reservoir compaction are

shown to be minor.

Chapter 3

Time-lapse Analysis

Abstract

Seven years of hydrocarbon production from the M4.1 reservoir resulted in acoustic changes that are resolved by reflection seismic data. We use two seismic surveys over the Tahoe field to study these changes. The first survey was acquired in 1993 and the second in 2001. We describe the correlation between the two seismic datasets over an area unaffected by production. The M4.1 sand shows increases in seismic amplitude associated with gas exsolution down-dip of three producing wells. Near the 783-5BP well, we observe a decrease in seismic amplitude which we attribute to increased oil saturation resulting from the up-dip movement of the oil leg. Based on a region of seismic brightening, which we attribute to gas exsolution, we interpret the presence of an oil rim in a region that was initially considered to contain only gas. We also adjust the location of a pre-production oil-water contact based on observed seismic differences.

53

3.1 Introduction

Time-lapse (4D) seismic analysis is the study of changes in the acoustic properties of a reservoir through time as a result of hydrocarbon production. These changes are observed by comparing two or more seismic surveys shot at different times over the same area. This type of analysis is possible because changes in fluid saturations and reservoir pressures can affect the seismic response of a reservoir (Lumley, 2001). For example, exsolution of free gas can occur during production due to pressure depletion and can significantly reduce the rock's acoustic impedance (Robinson, 2005). Specifically, in a 4D study of the South Timbalier Field, Burkhart (1997) predicts that 10% gas exsolution will increase synthetic amplitude by 30%. Conversely, increasing oil saturation, due to the up-dip movement of an oil rim into a gas cap, can cause seismic dimming (Weisenborn, 2005). A decline in reservoir pressure as production occurs increases the effective stress experienced by the reservoir (Waggoner, 2003). A 4D study over the Gullfaks oil field, northern North Sea, showed that an increase in effective pressure resulted in an increase in impedance of approximately 4% which affected seismic response (Najjar, 2003).

Time-lapse studies have the potential to increase the economic life of a field by identifying bypassed hydrocarbon reserves (Lumley, 2001). In 2005, a 4D study over the Gannet A field, central North Sea, revealed two pockets of unswept volumes of between 2.5 and 3.5 million barrels of recoverable oil (Weisenborn, 2005). Time-lapse analysis can also be used to find the optimal design of field development by mapping reservoir compartmentalization and fluid-flow properties of faults (Lumley, 2001). A 4D study

over the Meren Field, Nigeria, identified several compartments within the E-05 reservoir that may contain bypassed oil reserves (Lumley, 1999). In addition to identifying new hydrocarbon targets, the technology has also been used to identify regions where further development is no longer necessary. A 4D study over the Gullfaks oil field, northern North Sea, resulted in the removal of a potential drilling target from the plan based on time-lapse evaluations indicating that the target area had already been swept (Najjar, 2003).

We examine the differences in seismic response of the M4.1 reservoir after seven years of production using two seismic surveys over the Tahoe field. We then compare these differences to those modeled using Gassmann fluid substitution and synthetic seismic modeling in order to quantify and describe changes in the acoustic properties of the reservoir.

3.2 Data Description

3.2.1 Introduction

We use two seismic datasets over the Tahoe field to study changes in the seismic properties of the M4.1 reservoir as a result of production. The first survey was acquired in 1993, one year before production began in 1994. These data were shot in a northeast-southwest direction. They have a fold of 60 and bin size of 82x82ft. This survey was conducted with a streamer length of 6,000 m, a CDP line spacing of 50 m, and a shotpoint interval of 50 m. The second survey was conducted in 2001 after seven years of production. This survey was shot with the same northeast-southwest orientation as the 1993 data. It has a fold and bin size of 72 and 82x82ft respectively. The 2001 survey

was conducted with a streamer length of 7,200 m, a CDP line space of 25 m, and a shotpoint interval of 25 m.

The 2001 seismic data were processed for normalization to the 1993 data. Normalization of the datasets allows observed seismic differences between surveys to be attributed to production affects rather than noise. We received the data after normalization.

3.2.2 Estimating S/N ratio

We consider a region assumed to be unaffected by production in order to estimate the S/N ratio of our data (Fig. 21). We extract the seismic amplitude data, obtained by mapping the M4.1 event in both seismic datasets, from this region in both the 1993 and 2001 datasets for comparison. We use a method described by Burkart (2000) to quantify the S/N ratio.

First, we rescale the 1993 data (y_i) using the following relationship:

$$\hat{y_i} = \left(\frac{\sigma_x}{\sigma_y} \right)(y_i - b_0),$$
<div align="right">Equation 9</div>

where σ_x and σ_y are the standard deviations of the 2001 and 1993 seismic data respectively, $\hat{y}$ represents the regression-normalized 1993 seismic data, and b_0 is the maximum likelihood estimate ($b_0 = \bar{y} - b_1 \bar{x}$) (Burkhart, 2000). Equation 9 normalizes the 1993 dataset so that it has the same mean and variance as the 2001 dataset. We then plot the normalized 1993 amplitude data with the 2001 data (Fig. 22). The crossplot of 1993
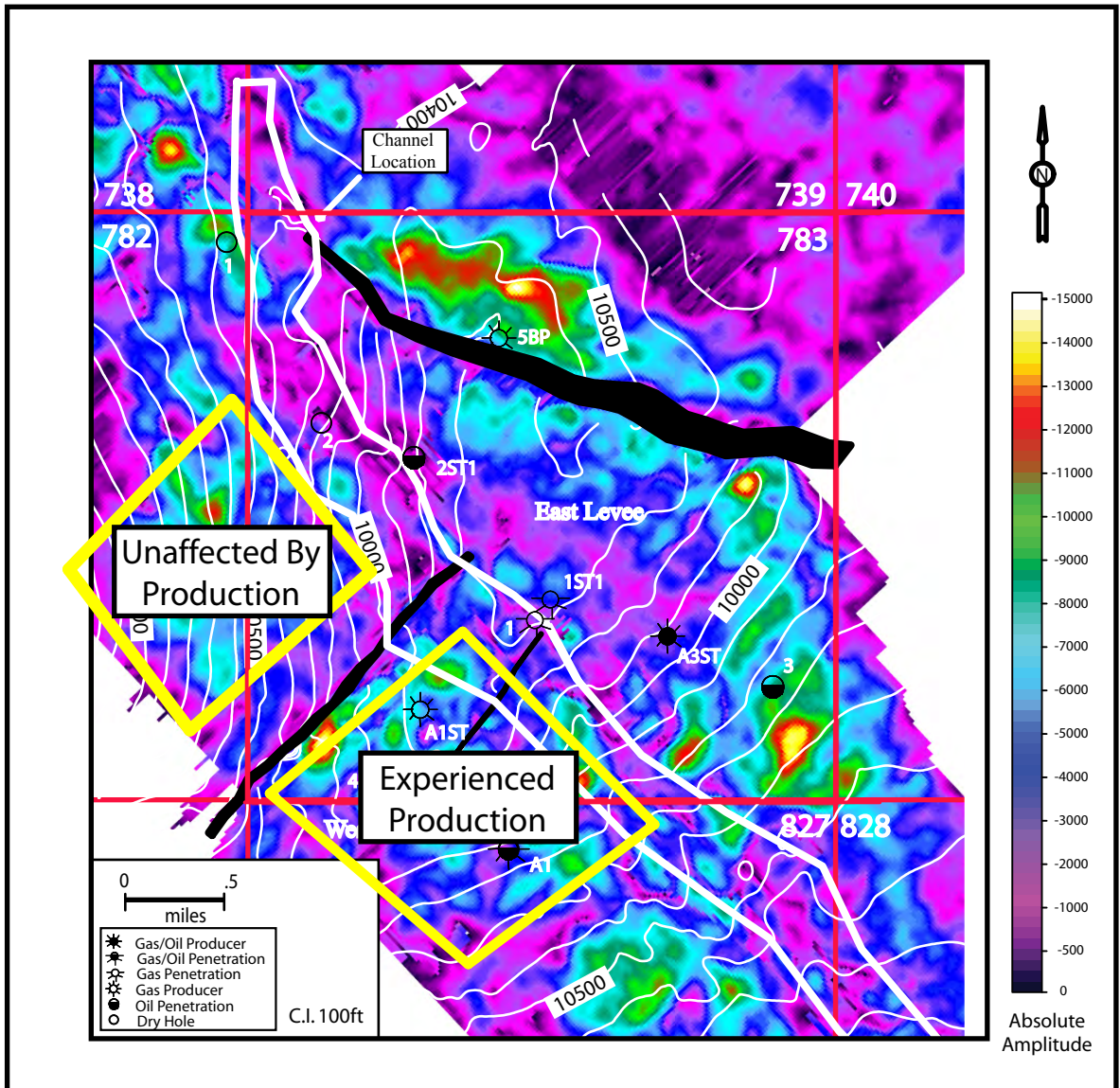
Figure 21: 1993 amplitude extraction of the M4.1, overlain on a structure map of the top of the M4.1. Large negative amplitudes generally indicate hydrocarbon-bearing regions. Smaller negative amplitudes represent either zones where water fills the pores or where the sand has thinned. A trend of low amplitudes is outlined in white and is interpreted to indicate the channel location. Yellow outlines delineate the areal extent of the seismic volumes used in the S/N ratio analysis (Figs. 22 & 23).
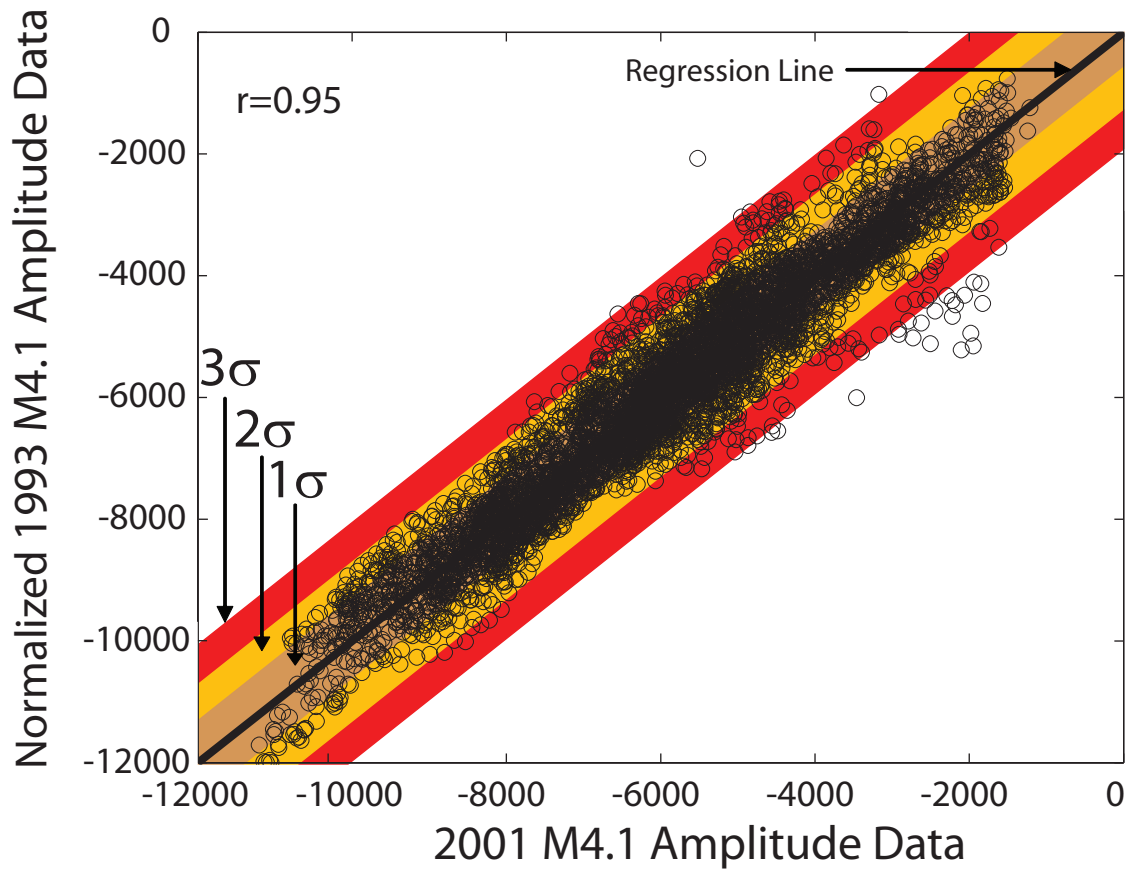
Figure 22: Amplitude crossplot of the normalized 1993 data versus the 2001 data over an area unaffected by production (Located in Fig. 21). The scatter around the regression line represents the noise in the two surveys. We use the standard deviation (σ) of these differences to define confidence intervals (colored bands) as a function of increasing σ. The σ bands are drawn by defining a line on both sides of the regression line that falls at a given σ distance from the regression line. These lines serve as the boundaries for that particular σ interval, which is then colored.

versus 2001 seismic data shows some scatter (Fig. 22). This scatter represents the noise present in the two surveys. The correlation coefficient (r) is:

$$r = \frac{\sigma_{x\hat{y}}}{\sigma_x \sigma_{\hat{y}}},$$

Equation 10

where $\sigma_{x\hat{y}}$ is the covariance between the two seismic surveys. When the data correlate perfectly, r = 1, and all points lie on a straight line in the amplitude crossplot. The correlation coefficient is found to be r=0.95 (Table 8A). Burkhart (2000) defines the variance in the error values of either seismic data (σ_μ^2) with the following relationship:

$$\sigma_\mu^2 = (1 - r)\sigma_x^2,$$

Equation 11

where σ_x^2 is the variance in the 2001 seismic data. The S/N in each dataset is defined by Burkhart (2000):

$$S/N = \sqrt{\sigma_x^2 - \sigma_\mu^2} \Big/ \sigma_\mu.$$

Equation 12

As described in Burkhart (2000), it is assumed that the signal to noise ratio is the same in both datasets. We compute a S/N ratio of 4.23 which is very high compared to the S/N ratios found in previous studies of the Bullwinkle and South Timbalier fields, Gulf of Mexico (Comisky, 2002; Burkhart, 1997), which employed a similar method for calculating S/N (Table 8B).

Parameter	Definition	Value
σ_x	standard deviation of x	2033
σ_μ	variance of μ	468
$\sigma_{\hat{y}}$	standard deviation of $\hat{y}$	2033
$\sigma_{x\hat{y}}$	covariance of x and $\hat{y}$	3,913,700
S/N ratio	$\sqrt{\sigma_x^2 - \sigma_\mu^2} \Big/ \sigma_\mu$	4.23

Table 8A: Signal and noise components used in calculation of correlation coefficient (r) and S/N ratio.

Field	Compared Surveys	S/N
Bullwinkle	1988 E-W HF/1997 E-W HF	1.56
Bullwinkle	1988 N-S HF/1997 N-S HF	1.8
Bullwinkle	1988 N-S LF/1997 N-S LF	1.9
South Timbalier	1988/1994	2.35
Tahoe	1993/2001	4.23

Table 8B: Comparison of S/N ratios computed in previous studies using the same methodology.

3.2.3 Discriminating signal from noise

The amplitude crossplot of the normalized 1993 and 2001 seismic data, over a region not affected by production (Fig. 22), represents the differences between the two datasets resulting from noise. We subtract the 2001 amplitude data from the 1993 amplitude data and use the standard deviation (σ) of these differences to define confidence intervals as a function of increasing σ (Fig. 22). We then compare the 1993 data with the 2001 data over a region that has experienced production (Fig. 23). These data show more scatter than the amplitude crossplot over a region unaffected by production. This is quantified with a lower correlation coefficient (r = 0.88 versus r = 0.95) (Fig. 23). The increased scatter in the produced region reflects differences due to both noise and changes in acoustic properties of the reservoir. We use the defined confidence intervals from the region not affected by production to distinguish between amplitude differences resulting from noise and those from changing acoustic properties in the produced zone (Fig. 23). Amplitude differences that plot at larger intervals of σ are more likely attributable to changes in rock and fluid properties.

3.3 Observations

The M4.1 was mapped throughout the 2001 seismic data and we present an amplitude map of the reservoir after seven years of production (Fig. 24). This amplitude map was created by mapping the peak negative trough that represents the M4.1 sand in the 2001 data. We then subtract the 2001 amplitude map (Fig. 24) from the 1993 amplitude map (Fig. 5) to produce an M4.1 difference map (Fig.25). This map represents the amplitude difference between the 1993 and 2001 data throughout the M4.1 reservoir.
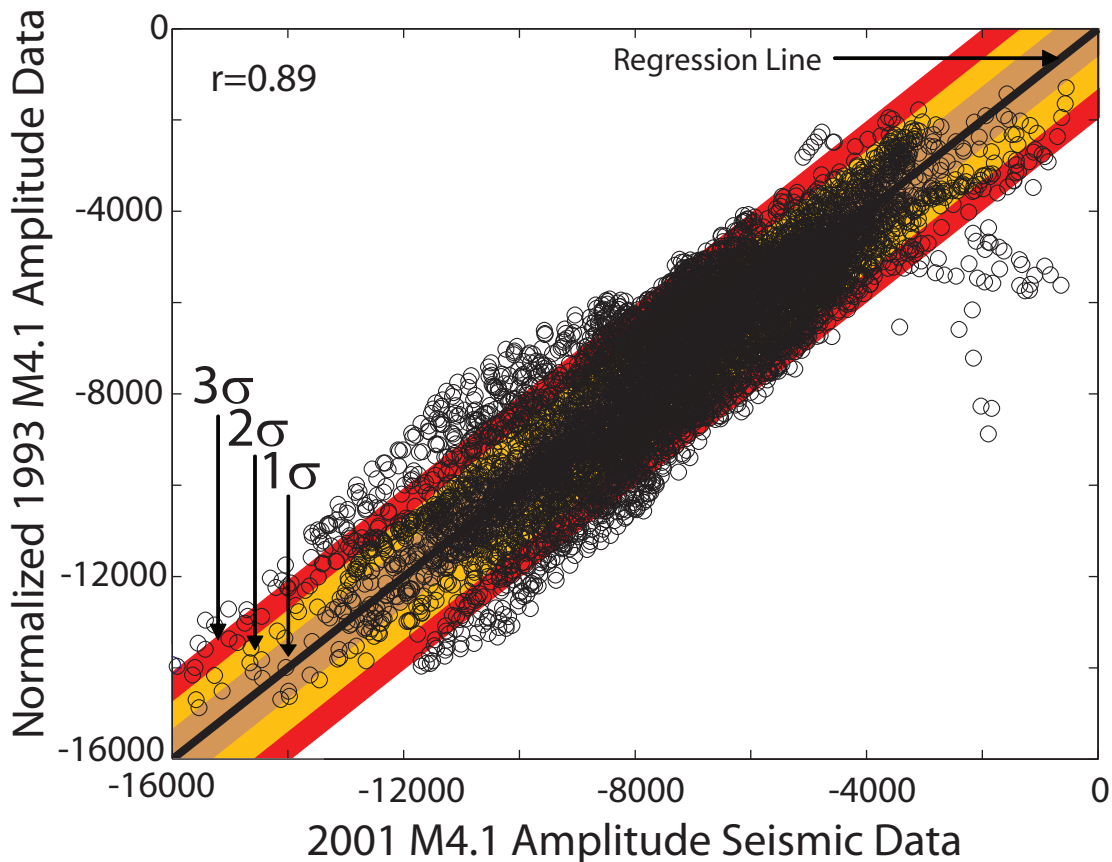
Figure 23: Amplitude crossplot of the normalized 1993 data versus the 2001 data over a produced area. These data show more scatter than the amplitude crossplot over a region unaffected by production (Fig. 22). This is quantified with a lower correlation coefficient (r = 0.88 versus r = 0.95). The lower correlation coefficient is recording both noise and changes in acoustic properties of the reservoir. We use the defined confidence intervals from the region not affected by production (Fig. 22) to distinguish amplitude differences resulting from either noise or changing acoustic properties in the produced zone. Points father from the regression line have a higher probability of being attributable to changes in the acoustic properties of the reservoir. These data are extracted from the region delineated in Figure 21.
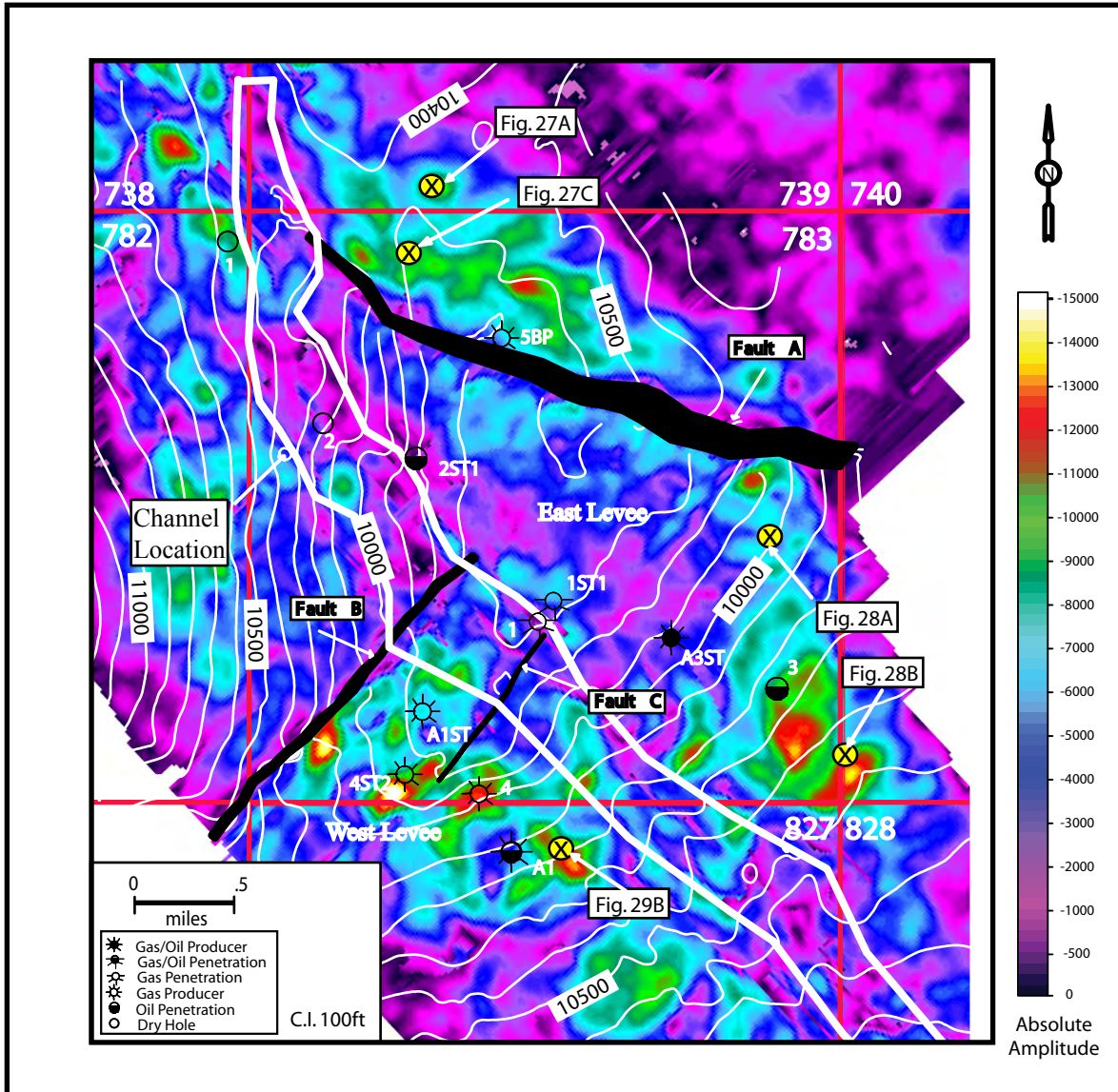
Figure 24: 2001 seismic data amplitude extraction of the M4.1, overlain on a structure map of the top of the M4.1. High amplitudes generally indicate hydrocarbon bearing regions. Lower amplitudes represent either zones where water fills the pores or where the reservoir sand has thinned. A trend of low amplitudes is outlined in white. It is interpreted to indicate the channel location. Locations of seismic trace extractions in Figures 27-29 are also labeled.

Figure 25: M4.1 absolute amplitude difference map made by subtracting the 2001 amplitude map (Fig. 24) from the 1993 amplitude map (Fig. 5). Values that were originally negative and become less negative with time record seismic dimming and are shown as cool colors (blue, purple). In contrast, values that were originally negative and become more negative with time record seismic brightening and are shown as warm colors (red, orange). Locations of seismic trace extractions in Figures 27-29 are also labeled.

We then apply the confidence intervals defined in the previous section to distinguish between seismic differences that are due to noise and those that can be attributed to changes in the acoustic properties of the reservoir (Fig. 26). We color all data that falls within one standard deviation (σ) of the mean brown; in this region production effects cannot be distinguished from noise present between the two datasets. The remaining data are plotted according to incremental values of σ (Fig. 26). Values that were originally negative and become less negative with time are interpreted to represent areas of seismic dimming and are shown as cool colors (blue, purple) (Fig. 26). In contrast, values that were originally negative and become more negative with time are interpreted to represent areas of seismic brightening and are shown as warm colors (red, orange) (Fig. 26).

We use the M4.1 difference map (Fig. 26) to quantify and describe observed seismic changes in the reservoir after seven years of production. We define four regions of interest on the M4.1 difference map: R1, R2, R3, and R4 (Fig.26). R1 is to the north of Fault A in the East Levee and surrounds the #5 wells (Fig. 26). R2 and R3 are both south of Fault A in the East Levee (Fig. 26). R4 is located in the West Levee to the south of Fault B (Fig. 26).

Region R1 shows both increases and decreases in seismic amplitude (Fig. 26). We observe a decrease in seismic amplitude in the area immediately surrounding the producing well, extending approximately 100ft down-dip (Fig. 26). Further down-dip, we observe an increase in seismic amplitude (Fig. 26). The M4.1 in region R2, just south of Fault A, shows a decrease in seismic amplitude (Fig. 26). In region R3, located further
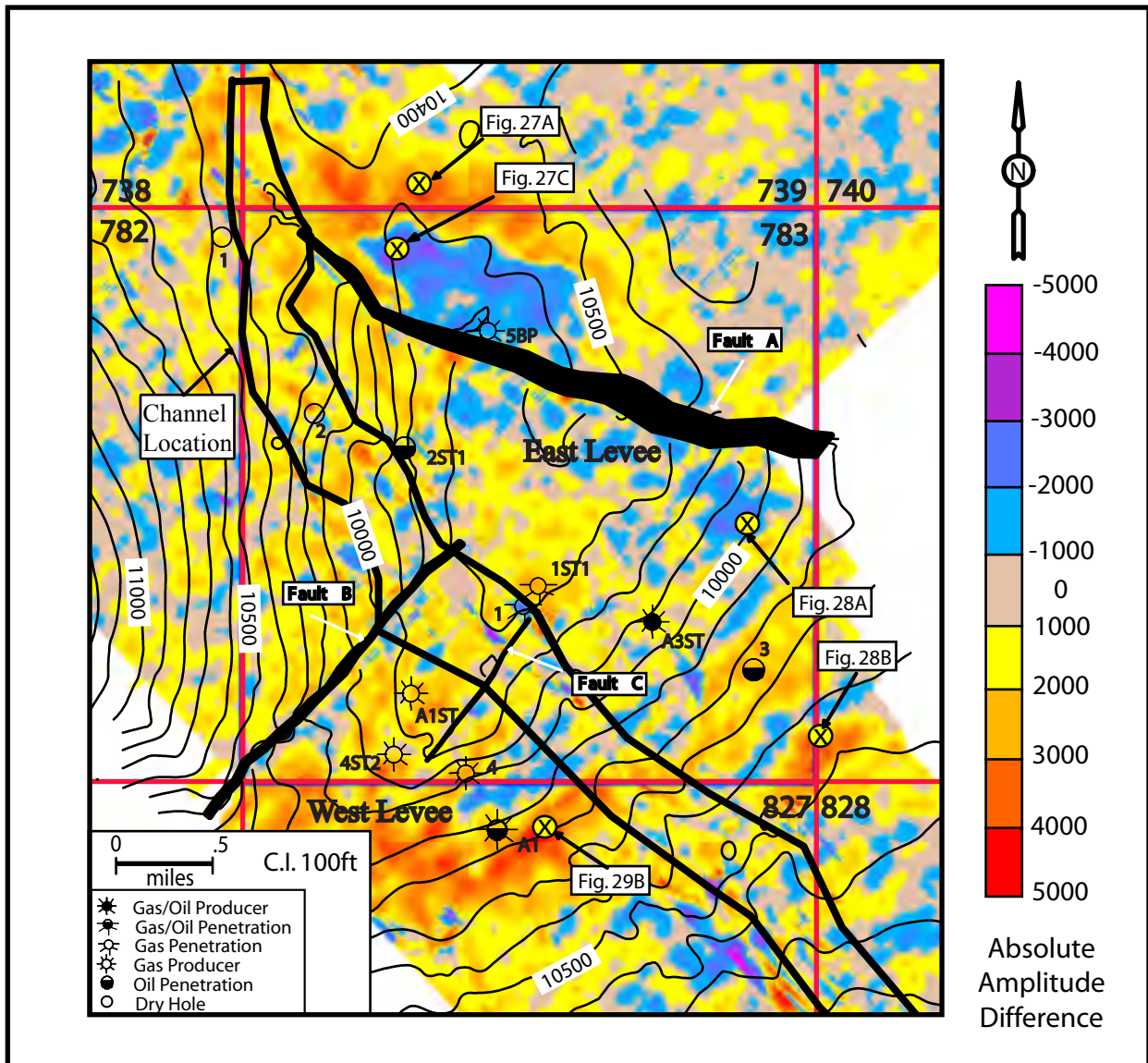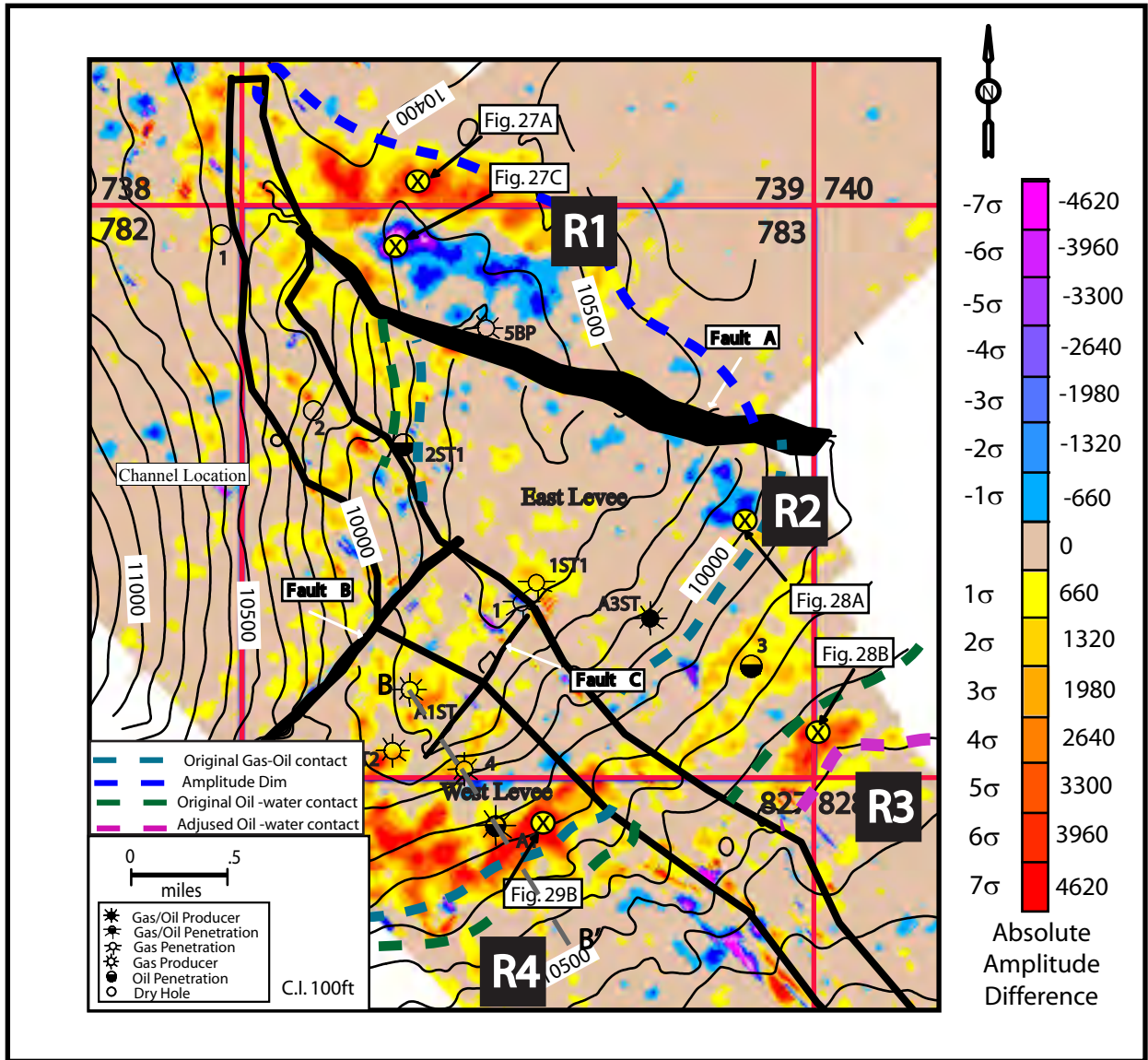
Figure 26: M4.1 absolute amplitude difference map made by subtracting the 2001 amplitude map (Fig. 24) from the 1993 amplitude map (Fig. 5). We color all data brown that fall within one standard deviation (σ) of the mean. We plot the remaining data according to incremental values of σ as defined in Figure 22. The original fluid contacts delineated in the fluid distribution map (Figure 6) are shown. The location of cross-section BB' in Figure 30 is also shown.

south in the East Levee, we observe an increase in seismic amplitude (Fig. 26). Region R4, located in the West Levee, shows a strong increase in seismic amplitude (Fig. 26).

3.4 Discussion

We compare observed differences in seismic amplitude after seven years of production to predicted changes from Gassmann and synthetic modeling. The M4.1 in region R1 was initially characterized as only gas bearing. We interpret the observed increase in seismic amplitude, down dip of the producing well, to suggest the presence of an oil rim that experienced gas exsolution as reservoir pressure declined (Fig. 26). In this region, seismic amplitudes increase by as much as 50% (Fig. 27A). This increase is consistent with synthetic modeling of an increase in gas saturation to 10%, which predicts an increase in seismic amplitude of 40%-72% (Fig. 20).

There is an area where amplitudes decrease at well 783-5BP and extends down-dip approximately 100ft (Fig. 26). Seismic amplitude decreases by 15% at well 783-5BP (Fig. 27B) and 35% down-dip of well 783-5BP (Fig. 27C). A 35% decrease in amplitude is consistent with synthetic modeling of the up-dip movement of an oil rim into a gas cap, which predicts a 30% decrease in amplitude for an increase in oil saturation to 70% (Fig. 19).

Increasing oil saturation in the gas cap, caused by the up-dip movement of the oil rim, is also interpreted to cause the seismic dimming observed in region R2 (Fig. 26). In this region we observe decreases in amplitude by as much as 27% (Fig. 28A). The observed amplitude drop is consistent with synthetic modeling of oil sweep which predicts a 30% decrease in amplitude as oil saturation approaches 70% (Fig. 19).
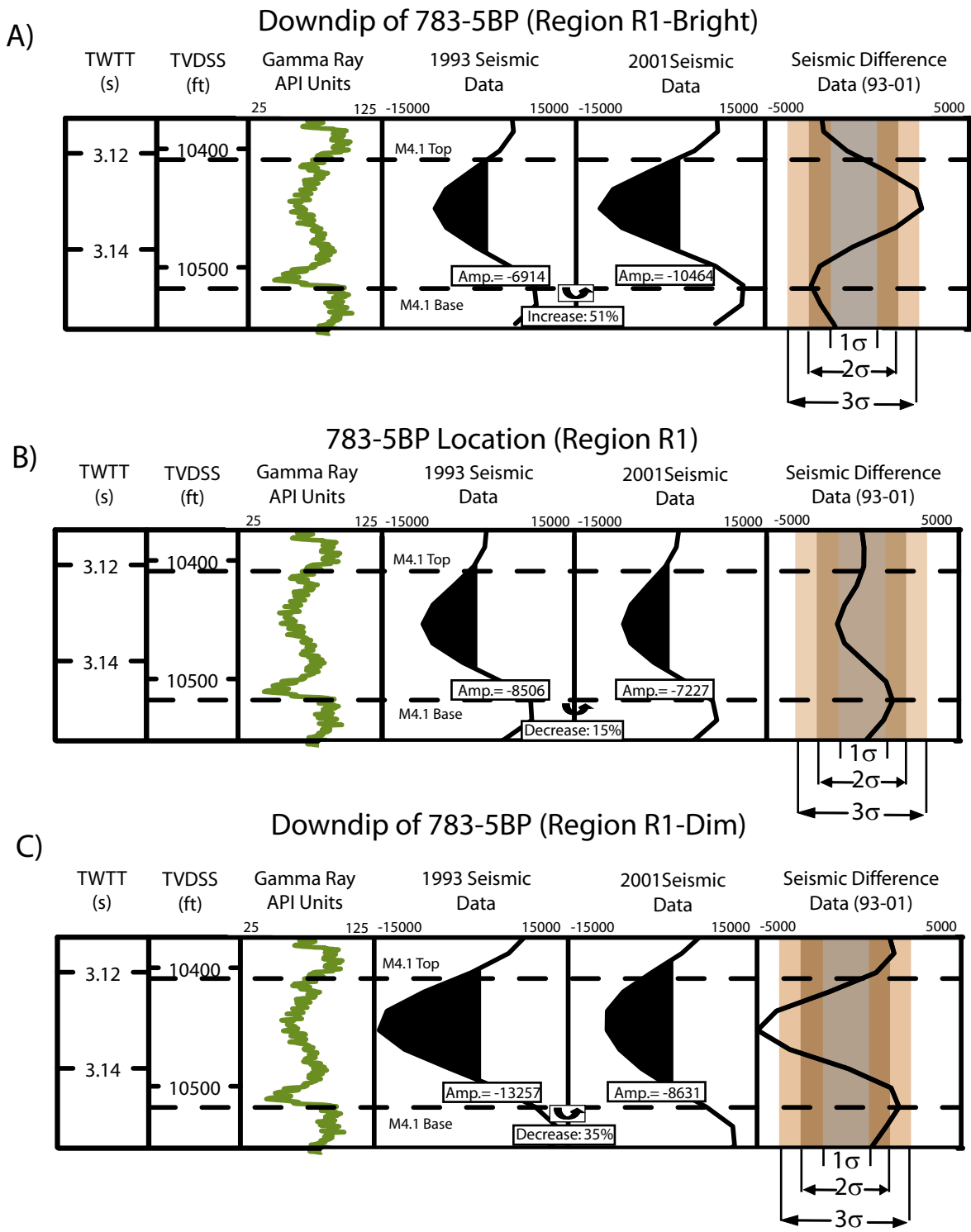
Figure 27: Gamma-ray log, seismic traces and seismic difference traces extracted from region R1 located in Figure 26: A) down-dip of well 783-5BP in region of seismic brightening, B) at well 783-5BP, and C) down-dip of well 783-5BP in region of seismic dimming. The colored bands in the seismic difference traces represent the 1, 2, and 3 sigma intervals defined in Figure 22. The locations of the well penetration and trace extractions are shown in: Figure 5 (1993 seismic), Figure 24 (2001 seismic), and Figure 26 (difference map). Trace extractions are denoted by a yellow circle with an "x".

A) East Levee Dim (Region R2)

B) East Levee Bright (Region R3)

Figure 28: Seismic traces and seismic difference traces extracted from A) region of seismic dimming at R2 and B) region of seismic brightening at R3. Regions R2 and R3 are located in Figure 26. The colored bands in the seismic difference traces represent the 1, 2, and 3 sigma intervals defined in Figure 22. The locations of the well penetration and trace extractions are shown in: Figure 5 (1993 seismic), Figure 24 (2001 seismic), and Figure 26 (difference map). Trace extractions are denoted by a yellow circle with an "x".

In region R3, located in the southern portion of the East Levee, seismic amplitude increases 40% (Fig. 28B). This bright event is well defined and is located between depths ranging from 10,400ft to 10,500ft (Fig. 26). The 40% increase is consistent with synthetic modeling of gas exsolution which predicts an increase in synthetic amplitude of 40-72% based on an increase in S_g up to 10% (Fig. 20). Our original fluid distribution analysis placed the oil-water contact (OWC) at approximately 10,400ft in this region (Fig. 26). Based on the seismic brightening observed, we interpret the presence of oil down to a depth of 10,500ft and adjust the pre-production OWC to this depth (Fig. 26).

There is seismic brightening in region R4, located in the West Levee (Fig. 26). Seismic amplitudes increase by 45% at well 827-A1 and 60% approximately 50ft down-dip (Figs. 29A & 29B). This increase in amplitude is consistent with synthetic modeling of gas exsolution, which predicts an increase in synthetic amplitude of 40%-72% based on an increase in S_g to 10% (Fig. 20).

The seismic brightening is observed throughout much of the West Levee within a depth interval of 10,050ft to 10,350ft (Fig. 26). The original gas-oil contact (GOC) in the West Levee was placed at 10,250ft and the oil-water contact (OWC) at 10,315 (Fig. 26). While the observed brightening conforms well to the original OWC, time-lapse analysis shows seismic brightening at depths shallower than the original GOC. We show, through a structural cross-section, that a "fringe" zone in the West Levee M4.1 sand contains both gas and oil (Fig. 30). The M4.1 sand up-dip of this zone contains only gas while the sand down-dip contains only oil (Fig. 30). We plot the lateral extent of this fringe zone on the
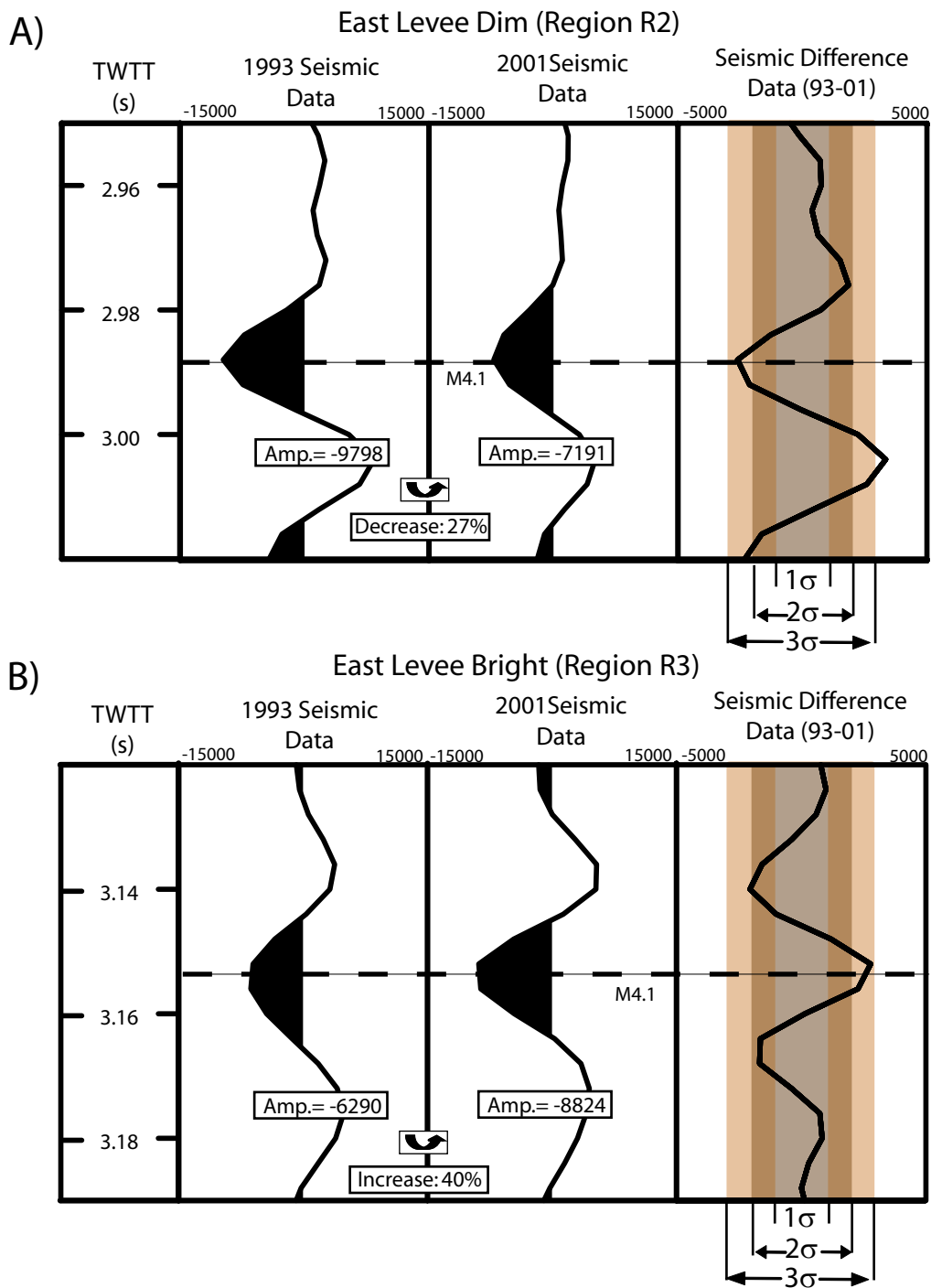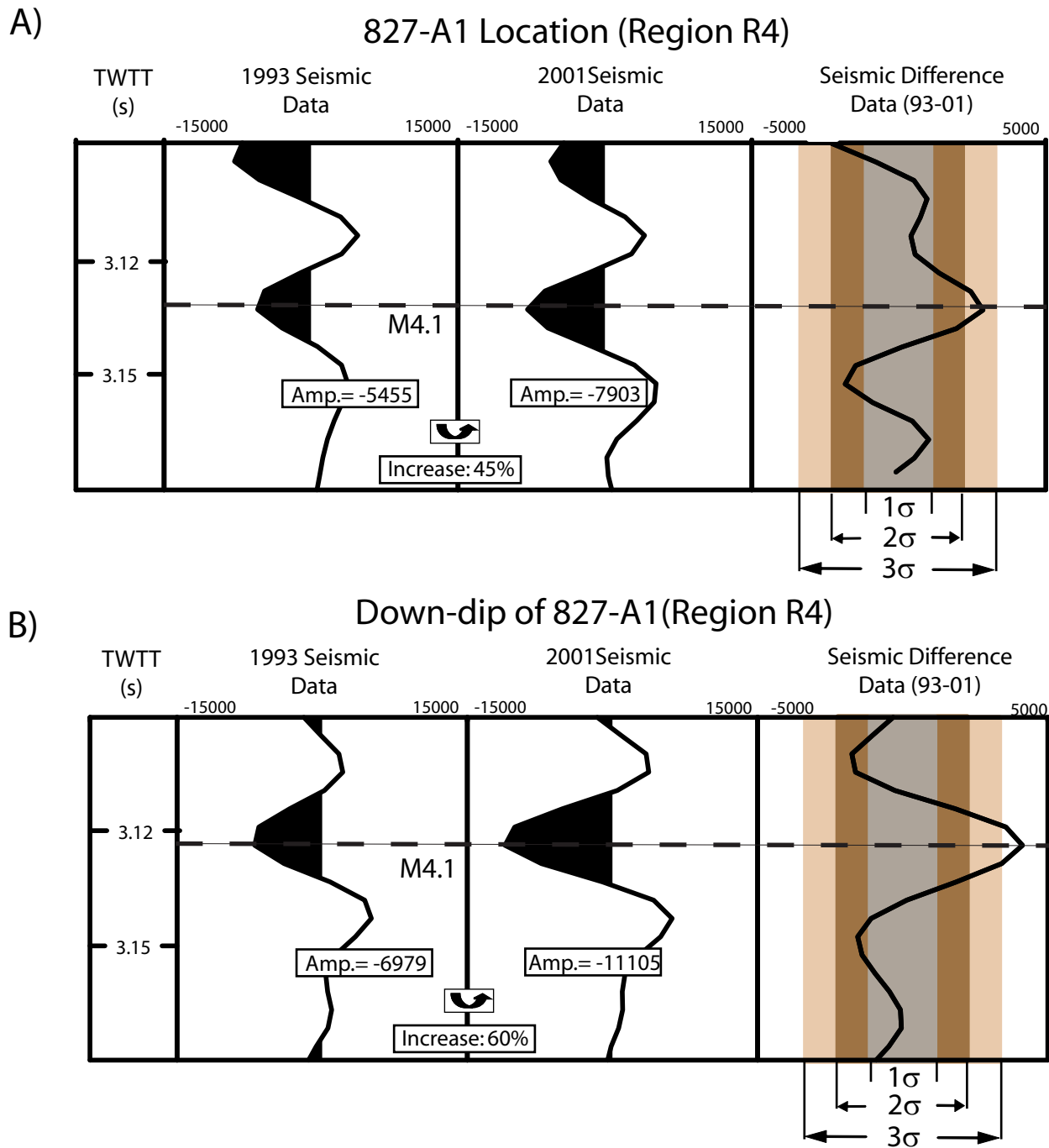
Figure 29: Seismic traces and seismic difference traces extracted from region R4 located in Figure 26: A) at well 827-A1 and B) down-dip of well 827-A1 in region of seismic brightening. The colored bands in the seismic difference traces represent the 1, 2, and 3 sigma intervals defined in Figure 22. The locations of the well penetration and trace extractions are shown in: Figure 5 (1993 seismic), Figure 24 (2001 seismic), and Figure 26 (difference map). Trace extractions are denoted by a yellow circle with an "x".
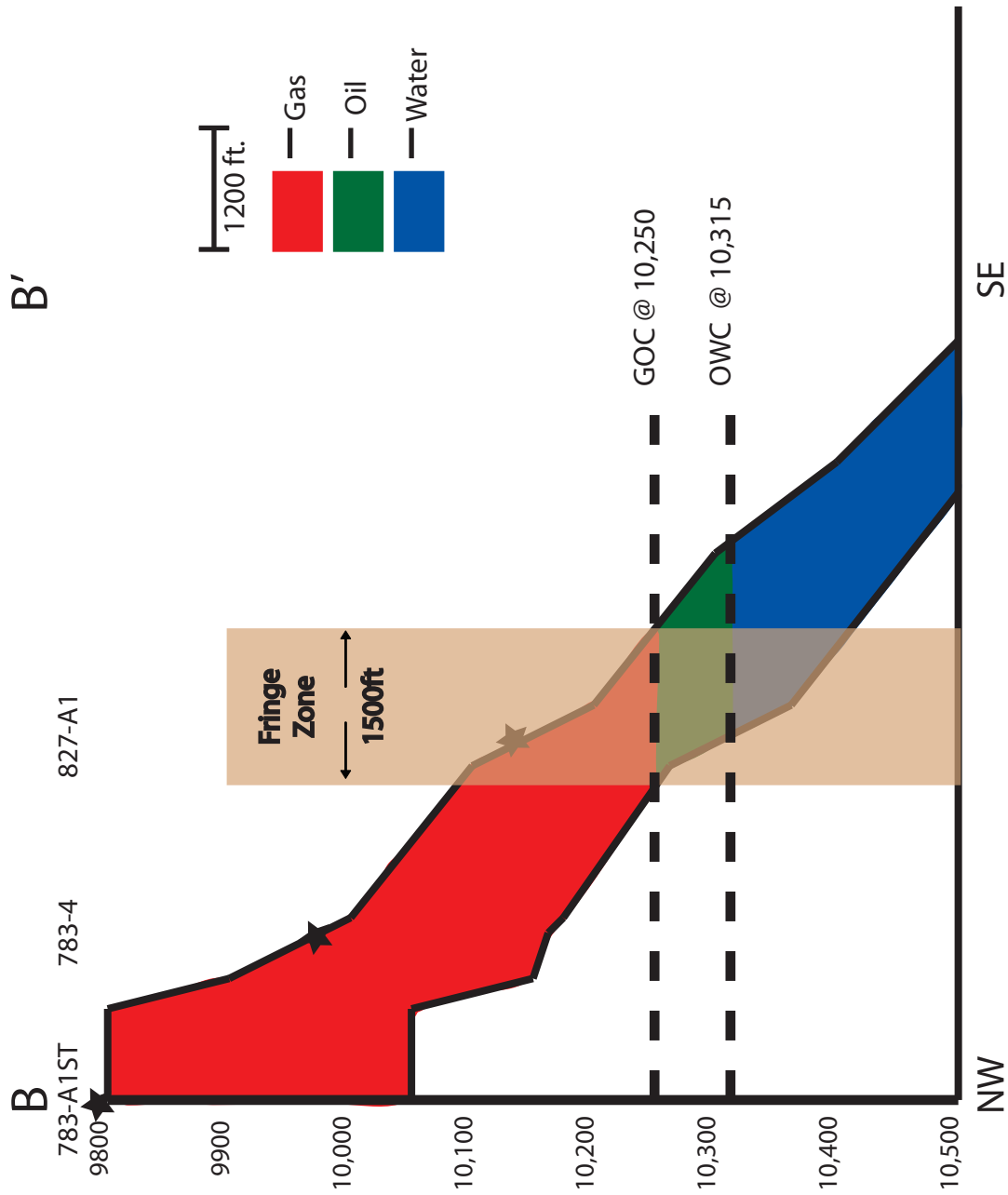
Figure 30: Cross-section showing the structure and fluid distribution along BB' in the West Levee. The stars indicate the location of the wells labeled above. The fringe zone is a region where the M4.1 contains both gas and oil. Everything to the left (up-dip) of the fringe zone contains only gas while everything to the right (down-dip) contains only oil. We plot the lateral exten of this zone on the M4.1 difference map in Figure 31. The location of BB' is located in Figure 26.

M4.1 difference map and show that the region of seismic strengthening in the West Levee is contained within this fringe zone (Fig. 31). We use fluid substitution to model gas exsolution in the oil-leg at three locations within this zone, with oil-leg thickness increasing down-dip (Fig. 32). As the amount of oil in the sand increases, the amount of gas that can exsolve also increases. Modeling of this gas exsolution predicts seismic strengthening consistent with the observed differences in the M4.1 difference map (Fig. 33). Therefore, we attribute the seismic strengthening up-dip of the GOC to gas exsolution in the oil leg of the M4.1.

3.5 Conclusions

Time-lapse analysis of the M4.1 reservoir shows changes in seismic properties after seven years of production. We observe seismic brightening in both the East and West Levees, which we attribute to the exsolution of free gas in the oil phase (Fig. 34). Seismic amplitudes increase by as much as 60% in some regions. We interpret the observed increase in seismic amplitude, down-dip of well 783-5BP, to suggest the presence of an oil rim in a region previously thought to contain only gas (Fig. 26). Based on seismic brightening observed to the south in the East Levee, we interpret the presence of oil down to a depth of 10,500ft and place the pre-production OWC at this depth, 90ft. deeper than previously interpreted (Fig. 26). We also observe seismic dimming in the East Levee which, we attribute to an increase in oil saturation due to the up-dip movement of the oil rim (Fig. 35).
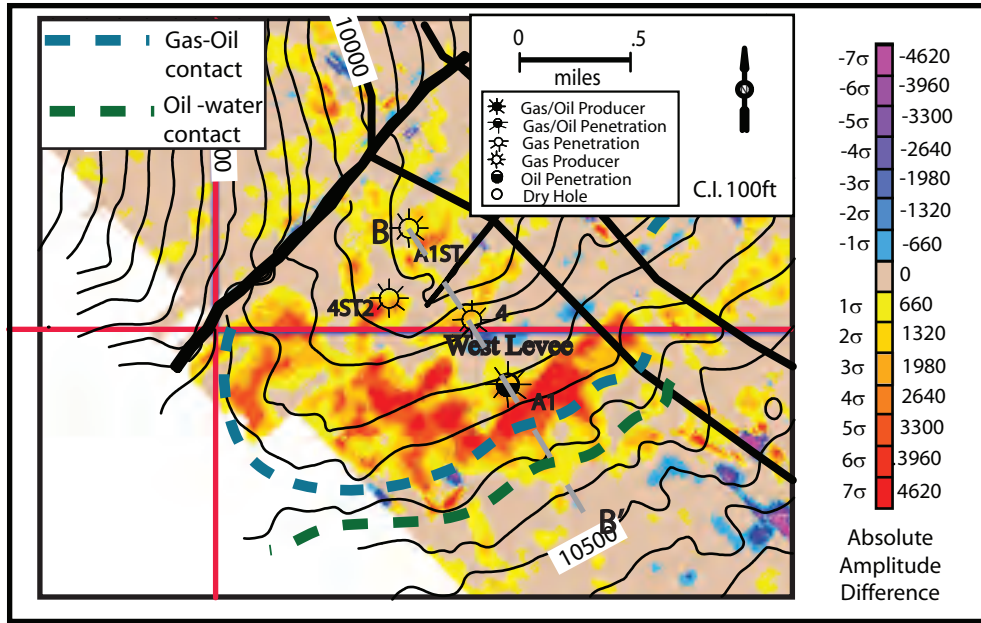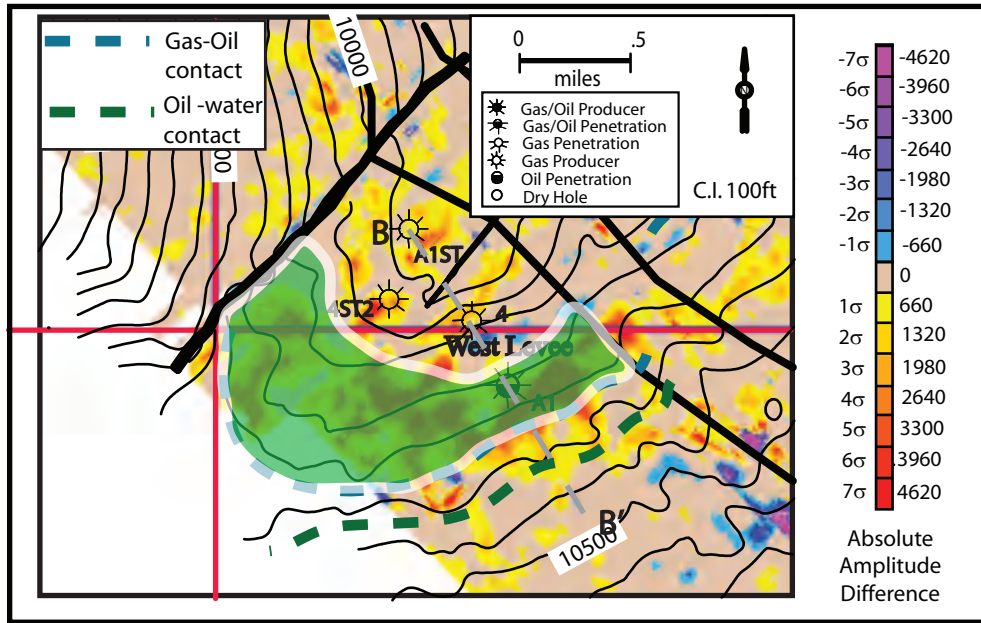
Figure 31: A) M4.1 absolute amplitude difference map centered on the West Levee. B) The fringe zone defined is colored green and represents a region where the M4.1 contains both gas and oil. The fringe zone is thicker to the west because the M4.1 is thicker in this region. We color all data that falls within one standard deviation (σ) of the mean brown and plot the remaining data according to incremental values of σ as defined in Figure 22. Values that were originally negative and become less negative with time are interpreted to represent areas of seismic dimming and are shown as cool colors (blue, purple). In contrast, values that were originally negative and become more negative with time are interpreted to represent areas of seismic brightening and are shown as warm colors (red, orange). The original fluid contacts delineated in the fluid distribution map (Figure 6) are shown. The location of cross-section BB' in Figure 30 is also shown.
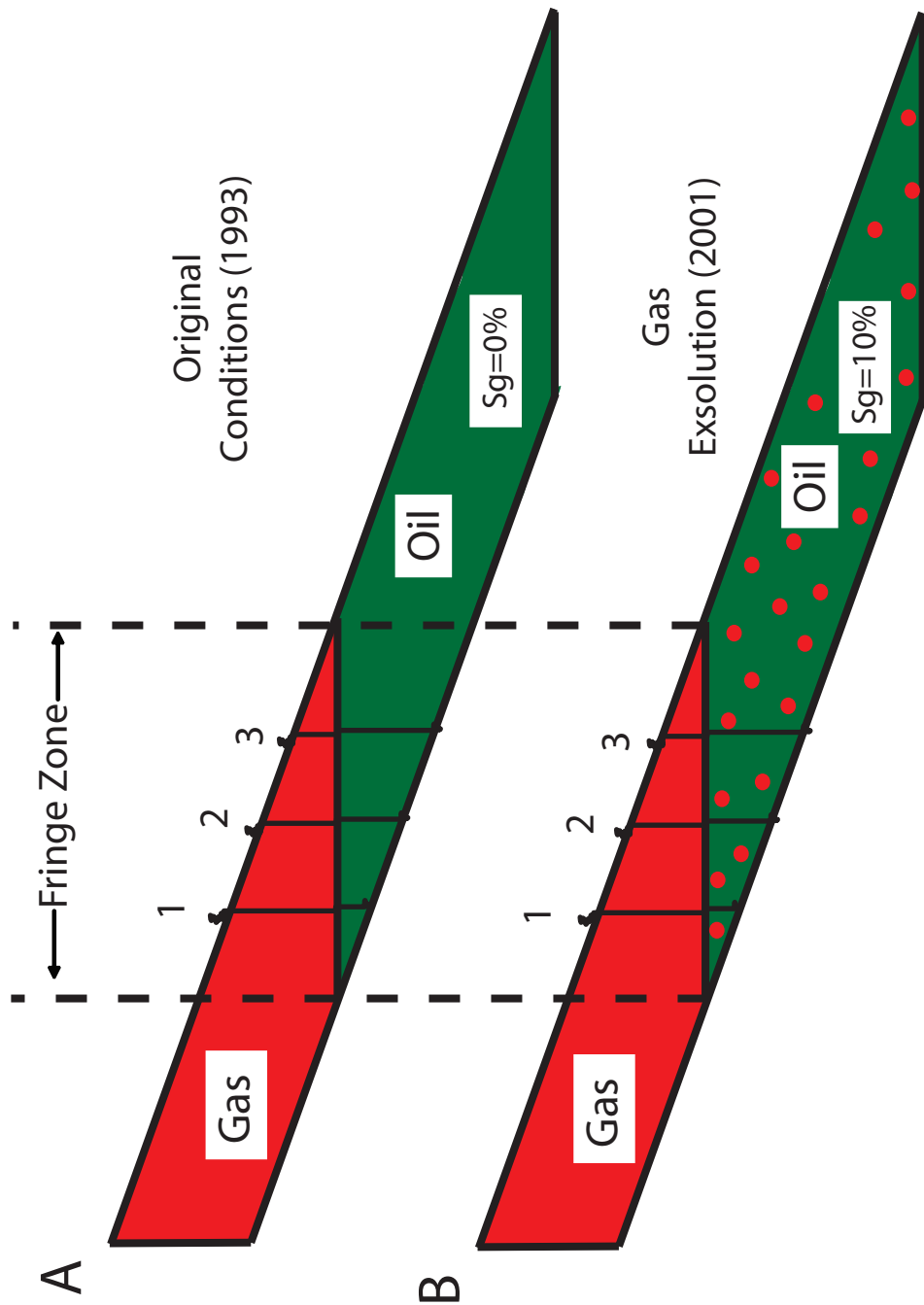
Figure 32: Gassmann fluid substitution model of the "fringe" zone where the M4.1 contains both gas and oil. We model the acoustic response of this zone under A) intial conditions (Sg=0%) in the oil-leg and B) gas exsolution (Sg=10%) in the oil-leg. In each scenario we model the acoustic response at three locations: 1) 75ft oil-leg, 2) 150ft oil-leg, and 3) 225ft oil-leg. The acoustic models are shown in Figure 33.
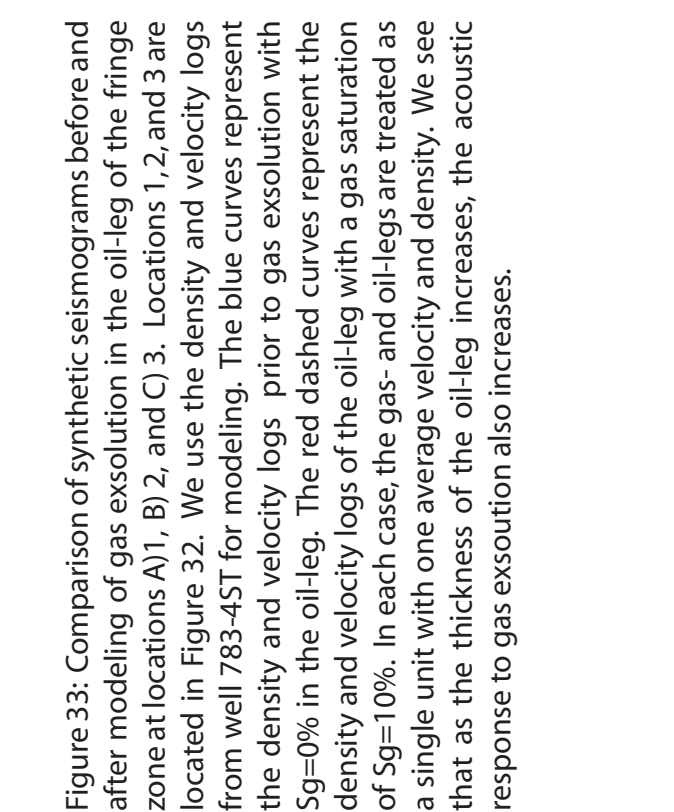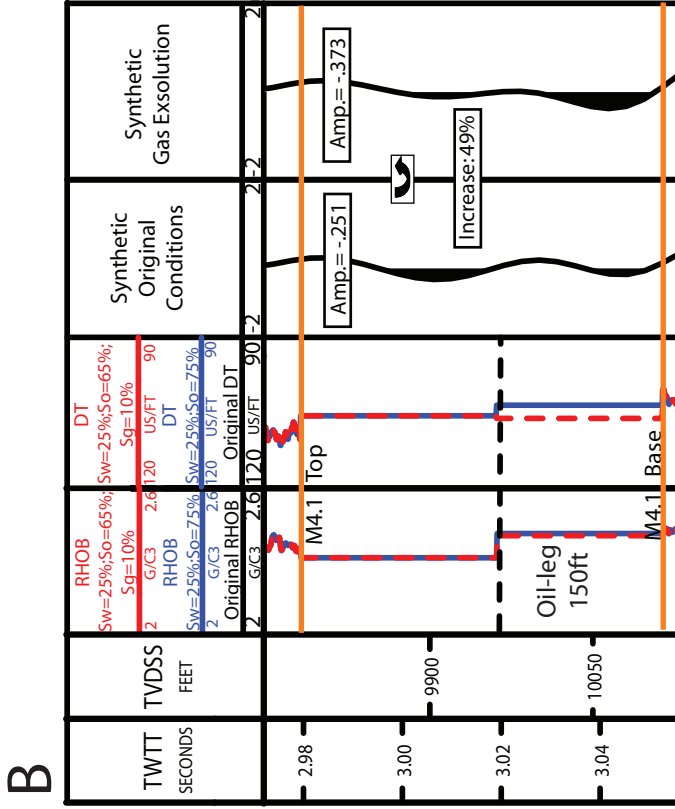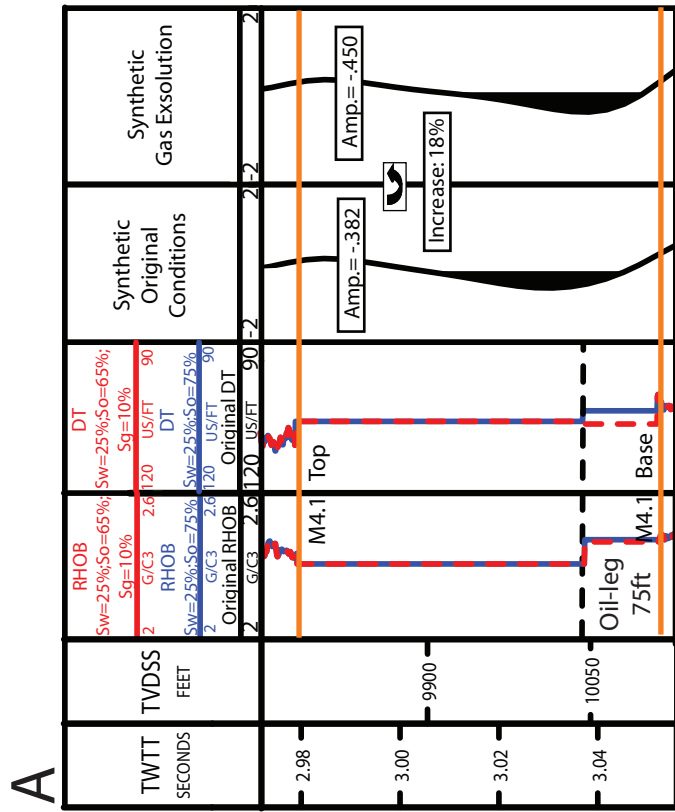
Figure 33: Comparison of synthetic seismograms before and after modeling of gas exsolution in the oil-leg of the fringe zone at locations A)1, B) 2, and C) 3. Locations 1,2,and 3 are located in Figure 32. We use the density and velocity logs from well 783-4ST for modeling. The blue curves represent the density and velocity logs prior to gas exsolution with Sg=0% in the oil-leg. The red dashed curves represent the density and velocity logs of the oil-leg with a gas saturation of Sg=10%. In each case, the gas- and oil-legs are treated as a single unit with one average velocity and density. We see that as the thickness of the oil-leg increases, the acoustic response to gas exsoution also increases.

76
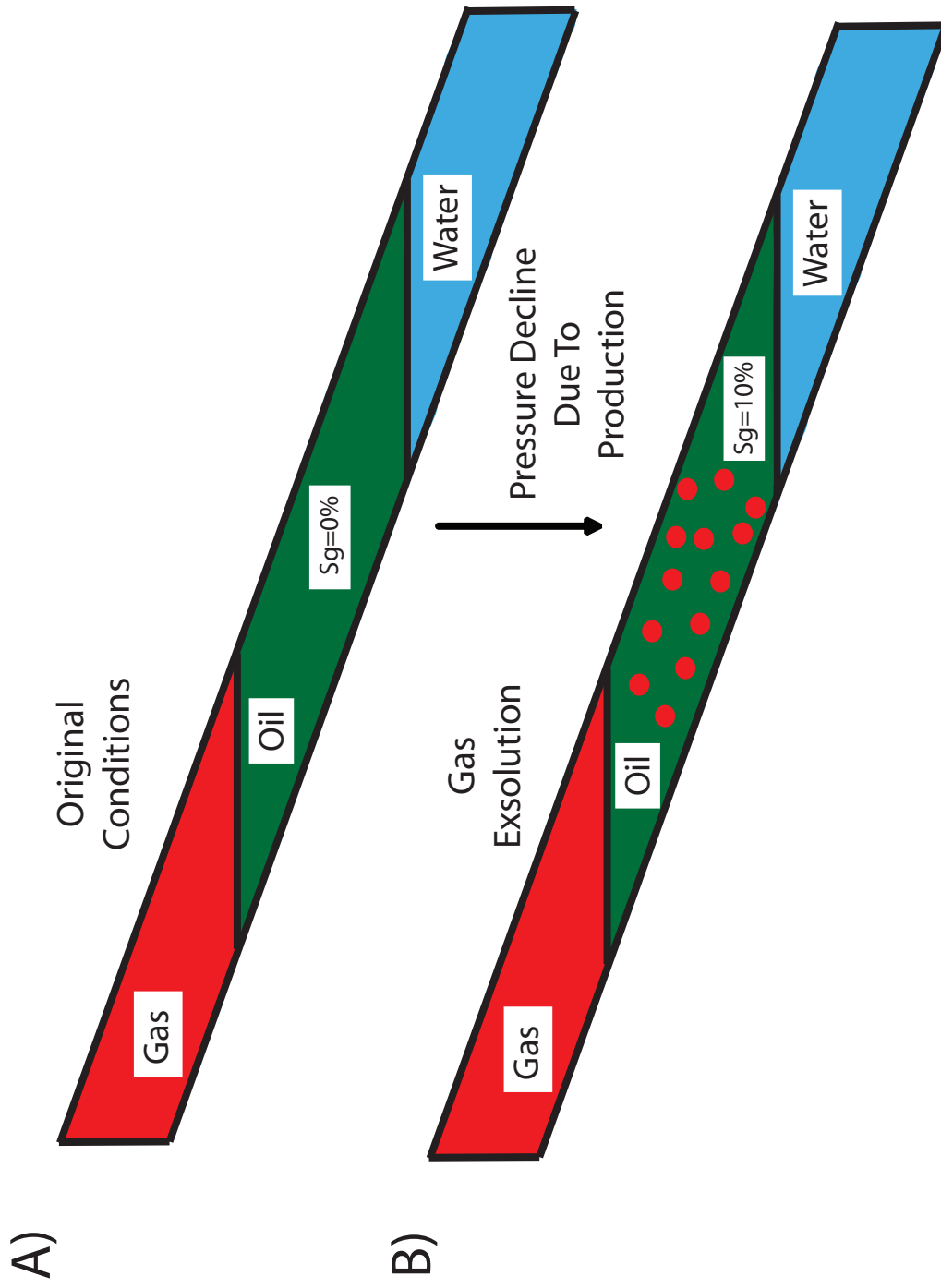
Figure 34: Model illustrating increasing gas saturation in the oil phase of the reservoir. As pressure in the reservoir declines below the bubble point, gas comes out of solution. A) Model of the reservoir fluid distribution prior to production. Gas saturation in the oil phase is equal to zero at this time. B) Model of reservoir fluid distribution after production has occurred. Gas saturation in the oil phase has increased due to gas exsolution. The presence of gas in the oil phase of the reservoir significantly decreases the acoustic impedance.
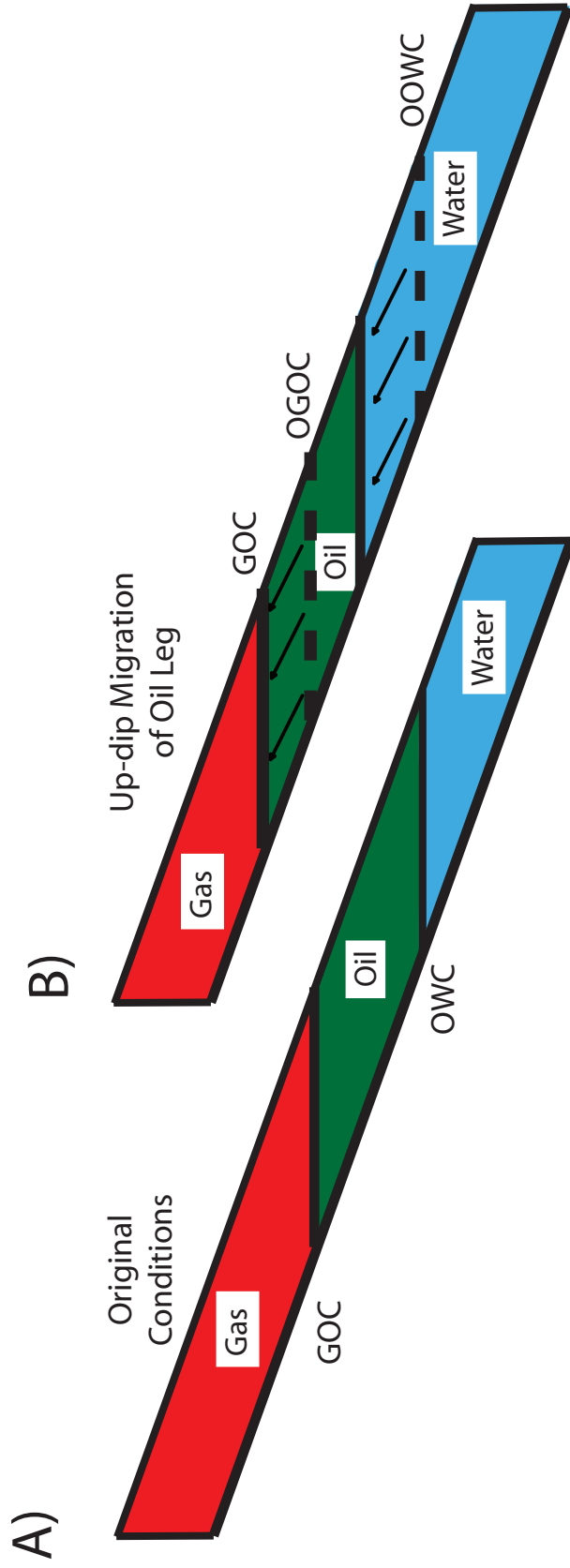
Figure 35: Model illustrating increasing oil saturation in a gas-oil system. As production occurs, the oil leg migrates up-dip and replaces gas with oil. A) Model of the reservoir fluid distribution prior to production with the gas-oil (GOC) and oil-water (OWC) contacts shown. B) Model of reservoir fluid distribution after production has occurred. The oil leg has migrated up-dip and the GOC and OWC are now located at shallower depths. The original gas-oil and oil-water contacts are labeled OGOC and OOWC, respectively.

Time-lapse analysis shows an increase in seismic amplitude in region R4, above the initial gas-oil contact (GOC), which we attribute to gas exsolution in the oil phase (Fig. 26). Within region R4, in an area we term the "fringe" zone, the M4.1 sand contains both gas and oil (Fig. 32). We show, through Gassmann fluid substitution and synthetic seismogram modeling, that gas exsolution in the oil phase of this zone is consistent with the observed seismic strengthening (Fig. 33).

We observe the strongest changes in seismic response in regions R1 and R4 (Fig. 26). Region R1 exhibits a strong amplitude response in the original seismic data (Fig. 5). Analysis of the M4.1 at this location shows the amplitude response is due to the large impedance contrast between the very clean sand and overlying shale (Fig. 12A). As a result, drainage in this region significantly impacts the acoustic properties of the reservoir and results in the strong seismic differences we observe (Fig. 26). Region R4, located in the West Levee, also shows a strong response in the seismic difference map (Fig. 26). The M4.1 in this region contains the thickest sand found in the reservoir (Fig. 7). In this region, tuning effects related to increased sand thickness drive the strong observed differences in seismic response (Fig. 26).

Through the use of time-lapse analysis, we attribute observed seismic differences after seven years of production to changes in the acoustic properties of the M4.1 reservoir. Our analysis of changes in the fluid behavior of the M4.1 has provided insight into how production affects the acoustic properties of the reservoir. This time-lapse analysis has also increased our understanding of the initial (pre-production) fluid conditions in the reservoir. For example, our analysis resulted in the identification of oil reserves in a region that was initially believed to contain only gas. Finally, based on the

time-lapse analysis, we relocated a pre-production oil-water contact, which resulted in the

identification of additional hydrocarbon reserves.

Nomenclature

Symbol	Description	Dimension
K_{dry}	rock dry frame modulus	GPa
K_{fl}	bulk fluid modulus	GPa
K_g	gas modulus	GPa
K_{oil}	oil modulus	GPa
K_s	solid grain modulus	GPa
K_w	water modulus	GPa
M	rock bulk p-wave modulus	GPa
RFC	reflection coefficient	none
S	constant	none
S_g	gas saturation	v/v
S_o	oil saturation	v/v
S_w	water saturation	v/v
S_{hyd}	hydrocarbon saturation	v/v
v	Poisson's ratio	v/v
V_g	velocity of gas saturated sand	ft/s
V_o	velocity of oil saturated sand	ft/s
V_p	p-wave velocity	ft/s
V_w	velocity of water saturated sand	ft/s
σ	effective stress	MPa
ρ_b	bulk density	g/cc
ρ_{b0}	initial bulk density	g/cc
ρ_f	fluid density	g/cc

Nomenclature cont.

Symbol	Description	Dimension
ρ_{f0}	initial fluid density	g/cc
ρ_m	grain matrix density	g/cc
ρ_w	density of water	g/cc
ρ_o	density of oil	g/cc
ρ_g	density of gas	g/cc
P	reservoir pressure	psi
T	reservoir temperatire	$^{\circ}$R
API	API gravity	degree
V_{oil}	ultrasonic velocity of oil	m/s
x	amplitude values from the 2001 data	v
y	amplitude values from the 1993 data	v
y_i	value of y at the ith location	v
μ	set of error values in the set of obsrvations of the 2001 data	v
σ_x	standard deviation x	v
σ_y	standard deviation of y	v
σ_μ	standard deviation of μ	v
$\bar{x}$	mean of all x values	v
$\bar{y}$	mean of all y values	v
$\hat{y}$	set of all amplitude values from 1993 after regression normalization	v
$\sigma_{x\hat{y}}$	covariance of x and $\hat{y}$	none
$\sigma_{\hat{y}}$	standard deviation of $\hat{y}$	v
r	correlation coefficient	none
σ_x^2	variance of x	v
σ_μ^2	variance of μ	v

References

Akkurt, R., Moore, A. M., Freeman, J.J., 1997. Impact of NMR in the development of a deepwater turbidite field. SPWLA 38th Annual Logging Symposium, June 15-18, p.1-12.

Batzle, K. and Wang, Z., 1992, Seismic properties of pore fluids: Geophysics, vol. 47, no. 11, pp. 1396 – 1408.

Benson, A. K., and Wu, J., 1999, A modeling solution for predicting a) dry rock modulus, rigidity modulus and b) seismic velocities and reflection coefficients in porous, fluid-filled rocks with applications to rock samples and well logs: Journal of Applied Geophysics, vol. 41, pp. 49 – 73.

Biot, M. A., 1955. Theory of elasticity and consolidation for a porous anisotropic solid. Journal of Applied Physics, 26, 182 – 185.

Biot, M. A., 1956. Theory of propagation of elastic waves in a fluid-saturated porous solid: 1. Lower frequency range, 2. Higher frequency range. Journal of Acoustical Society of America, 28, 168 – 191.

Blangy, J.P., 1992, Integrated seismic lithologic interpretation: the petrophysical basis, Stanford University PhD thesis, 414 pp.

Brown, A. R., 2004, Interpretation of three-dimensional seismic data: The American Association of Petroleum Geologists and the Society of Exploration Geophysicists.

Burkhart, T., 1997, Time lapse monitoring of the South Timbalier block 295 field, offshore, Louisiana: Masters thesis, The Pennsylvania State University.

Burkhart, T., Hoover, A.R., and Flemings, P. B., 2000, Time lapse (4D) seismic

    monitoring of primary production of turbidite reservoirs at South Timbalier

    block 295, offshore Louisiana, Gulf of Mexico: Geophysics, vol. 65, no. 2,

    pp. 351 - 367

Comisky, J., 2002, Petrophysical analysis and geologic model for the Bullwinkle J sands

    with implications for time-lapse reservoir monitoring, Green Canyon block 65,

    offshore Louisiana: Masters thesis, The Pennsylvania State University.

Domenico N., 1977, Elastic properties of unconsolidated porous sand reservoirs:

    Geophysics, vol. 42, no. 7, pp. 1339 - 1368

Enunwa, C., Razzano, J.L., Ramgulam, A., Flemings, P.B., Ertekin, T., and Karpyn, Z.T.,

    2005, Tahoe Field Case Study – Understanding reservoir compartmentalization in

    a channel-levee system: Gulf Coast Association of Geological Societies

    Transactions, vol. 55.

Fonnesu, F., 2003. 3D seismic images of a low-sinuosity slope channel and related

    depositional lobe (West Africa deep-offshore). Marine and Petroleum Geology,

    20, p. 615-629.

Gabriels, P. W., Horvei, N.A., and Koster, J. K., 1999, Time lapse seismic monitoring of

    the Draugen Field. SEG Expanded Abstract.

Gassmann, F., 1951, Elastic waves through a packing of spheres: Geophysics, vol. 16, pp.

    673 – 685.

Geertsma, J., 1961, Velocity-log interpretation: the effect of rock bulk compressibility.
Society of Petroleum Engineering Journal 1, 235 – 248.

Geertsma, J., Smit, D. C., 1961, Some aspects of elastic wave propagation in
fluid-saturated porous solids. Geophysics, vol. 26, pp. 169-181.
Gregory, A. R., 1976, Fluid saturation effects on dynamic elastic properties of
sedimentary rocks: Geophysics, vol. 41, pp. 895 -921.

Han, D., Nur, A., and Morgan, D., 1986, Effects of porosity and clay content on wave
velocities in sandstones: Geophysics, vol. 51, pp. 2093 – 2107.

Henry, S., 2000, Pitfalls in synthetics. The Leading Edge, pp. 604 - 606

Kendrick, J.W., 2000. Turbidite reservoir architecture in the Northern Gulf of Mexico
deepwater: insights from the development of Auger, Tahoe, and Ram/Powell
fields. GCSSEPM Foundation 20th Annual Research Conference, Deep-water
Reservoirs of the World, p.450-468.

Landro, M., 2001, Discrimination between pressure and fluid saturation changes from
time lapse seismic data: Geophysics, vol. 66, no. 3, pp 836 - 844

Lumley, D. E., Nunns, A. G., Delorme, G., Adeogba, A. A., and Bee, M. RF., 1999,
Meren Field, Nigeria: A 4D seismic case study: SEG Expanded Abstract.

Lumley, D. E., 2001, Time-lapse seismic reservoir monitoring: Geophysics, vol. 66, no. 1
pp. 50 - 53

Mavko, G., and Mukerji, T., 1995, Seismic pore space compressibility and Gassmann's
relation: Geophysics, vol. 60, pp. 1743 – 1749.

Najjar, N. F., Strønen, L. K., and Alsos, T., 2003. Time-lapse seismic programme at

      Gullfaks: value and the road ahead. Petroleum Geoscience, vol. 9, p. 35 - 41

Peterson, R.A., Fillippone, W.R., and Coker, F.B., 1955, The synthesis of seismograms

      from well data: Geophysics, vol. 20, no. 3, pp.516 – 538.

Robinson, N., Ford, A., Howie, J., Manley, D., Riviere, M., Stewart, S., Thomas, R.,

      2005. 4D time-lapse monitoring of Chirag Field. The Leading Edge, pp. 928 - 932

Rollins, D. R., Shew, R.D., 1993. Geophysical and petrophysical properties of thinly

      bedded turbidite deposits, eastern Gulf of Mexico. Society of Petroleum

      Engineers 68th Annual Technical Conference and Exhibition, Houston, SPE

      Paper No. 26505.

Shew, R.D., Tiller, G.M., Hackbarth, C.J., Rollins, D.R., and White, C.D., 1995.

      Characterization and modeling of channel and thin-bedded turbidite prospects in

      the Gulf of Mexico: integration of outcrops, modern analogs, and subsurface data.

      Society of Petroleum Engineers 70th Annual Technical Conference and

      Exhibition, Dallas, SPE Paper No. 30535.

Smith, T. M., Sondergeld, C. H., and Rai, C. S., 2003, Gassmann fluid substitution: A

      tutorial: Geophysics, vol. 68, no. 2, pp. 430 – 440.

Spencer, J.W., Cates, M.E. and Thompson, D.D., 1994, Frame moduli of unconsolidated

      sands and sandstones, Geophysics, vol. 59, no. 9, pp. 1352 – 1361.

Tiab, D., and Donaldson, E. C., 1996, Petrophysics: Theory and Practice of Measuring

      Reservoir Rock and Fluid Transport Properties: Gulf Publishing Company

Waggoner, J. R., Cominelli, A., Seymour, R. H., and Stradiotti, A., 2003. Improved reservoir modeling with time-lapse seismic data in a Gulf of Mexico gas condensate reservoir. Petroleum Geoscience, vol. 9, pp. 61 - 72

Wang, Z., 2001, Fundamentals of seismic rock physics: Geophysics, vol. 66, no. 2, pp. 398 – 412.

Weisenborn, T., and Hague, P., 2005. Time-lapse seismic in Gannet A: One more lead firmly integrated. The Leading Edge, pp. 80 - 85

White, C.D., Bradburn, F.R., Brown, R.L., and Thieme, M.A., 1992. Reservoir potential of thin-bedded turbidites: prospect Tahoe. Society of Petroleum Engineers 67th Annual Technical Conference and Exhibition, Washington, SPE Paper No. 24875.

Widess, M.B., 1973, How thin is a thin bed: Geophysics, vol. 38, no. 6, pp. 1176 - 1180

Wood, A. B., 1941, A textbook of sound: G. Bell and Sons.

Wyllie, M. R. J., Gregory, A. R., and Gardner, L. W., 1956, Elastic wave velocities in heterogeneous and porous media: Geophysics, vol. 21, no. 1, pp. 41 – 70.

Yilmaz, OZ., 2001, Seismic Data Analysis: Society of Exploration Geophysicists, vol. 1, pp. 170 – 171.

Zhang, J. J., and Bentley, L. R., 2000, Change of elastic moduli of dry sandstone with effective pressure. SEG Expanded Abstract.

Appendix A

Discussion of Synthetic Seismogram Technique

Synthetic seismograms provide a link between well information and seismic reflectors. This link is established by translating logged rock properties into a synthetic seismic trace. We generate synthetic seismograms by convolving a source wavelet with an integrated reflection coefficient (IRFC) series. This is a three step process: create the IRFC series using impedance log data, generate a source wavelet, and convolution of the source wavelet with the IRFC series.

The first step in creating the IRFC series is to generate an impedance log by multiplying the density log (ρ) by the velocity log (v) at the well location:

$$impedance = \rho v \, . \qquad\qquad \text{A1}$$

Impedance is calculated at all depths where there are velocity and density log measurements. The impedance log is then used to calculate a reflection coefficient (RFC) series using Equation A2:

$$RFC = \frac{\rho_2 v_2 - \rho_1 v_1}{\rho_2 v_2 + \rho_1 v_1} \qquad\qquad \text{A2}$$

Next, we integrate the RFC series to obtain an IRFC series:

$$IRFC = \sum_{1}^{n} RFC \, . \qquad\qquad \text{A3}$$

The second step in creating a synthetic seismogram is to generate a source wavelet that will be convolved with the IRFC series. In order to apply a source wavelet that is a close match to that present in the original seismic, autocorrelation and frequency domain analyses were performed on the seismic data to identify the proper wavelet. The

key characteristics of the wavelet we were interested in obtaining were the peak frequency and shape. Since reflectivity is assumed a random process, this implies that the seismogram has the characteristics of the seismic wavelet. Therefore, by performing an autocorrelation of the seismic data, which we possess, we can substitute this for an autocorrelation of the seismic wavelet, which is unknown (Yilmaz, 2001). We chose to use a Ricker wavelet in the generation of synthetic seismograms based on the shape observed in the autocorrelation of several traces (Fig. A1). After analyzing the frequency content of the autocorrelated traces, a peak frequency of 25Hz was chosen for the Ricker wavelet.

The last step is to convolve the IRFC with the source wavelet.

Gassmann Model Application

Gassmann modeling provides us with predicted values of velocity and bulk density with changes in fluid saturation and reservoir pressure. We use the synthetic techniques described above to model the impact these changes will have on RFC and synthetic amplitude. The M4.1 sand is highly laminated and contains numerous alternating sand and shale layers. To simplify modeling changes in velocity and density, we treat the M4.1 as a single unit of thickness with one designated velocity and bulk density for each synthetic seismogram. The new values of velocity and bulk density are substituted into the original velocity and bulk density logs. The synthetic is then generated using the modified logs. An example of the velocity and bulk density log substitution used to generate synthetic seismograms is found in Figure A2.
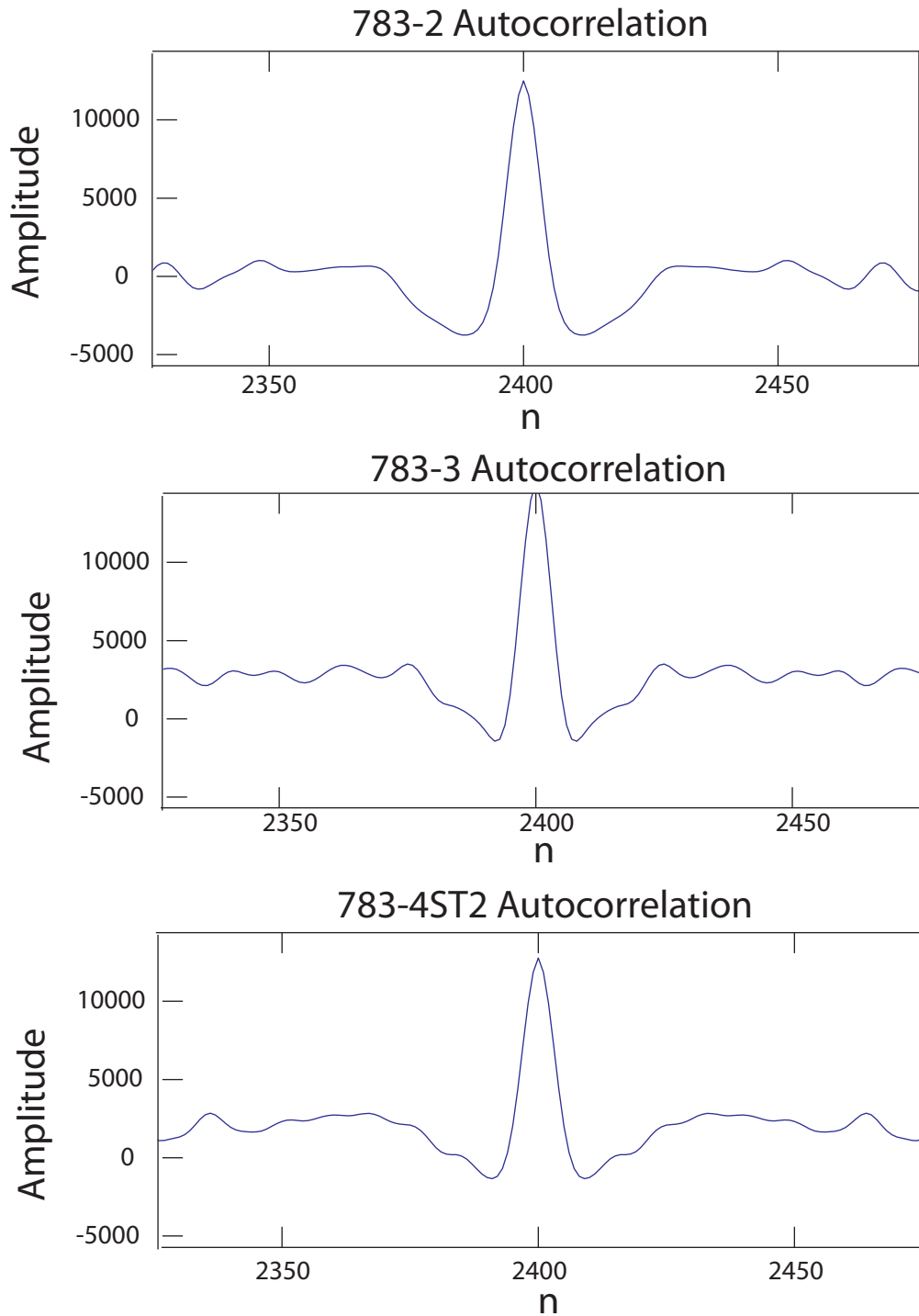
Figure A1: Autocorrelation traces of extracted seismic from wells 783-2, 783-3, and 783-4ST2. All three autocorrelations show a Ricker shape to the wavelet. Frequency domain analysis of these traces shows an average peak frequency of 25Hz. Therefore, a 25Hz Ricker wavelet is used as the source wavelet for synthetic seismogram generation. Wells are located in Figure 2.
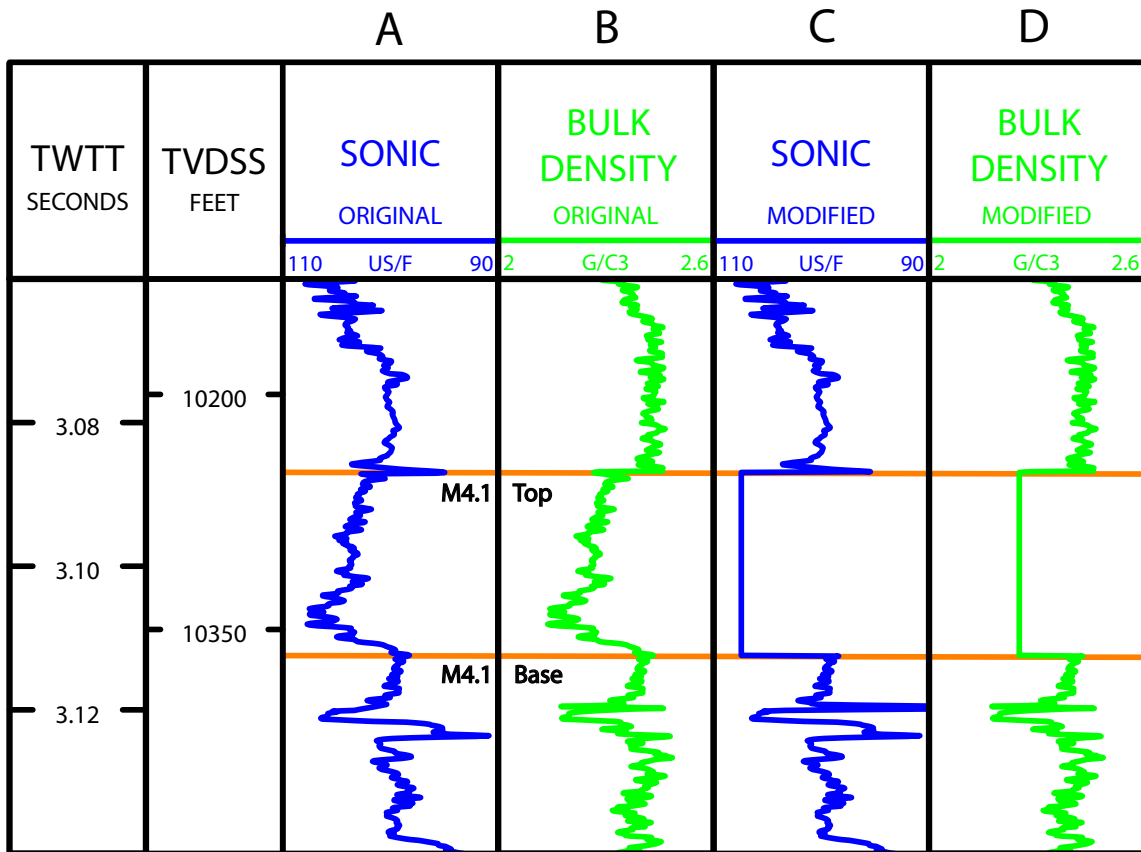
Figure A2: Original A) sonic and B) density logs for well 783-3. Modified C) sonic and D) density logs used in synthetic modeling. The decrease in sonic and density seen in the modified logs is based on Gassmann modeling of gas exsolution up to Sg=10%. The modified logs illustrate the treatment of the M4.1 sand as a single unit of thickness for synthetic modeling. Well 783-3 is located in Figure 2.

Appendix B

B-1: CALCULATION OF OIL MODULUS (K_{oil})

We calculate the ultrasonic velocity of the oil (V_{oil}) based on the following correlation (Batzle et al., 1992):

$$V_{oil} = 15450(77.1 + API)^{-\frac{1}{2}} - 3.7T + 4.64P + 0.0115\left(0.36API^{\frac{1}{2}} - 1\right)TP. \qquad \text{B1}$$

API is API gravity, T is the reservoir temperature, and P is reservoir pressure. API gravity based on fluid analysis is 54°, T is 660° R, and P is 5,000psi. V_{oil} is calculated at 1,114 m/s. Using this velocity and an oil fluid density of 0.7628 g/cc, derived from fluid sample analysis, the oil modulus is calculated to be 947 MPa using Equation B2 (Smith, 2003):

$$K_{oil} = \rho_f\left[V_p^{\;2}\right] \qquad \text{B2}$$

B-2: CALCULATION OF K_{DRY}

Using a method described by Benson et al. (1999), we calculate K_{dry} at several well locations throughout the M4.1. This method involves using the BGG equation (Biot-Geertsma-Gassmann), which represents the velocity of sound in a fluid-saturated, porous rock.

$$V_p = \{[K_{eff} + 4/3\mu]/\rho_b\}^{1/2},$$ B3

Benson inverted Equation B3 to solve for K_{dry} using Equations B4 though B7 found below. See Benson (1999) for derivation of these equations.

$$r = \frac{3(1-v)}{(1+v)}$$ B4

$$X = \frac{r\left(1 - \phi + \phi\left(\frac{K_s}{K_{fl}}\right)\right) + \frac{\rho_b V_p^2}{K_s} - 2}{2(r-1)}$$ B5

$$Y = \frac{\left(1 - \phi + \phi\left(\frac{K_s}{K_{fl}}\right)\right)\left(\frac{\rho_b V_p^2}{K_s} - 2\right) - 1}{(r-1)X^2}$$ B6

$$K_{dry} = X\left[1 - (1-Y)^{\frac{1}{2}}\right]K_s$$ B7

These equations relate the dry bulk modulus (K_{dry}) to the following: p-wave velocity (V_p), porosity (ϕ), Poisson's ratio (v), solid grain modulus (K_s), bulk fluid modulus, (K_{fl}), and bulk density (ρ_b).

Average values for velocity, bulk density, and porosity are obtained from well log data at each well location. Poisson's ratio and solid grain modulus are assumed constant and

have values of 0.18 and 38MPa respectively (Table 3). K_{fl} is the modulus of the composite reservoir fluid and can be obtained using woods equation (Wood, 1941):

$$\frac{1}{K_{fl}} = \frac{S_w}{K_w} + \frac{S_o}{K_o} + \frac{S_g}{K_g} , \qquad \text{B8}$$

S_w, S_o, and S_g are water, oil, and gas saturations, respectively, and were obtained from log information. The values for the individual fluid moduli in Equation B8 are constants and can be found in Table 3.

EXAMPLE K_{dry} Calculation at Well 783-3

Average velocity (V) and bulk density (ρ_b) of the M4.1 sand at well 783-3 were calculated using available log data (Fig. B1). Porosity (Φ) was obtained from well log information (Table B1). Poisson's ratio (ν) and the solid grain bulk modulus (K_s) are constants at 0.18 and 38GPa respectively (Table B1). The M4.1 in this location has a water saturation of 25%, an oil saturation of 75%. Rearranging Equation B8 we solve for the composite fluid modulus (K_{fl}).

$$K_{fl} = \frac{1}{\left[\dfrac{S_w}{K_w} + \dfrac{S_o}{K_o}\right]} . \qquad \text{B9}$$

K_{fl}= 1.14 GPa

The following table is a list of the necessary parameters and their values for the calculation of K_{dry} in the location of well 783-3:

Table B1

v	0.18
K_{fl}	1.14 GPa
ρ_b	2.27 g/cc
K_s	38 GPa
Φ	28%
V	2.9 km/s

Using the parameters found in Table B1 and Equations B4 – B7, we solve for K_{dry} at well 783-3:

$$K_{dry} = 8.29 GPa.$$

This value represents the rock's dry bulk modulus or stiffness. This is the incompressibility of the rock frame devoid of any fluids. The parameter values and corresponding K_{dry} calculation at each well location can be found below in Table B2:

Table B2

Well	Location	V_p (ft/s)	Φ (%)	K_{fl} (GPa)	ρ_b (g/cc)	K_{dry} (GPa)
783-1	Channel	9,333	27	0.08	2.21	8.49
783-1ST1	E. Levee	9,611	28	0.07	2.37	9.66
783-2	Channel	10,224	28	2.84	2.23	7.67
783-2ST1	E. Levee	10,101	29	1.26	2.34	9.78
783-3	E. Levee	9,657	28	1.25	2.27	8.3
783-4	W. Levee	9,590	28	0.07	2.34	9.53
783-4ST1	W. Levee	9,495	28	0.07	2.21	8.79
783-4ST2	W. Levee	9,644	28	0.07	2.35	9.66
783-5BP	E. Levee	10,487	25	0.08	2.31	11.24

All calculated K_{dry} values fall between 7.67 and 9.78GPa with one exception, the 783-5BP well (Table B2). The M4.1 at this location has a much higher velocity when compared to the M4.1 at all other well locations which causes the larger value of K_{dry}. We use the calculated K_{dry} values to define an average dry frame modulus for both an oil- and gas-saturated M4.1 (Table 4). The average rock and fluid properties for an oil- and gas-saturated M4.1 are summarized in Table 4. These properties serve as the initial parameters to calibrate the fluid substitution model.
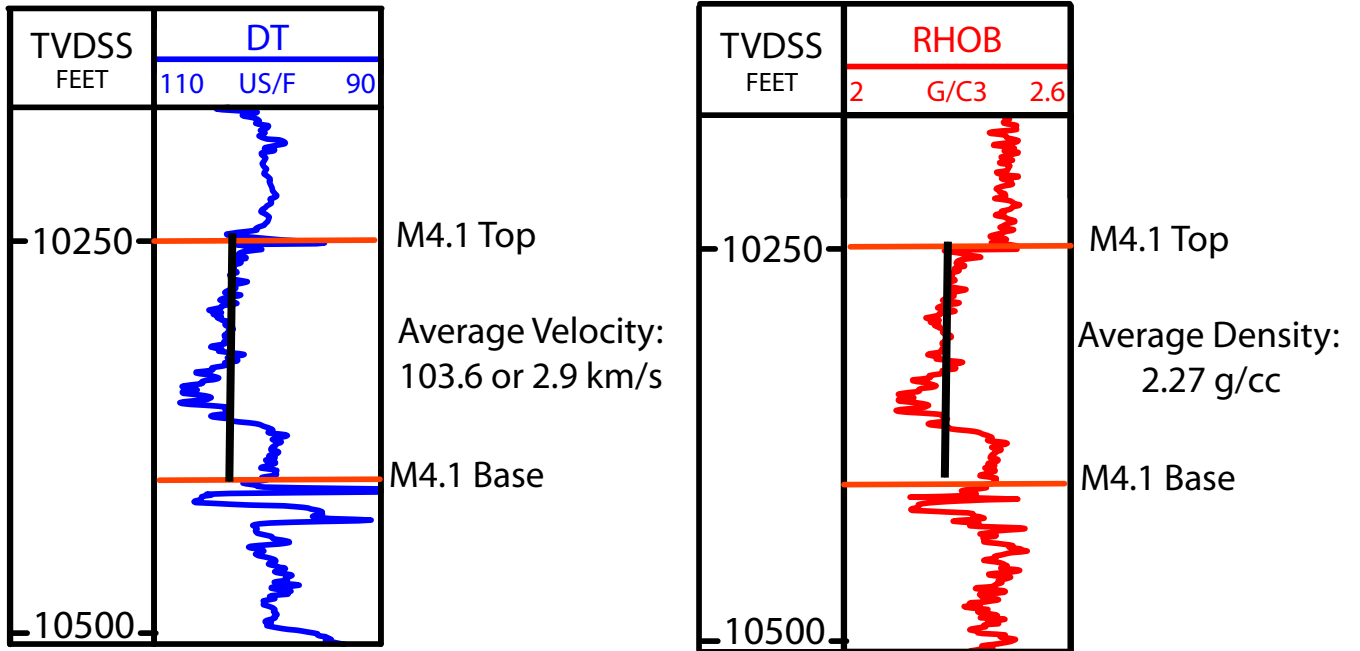
Figure B1: Sonic and density logs for well 783-3. The average interval velocity (2.9km/s) and bulk density (2.27g/cc) of the M4.1 sand is marked by the solid black line passing through each log. Well 783-3 is located in Figure 2.

Appendix C

Tahoe Field Case Study- Understanding Reservoir Compartmentalization in a Channel-Levee System

Refer to pocket insert